DETERMINING GAS TEMPERATURE FROM SPECTROSCOPIC MEASUREMENTS IN ELECTRIC OXYGEN-IODINE LASERS

BY

MICHAEL THOMAS DAY

THESIS

Submitted in partial fulfillment of the requirements
for the degree of Master of Science in Aerospace Engineering
in the Graduate College of the
University of Illinois at Urbana-Champaign, 2011

Urbana, Illinois

Adviser:

Professor Wayne C. Solomon

Abstract

Gas temperature is a driving factor in the performance of electric oxygen-iodine lasers. Due to the importance of temperature, the gas temperature must be measured at different locations throughout the laser system. Problems with traditional measurement techniques have led to molecular spectroscopy being relied upon for gas temperature measurements. In the past, all temperature information was calculated using the $O_2(b^1\Sigma)$ emission spectrum. This thesis discusses a new temperature diagnostic so that gas temperatures can be obtained from the $O_2(a^1\Delta)$ emission spectrum. Determining the temperature from $O_2(a^1\Delta)$ is accomplished by matching the experimental spectrum to a temperature-dependent theoretical spectrum. The theoretical spectrum is formed using the high-resolution transmission molecular database. Additionally, the high-resolution transmission molecular database was used to create a new temperature diagnostic for the $O_2(b^1\Sigma)$ spectrum. The new $O_2(a^1\Delta)$ and $O_2(b^1\Sigma)$ temperature diagnostics are compared to the current temperature diagnostics. Potential problems with both the old and new temperature diagnostics are discussed. Remedies to these problems also will be presented.

Acknowledgments

This work was supported by the Defense Advanced Research Projects Agency (DARPA) prime contract #HR0011-09-C-0025 on a subcontract from Physical Sciences, Inc. Additional support came from CU Aerospace internal research and development funds and the Directed Energy Professional Society (DEPS) Scholarship Program.

I would like to thank my advisor, Professor Wayne C. Solomon, for giving me the opportunity to work with the EOIL research group and for providing motivation and guidance as I have completed this work. Also, I would like to thank Dr. David L. Carroll and Professor Joseph T. Verdeyen for the helpful advice they have provided since I began working in the EOIL research group. Additionally, I thank W. T. Rawlins of Physical Sciences, Inc. for providing technical guidance. Also, I would like to thank the other members of the EOIL research group (past and present) for the contributions they have made to this research: Dr. Joseph W. Zimmerman, Brian S. Woodard, Gabriel F. Benavides, Darren M. King, Scott Tuttle, Tyler Field, and Brian Shea.

Additionally, I would like to thank my family for their love and support. Their encouragement and interest in my research motivated me to work hard each and every day. Finally, I thank Stephanie for the love and support she has provided as I have worked on this research.

Table of Contents

Nomenclature

Abbreviations:

AFRL	Air Force Research Laboratory
ALTB	Airborne Laser Test Bed
Cav	cavity
CCD	charge-coupled device
COIL	chemical oxygen-iodine laser
CUA	CU Aerospace (Champaign, IL)
EOIL	electric oxygen-iodine laser
eV	electron volt
FWHM	full width at half maximum
GPM	gallons per minute
HITRAN	high-resolution transmission molecular database
HEX-1	heat exchanger design 1
HEX-2	heat exchanger design 2
ID	inner diameter
ISD	Iodine Scan Diagnostic
LN_2	liquid nitrogen
OD	outer diameter
OMA	optical multi-channel analyzer
PMT	photomultiplier tube
PSI	Physical Sciences Inc. (Andover, MA)
RF	radio frequency
SOG	singlet oxygen generator
TH	threshold
UIUC	University of Illinois at Urbana-Champaign
VertiCOIL	vertical chemical oxygen-iodine laser

Variables:

A_{21}	Einstein coefficient for spontaneous emission
B	rotational constant for oxygen
B_{12}	Einstein coefficient for induced absorption
c	speed of light
c_2	second radiation constant
C_R	spectral resolution constant
E_X	energy of state X
g	lineshape function
g_X	statistical weight of state X
h	Planck's constant
I	intensity
I_X	intensity of emission with rotational quantum number J_X
J_X	rotational quantum number

k	Boltzmann constant
k_f	forward reaction rate of $O_2(a) – I^*$
k_r	reverse reaction rate of $O_2(a) – I^*$
K_{eq}	temperature-dependent equilibrium constant of $O_2(a) – I^*$
kT	temperature (in wavenumber)
m	molecular mass
n_X	number density of state X
N	total molecular number density
P	peak
Q	total internal partition function
S_{12}	absorption line intensity
S_{21}	emission line intensity
T	temperature
T_{REF}	reference temperature
V	valley
Y_{TH}	threshold yield of $O_2(a)$
$\Delta\lambda$	wavelength resolution
$\Delta\nu_D$	Doppler linewidth
λ	wavelength
λ_0	location of line center
ν_0	center frequency of emission
ν_{12}	spectral line transition frequency

Additional Subscripts and Superscripts:

1	lower state
12	lower to upper state (absorption)
2	upper state
21	upper to lower state (emission)
D	Doppler
E	experimental
eq	equilibrium
f	forward
inp	input
r	reverse
REF	reference
T	theoretical
TH	threshold
η	lower state
*	excited state

1. Introduction and Background

This section begins by providing essential background information on laser systems. In the first subsection, basic principles of laser operation are explained. Specific laser terminology will also be introduced and defined. Most of the terms introduced in this section will be used throughout this thesis. After the general overview on laser basics, the electric oxygen-iodine laser will be introduced. The remainder of this section will look at the history and development of electric oxygen-iodine laser systems. Also, current research efforts of this laser technology will be discussed.

1.1 Laser Basics

Laser is an acronym for **l**ight **a**mplification by **s**timulated **e**mission of **r**adiation. In most general terms, lasers can be subdivided into three groups: gas, solid-state, and liquid. A more precise laser nomenclature describes the specific lasing media and/or the way in which lasing species are pumped to the upper lasing state. This classification methodology gives rise to categories such as fiber, diode, rare-gas, ion, free electron, excimer, chemical, dye, metal vapor, and semiconductor lasers.

No matter into which category a specific laser fits, the basic principles of operation are the same: all lasers involve the electronic transfer of atoms or molecules from excited energy states. As known from quantum theory, energy comes in discrete packages associated with two energy levels. When an atom transitions from a higher to lower energy level, radiation is emitted in the form of a photon. Einstein identified three elementary quantum mechanisms of radiation for a simple, two-level model of an atom: absorption, spontaneous emission, and stimulated emission. In absorption, an atom in a lower energy level (denoted as state 1) absorbs a photon and transfers to a higher energy level (denoted as state 2). In spontaneous emission, an atom in state 2 decays to state 1 and emits a photon in a random spatial direction.

As the name implies, lasers operate on the process of stimulated emission. In stimulated emission, an atom in state 2 emits a photon when encountered by another photon with the same energy. This results in the production of two photons at the same frequency, polarization, phase, and direction of propagation of the stimulating photon [1.1]. These properties make laser radiation different from incoherent sources of light such as light bulbs. The processes of absorption, spontaneous emission, and stimulated emission are shown in Figure 1.1.

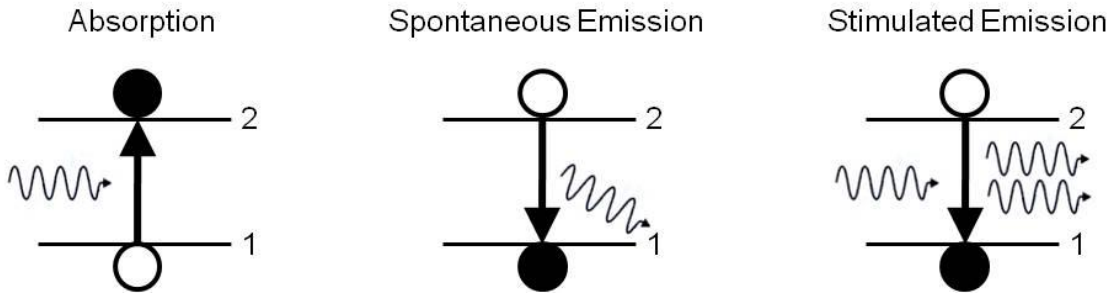

Figure 1.1 Three elementary quantum mechanisms of radiation for a simple, two-level model of an atom: absorption, spontaneous emission, and stimulated emission. Lasers operate on stimulated emission, which produces photons having the same frequency, polarization, phase, and direction of propagation [Adapted from 1.2].

The basic laser consists of two mirrors which form an optical resonator. Between these two mirrors is a medium (known as the gain region) which contains the excited lasing species. The gain region serves as an optical amplifier, which reinforces the strength of radiation. The term *gain* is used to quantify the amplification of optical amplifiers. For small gains, the gain is specified as a percentage per unit length. For example, a gain value of 5% cm^{-1} refers to an amplification factor of 1.05 per centimeter. The gain is dependent on the population densities of the upper and lower lasing state, with positive gain occurring when the population density of the upper lasing state is higher than the lower state. In order for positive gain to occur (also known as population inversion) the lower state must be excited to the upper lasing level. Therefore, all lasers require some sort of pumping mechanism to input energy and populate the upper lasing state.

When the pumping mechanism is first activated, species in the gain region begin to absorb energy and spontaneously emit. Since the spontaneous emission is occurring between the two mirrors, some of the emitted photons are reflected back into the gain region. These reflected photons then strike other excited species and cause stimulated emission to occur. When positive gain occurs, there are more atoms emitting photons due to stimulated emission than atoms absorbing photons, and the photons oscillate between the mirrors. Typically, one mirror is denoted as the *high reflector* and the other is the *low reflector*. The ideal *high reflector* would reflect every photon back into the gain region, resulting in increased stimulated emission. The *low reflector* also reflects photons back into the gain region; however, it allows some photons to be transmitted out of the resonator, resulting in a coherent laser beam emerging from one side. A simple model of a laser resonator is shown in Figure 1.2.

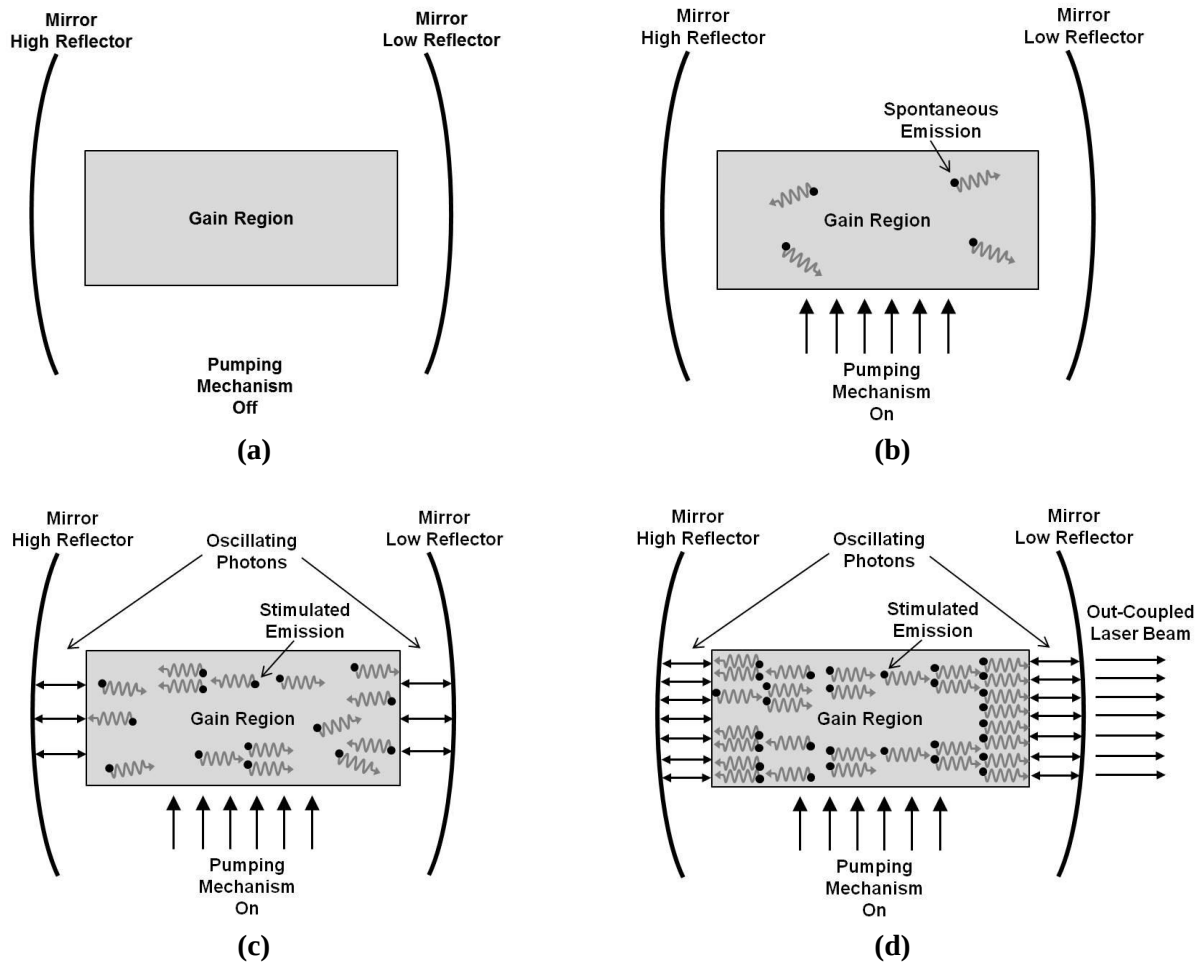

Figure 1.2. Simple model of laser resonator. (a) When the pumping mechanism is off, the upper laser state is not populated. (b) After the pumping mechanism is turned on, the lasing species is excited to the upper lasing state and spontaneously emits photons. (c) Photons begin to oscillate between the mirrors, reflect back into the gain region, and cause stimulated emission to occur. (d) Photons continue to oscillate between the mirrors, stimulated emission continues in the gain region, and the out-coupled laser beam emerges from the low-reflectivity mirror.

1.2 Chemical Oxygen-Iodine Lasers

A chemical laser is a type of laser in which the lasing species is pumped to the upper lasing level by a chemical process. One type of chemical laser is the **c**hemical **o**xygen-**i**odine **l**aser (COIL), which emits radiation at 1.315 μm from the magnetic dipole transition of atomic iodine from the excited electronic state $I(^2P_{1/2})$ (also denoted as I*) to the ground state $I(^2P_{3/2})$ (also denoted as I). The lasing reaction is shown as Equation (1.1)

$$I(^2P_{1/2}) \longrightarrow I(^2P_{3/2}) + h\nu \qquad (1.1)$$

where *hv* represents a photon at 1.315 μm. The first observations of lasing on the $I(^2P_{1/2})$ state were made by Kasper and Pimentel [1.3] where they used a pulsed flashlamp to photodissociate alkyl-iodide molecules. Later, Derwent *et al.* [1.4] determined that singlet molecular oxygen could be used in energy transfer pumping for the iodine atom. The first functional COIL was developed by the United States Air Force in 1978 by McDermott *et al.* [1.5]. In a COIL, the population inversion is created from the near resonant energy transfer between the excited singlet oxygen molecule $O_2(a^1\Delta)$ [also denoted as $O_2(a)$] and the ground state iodine atom. The pumping reaction is given as Equation (1.2)

$$O_2(a^1\Delta) + I(^2P_{3/2}) \underset{k_r}{\overset{k_f}{\rightleftharpoons}} O_2(X^3\Sigma) + I(^2P_{1/2}) \qquad (1.2)$$

where $O_2(X^3\Sigma)$ is the ground state oxygen molecule (also denoted as O_2) and k_f and k_r are the forward and reverse reaction rates, respectively. In traditional COIL devices, the production of $O_2(a)$ is done by a singlet oxygen generator (SOG). In the SOG, a chemical reaction between gaseous chlorine and aqueous basic hydrogen peroxide produces $O_2(a)$ very effectively. A detailed description of the production of $O_2(a)$ via chlorine gas and basic hydrogen peroxide can be found in Truesdell *et al*. [1.6].

In COIL, the $O_2(a)$ production serves two purposes. First, the energy stored in $O_2(a)$ is used to split the injected iodine molecules into atoms. It is known from empirical studies that an average of four to six $O_2(a)$ molecules is needed to dissociate one I_2 molecule [1.7]. Then, $O_2(a)$ excites the dissociated iodine atoms to the lasing state using near resonant energy transfer. Figure 1.3 shows the working energy levels and transitions in COIL. The arrow in Figure 1.3 shows how the energy in $O_2(a)$ transfers to $I(^2P_{3/2})$, which is then excited to $I(^2P_{1/2})$.

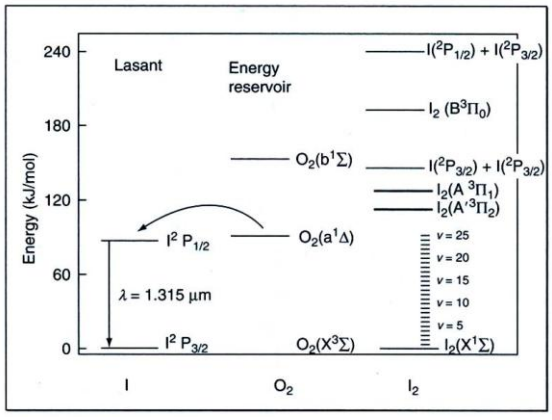

Figure 1.3. Energy levels and transitions in COIL. The $O_2(a)$ is used to split the ground state iodine molecule $I_2(X^1\Sigma)$ into two iodine atoms $I(^2P_{3/2})$ + $I(^2P_{3/2})$. Then $O_2(a)$ excites $I(^2P_{3/2})$ into $I(^2P_{1/2})$. The $I(^2P_{1/2})$ then releases radiation at 1315 nm [1.2].

Since its initial demonstration, COIL technology has undergone numerous improvements leading to greater laser power [1.6]. The recent development and testing of the Airborne Laser Test Bed (ALTB) is a testament to the high power levels that can be achieved from a COIL. The megawatt-class COIL system on the ALTB was designed to destroy ballistic missiles in the boost phase of flight [1.8]. The successful demonstration of ALTB destroying a missile [1.9] provides hope that this system can be implemented in missile defense.

Even though it has experienced great success in the past, the COIL system does have some drawbacks. While the liquid SOG method is highly efficient at producing $O_2(a)$, it requires heavy support equipment. The liquid chemicals used to produce $O_2(a)$ require large, heavy storage tanks, hindering the mobility of a tactical laser system. Also, the basic hydrogen peroxide and chlorine gas used by the SOG are toxic and dangerous. The logistics of dealing with the liquid SOG system motivated the investigation of all gas phase system. The Air Force Research Laboratory (AFRL) was the first to demonstrate that significant quantities of excited iodine atoms could be produced using an all gas-phase generator [1.10]. AFRL first used $NCl(a^1\Delta)$ to produce excited iodine atoms. This opened the door for other research focusing on the production of an all gas phase oxygen-iodine laser system

1.3 Electric Oxygen-Iodine Lasers

The variation to the COIL being studied at the University of Illinois in Champaign–Urbana (UIUC) and CU Aerospace (CUA) is the **e**lectric **o**xygen-**i**odine **l**aser (EOIL). The EOIL concept, proposed by Carroll and Solomon in 2000 [1.11], uses an all gas-phase system and produces the $O_2(a)$ from an electric discharge. Carroll *et al.* (the research group at UIUC-CUA) were the first to report measurements of positive gain on the electronic transition of the iodine atom at 1.315 μm pumped by resonance excitation transfer from $O_2(a)$ produced in an electric discharge [1.12]. Earlier studies on using electric discharges for $O_2(a)$ production to pump an iodine laser were made by Zalesskii [1.13] and Fournier *et al.* [1.14]; however, neither was able to achieve positive gain. Carroll *et al.* also had the first demonstration of laser power with an EOIL system [1.15].

Other research groups quickly followed in the work of the UIUC-CUA research group. Rawlins *et al.* from Physical Sciences Inc. (PSI) reported positive gain in a subsonic microwave-discharge flow reactor near room temperature [1.16]. Also, Hicks *et al.* from the Ohio State

University measured positive gain and laser power using a non-self-sustained pulser-sustainer discharge [1.17].

1.4 Basic Components of EOIL System

Since many research groups have been working on EOIL technology, different laser designs have evolved. However, a few basic components for EOIL operation are common. These components include: the electric discharge, iodine injectors, and a laser cavity. In all EOIL systems, a mixture of gas (usually oxygen O_2, helium He, and trace nitric oxide NO) flows through an electric discharge. The discharge ionizes the gas and forms excited species via electron impacts. One of the excited species formed in the discharge is the desired $O_2(a)$ molecule. Along with other excited species, $O_2(a)$ exits the discharge and flows downstream where iodine is injected using a helium carrier gas. Excited species dissociate the iodine molecules into atoms, which are then pumped by $O_2(a)$ to the excited state. The flow then enters the laser cavity, where mirrors are present to provide stimulated emission.

While every EOIL system needs the three components previously described, there exist variations of these components across different research groups. For instance, Rawlins *et al.* has had success using a microwave-discharge flow reactor [1.16], while Hicks et al. used a non-self-sustained pulser-sustainer discharge [1.17]. Many experimental and computational studies have been made involving the production of $O_2(a)$ from an electric discharge. Some discharge studies performed by the research group at UIUC-CUA will be discussed later in this section. Ionin *et al.* [1.18] and Heaven [1.19] provide comprehensive topical reviews of the discharge production of $O_2(a)$ and EOIL studies by various research groups.

Figure 1.4 is a schematic showing the basic components of the EOIL system being studied at UIUC-CUA. A mixture of O_2:He:NO gas enters a transverse capacitive-coupled radio frequency (RF) discharge. The gas is extremely hot after leaving the discharge (up to 700 K depending on input power and pressure) and enters a heat exchanger where excess heat is removed. Downstream from the heat exchanger, iodine gas is injected via a helium carrier gas. To further cool the flow, a tertiary flow of cold nitrogen gas is injected downstream of the iodine injectors. The flow then enters a Mach 2 nozzle which supersonically expands the flow and lowers the temperature further to promote the pumping reaction. The importance of temperature for the EOIL system will be explained in more depth in a subsequent section. The flow then

enters the laser cavity where high-reflectivity mirrors are present to facilitate stimulated emission. The out-coupled laser beam emerges from the cavity.

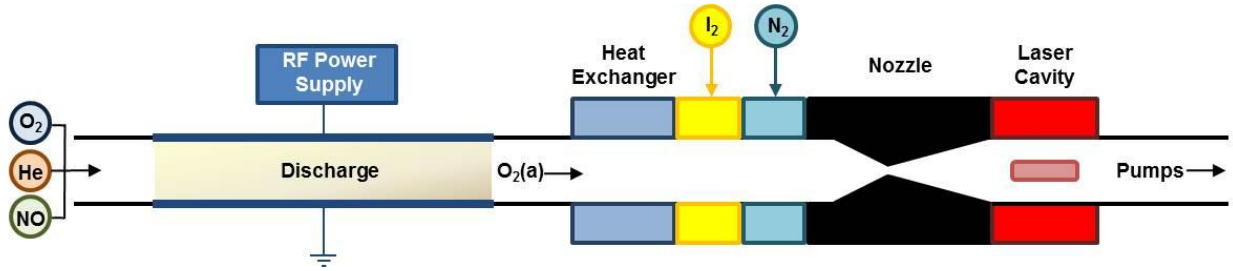

Figure 1.4. Schematic showing the basic components of the EOIL system at UIUC-CUA. This is a side view, with the flow moving from left to right and the laser beam emerging out of the page. The sketch is not to scale.

1.5 Chemical Kinetics in EOIL

One of the major differences between EOIL and COIL involve the chemical kinetics. In COIL, the only major outputs from the SOG are $O_2(a)$ and small amounts of water vapor. The iodine is injected downstream of the SOG using a flow of helium or nitrogen gas. The limited number of input and excited species allows for the chemical kinetics in COIL systems to be more easily understood. This simplicity also allows the chemical kinetics in COIL to be modeled and predicted more easily.

On the other hand, the use of an electric discharge with EOIL results in the production of many more excited species besides the desired $O_2(a)$ state. Two of the more important players in EOIL kinetics are oxygen atoms (also denoted as O atoms) and the excited $O_2(b^1\Sigma)$ state [also denoted as $O_2(b)$], which is at an energy of 1.63 eV [as compared to $O_2(a)$ which is at 0.98 eV]. Along with other species, both O atoms and $O_2(b)$ are products of the discharge. This is different from COIL systems in which no O atoms are present and the concentration of $O_2(b)$ is very low [1.20].

The presence of oxygen atoms and $O_2(b)$ has a dramatic effect on EOIL kinetics. Very early in EOIL development, it was thought that the $O_2(a)$ energy loss during iodine dissociation would kill any chance of a laser operating effectively. This is due to the fact that $O_2(a)$ yields in EOIL are smaller than the yields seen in COIL, and the I_2 dissociation method in COIL is based solely on $O_2(a)$. This energy loss was thought to be so detrimental to laser performance that the injection of predissociated iodine atoms would be necessary for EOIL systems to function [1.11].

It was latter realized that O atoms play a major role in dissociating the I_2 molecule [1.21], thus allowing the energy in $O_2(a)$ to be spent pumping the laser state. The dissociation of the I_2 molecule by O atoms occurs through the following mechanisms given in Equations (1.3) and (1.4).

$$O + I_2 \longrightarrow IO + I \quad (1.3)$$

$$O + IO \longrightarrow O_2 + I \quad (1.4)$$

While O atoms have been beneficial at their ability to dissociate I_2, they have also proven to bring deleterious effects to laser performance. For example, O atoms have been found to quench the excited I* state by the following mechanism given in Equation (1.5) [1.22].

$$I^* + O \longrightarrow I + O \quad (1.5)$$

Besides I* quenching, O atoms also directly quench $O_2(a)$ through a three-body process [1.23]. Therefore, O atoms play both positive and negative roles in the kinetics downstream from the discharge.

Since they have such a dramatic effect on system kinetics, mechanisms have been put in place to better control the effects of O atoms. For instance, trace amounts of nitrogen dioxide (NO_2) and/or NO gases were added to the flow in order to scavenge O atoms. The process of scavenging O atoms occurs through the following mechanisms given as Equations (1.6) and (1.7).

$$NO_2 + O \longrightarrow NO + O_2 \quad (1.6)$$

$$NO + O \longrightarrow NO_2^* \quad (1.7)$$

The addition of NO also somewhat enhances discharge production of $O_2(a)$ by lowering the average ionization threshold of the gas mixture. The NO gas has a lower ionization threshold than the other species entering the discharge. Therefore, NO enhances the production of electrons, increases the conductivity of the plasma, and reduces the electric field needed to sustain the plasma. The addition of NO also causes an “air afterglow” in which a very large broadband emission of NO_2^* is seen. This process is given in Equation (1.8).

$$NO_2^* \longrightarrow NO_2 + h\nu \quad (1.8)$$

The NO "air afterglow" allows the O atom concentration to be determined. However, it also disrupts other spectroscopic tools. This will be discussed in more detail in a subsequent section.

1.6 Discharge Geometry in EOIL

In addition to studying chemical kinetic mechanisms, a great deal of research has been performed on discharge geometries. Nearly all of the discharges used by the research group at UIUC-CUA have been an RF type and usually operated at 13.56 MHz. The three major designs include inductively-coupled, longitudinal capacitive-coupled, and transverse capacitive-coupled. Figure 1.5 shows a diagram of the three different discharge designs. In the inductively-coupled discharge, the power enters the gas by sending electric current through a coil wrapped around the flow tube. In the longitudinal capacitive-coupled discharge, a voltage is applied to electrodes that are separated along the flow axis. In the transverse capacitive-coupled discharge, a voltage is applied to electrodes that are on the top and bottom of the tube such that the current path is transverse to the flow direction. The longitudinal capacitive-coupled discharge was used in the experiments that lead to the first measurements of gain and laser power in an EOIL system.

Figure 1.5. Various RF discharge configurations: (a) inductively-coupled, (b) longitudinal capacitive-coupled, (c) transverse capacitive-coupled [Adapted from 1.24].

More experiments were carried out with the transverse capacitive-coupled discharges to determine the best geometry and discharge configuration. Experiments were conducted by Zimmerman *et al.* [1.25] and Woodard *et al.* [1.26] to examine the influence of frequency, geometry, pressure, and diluent ratio on $O_2(a)$ production. Zimmerman *et al.* found that a low current density homogeneous discharge resulted in the best $O_2(a)$ production. Both Zimmerman *et al.* and Woodard *et al.* found that shortening the gap between the electrodes at higher discharge pressures (50-100 Torr versus 20 Torr) more effectively creates $O_2(a)$. Reducing the transverse gap, while maintaining the volume between the electrodes allows low power density to be maintained. It also results in residence time to be maintained to allow removal of oxygen

atoms by wall recombination and reactions with NO. This is an important finding as EOIL has been moving toward higher operating pressures as the laser size has increased.

Since a narrow electrode gap was found to result in better $O_2(a)$ yields, smaller diameter discharge tubes were studied. However, the disadvantage of smaller tubes was that they limited the amount of gas that could flow through them without causing substantial pressure rises in the discharge [with the pressure rises being detrimental to $O_2(a)$ production]. To maintain the small discharge gap, the researchers at UIUC-CUA began experimenting with rectangular cross-section discharge tubes [1.27]. The rectangular cross-section discharge tube maintains the good discharge characteristics by having a small gap, while permitting higher flow rates without a substantial pressure rise. A schematic showing the cross-section of the quartz rectangular discharge tube and a photograph of the discharge tube during experimentation can be seen in Figure 1.6.

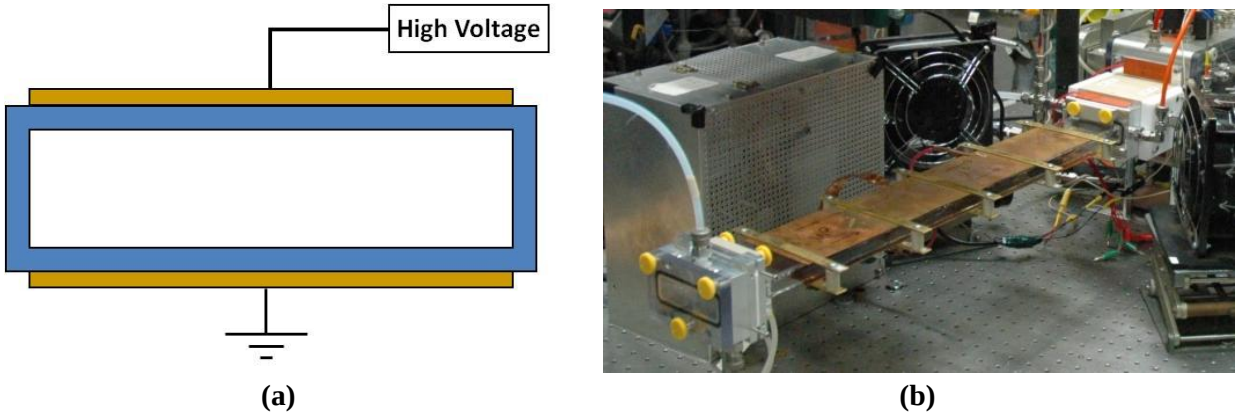

(a) **(b)**

Figure 1.6. (a) Schematic showing the cross-section of the rectangular quartz discharge tube with the two copper electrodes. The drawing is not to scale and the flow goes into the page. (b) Photograph of the rectangular quartz discharge tube during experimentation.

An alternative design to the rectangular cross-section tube was to use multiple small diameter circular tubes. The small diameter tubes would allow the desired small gap to be used, and adding more tubes would allow operation at higher flow rates. A schematic showing the cross-section of the multi-tube (also referred to as "6-tube") discharge and a photograph of the discharge tubes can be seen in Figure 1.7. A detailed discussion about the performance of the quartz rectangular cross-section tube and 6-tube discharges can be found in Woodard *et al.* [1.28].

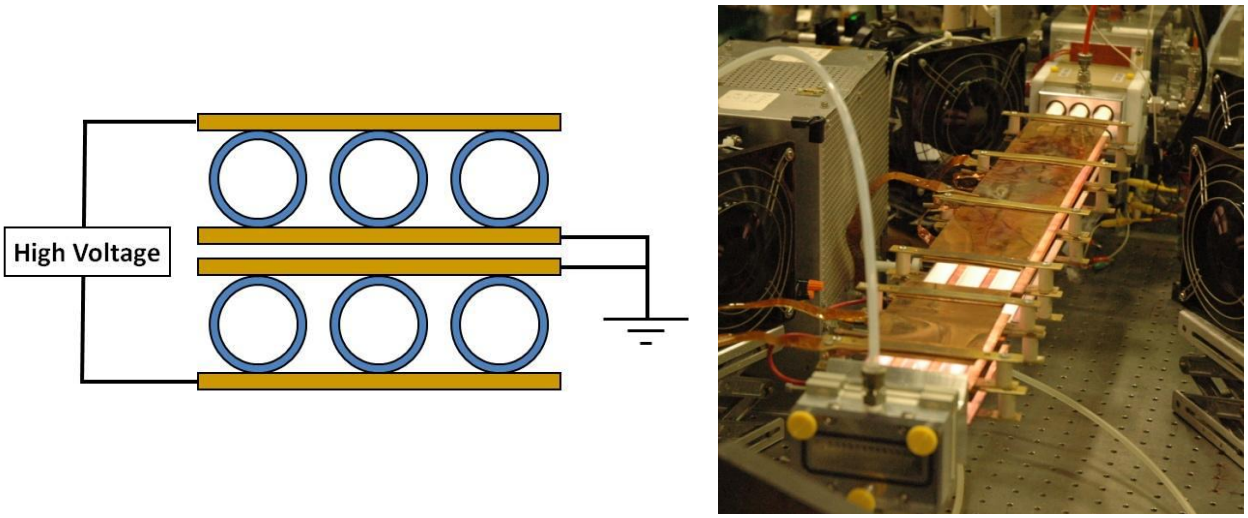

(a) **(b)**

Figure 1.7. (a) Schematic showing the cross-section of the "6-tube" discharge with the outer copper electrodes at high voltage and the inner electrodes grounded. The drawing is not to scale and the flow goes into the page. (b) Photograph of the "6-tube" discharge during experimentation.

During discharge geometry studies, two rectangular quartz discharge tubes were used in experiments. While the tubes gave very good $O_2(a)$ yields, they eventually experienced structural failures. The structural failures occurred due to the high stresses experienced by the rectangular shape while under vacuum pressure. In an attempt to strengthen the discharge tube and retain the rectangular cross-section geometry, an additional tube was fabricated out of alumina. Alumina is a much more rigid material and was thought to be able to withstand the high stresses of a vacuum system. A schematic showing the cross-section of the rectangular alumina tube and a photograph of the discharge tube can be seen in Figure 1.8. However, the rectangular alumina tube also experienced structural failures. Therefore, the rectangular cross-section discharge design was abandoned.

Due to the structural problems associated with the rectangular design, a new discharge geometry was proposed to maintain the small discharge gap but retain structural rigidity under vacuum system conditions. Since the circular cross-section tubes are best suited for the stresses of a vacuum system, a coaxial discharge was designed in which inner and outer circular cross-section tubes and electrodes form a discharge. The inner and outer tubes were made from quartz. Water was passed through the hollow inner electrode to prevent the electrode from melting. A schematic showing the cross-section of the concentric discharge and a photograph of the discharge can be seen in Figure 1.9.

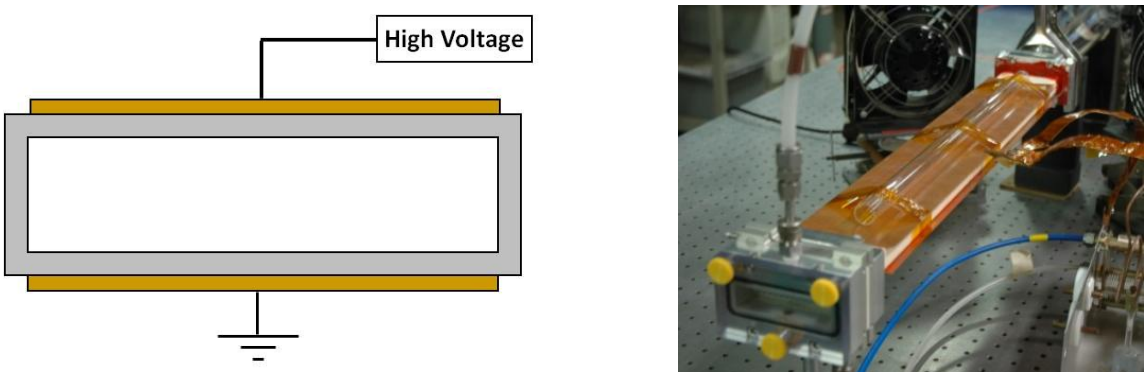

(a) (b)

Figure 1.8. (a) Schematic showing the cross-section of the rectangular alumina discharge tube. The drawing is not to scale and the flow goes into the page. (b) Photograph of the "rectangular alumina" discharge tube during experimentation.

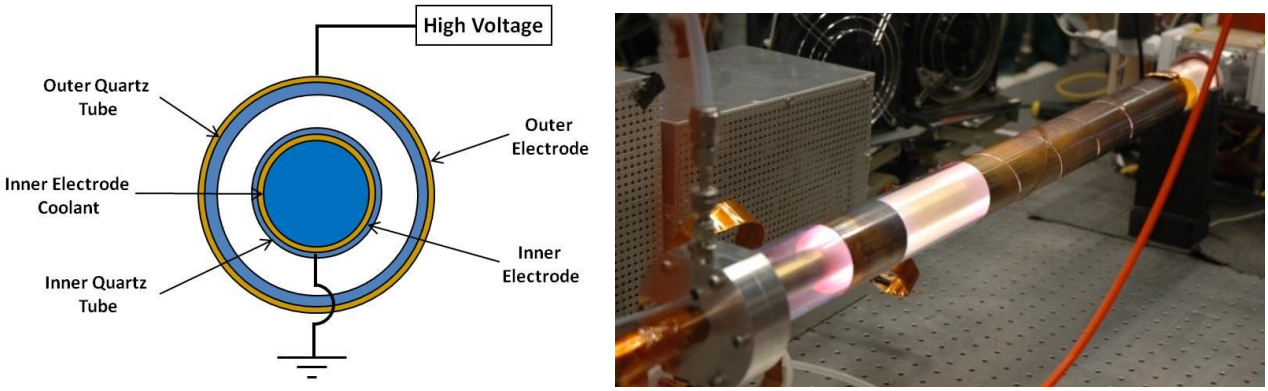

(a) (b)

Figure 1.9. (a) Schematic showing the cross-section of the concentric discharge. An outer copper electrode surrounds the outer quartz tube. A hollow brass cylinder serves as the inner electrode and is water-cooled. The drawing is not the scale and the flow goes into the page. (b) Photograph of the concentric discharge during experimentation.

1.7 Laser Cavity Configurations in EOIL

In addition to improving the discharge, different laser cavity designs have been studied and implemented to obtain higher gains and laser power. Improvements to the laser cavity hardware are constantly being discovered and employed. The hardware used for taking data for this thesis was the sixth generation "Cav6" laser cavity. A major improvement to Cav6 versus the fifth generation laser cavity was an increased gain length from 5.1 cm to 7.6 cm [1.27].

Along with the increased gain length, Cav6 also allowed many different resonator configurations to be studied. Typical two-mirror stable resonators were tested with 5 cm (2 in.) and 10 cm (4 in.) diameter optics. Also, four-mirror folded resonator designs using 5 cm diameter optics were also tested. These designs, stable X and Z-resonators (named based on the shape of the optical path) resulted in highest outcoupled laser power of 102 W and 109 W, respectively. Figure 1.10 shows cutaway views of the various resonator configurations that were tested with Cav6 hardware. Current work is being done to design the next generation Cav7 laser cavity.

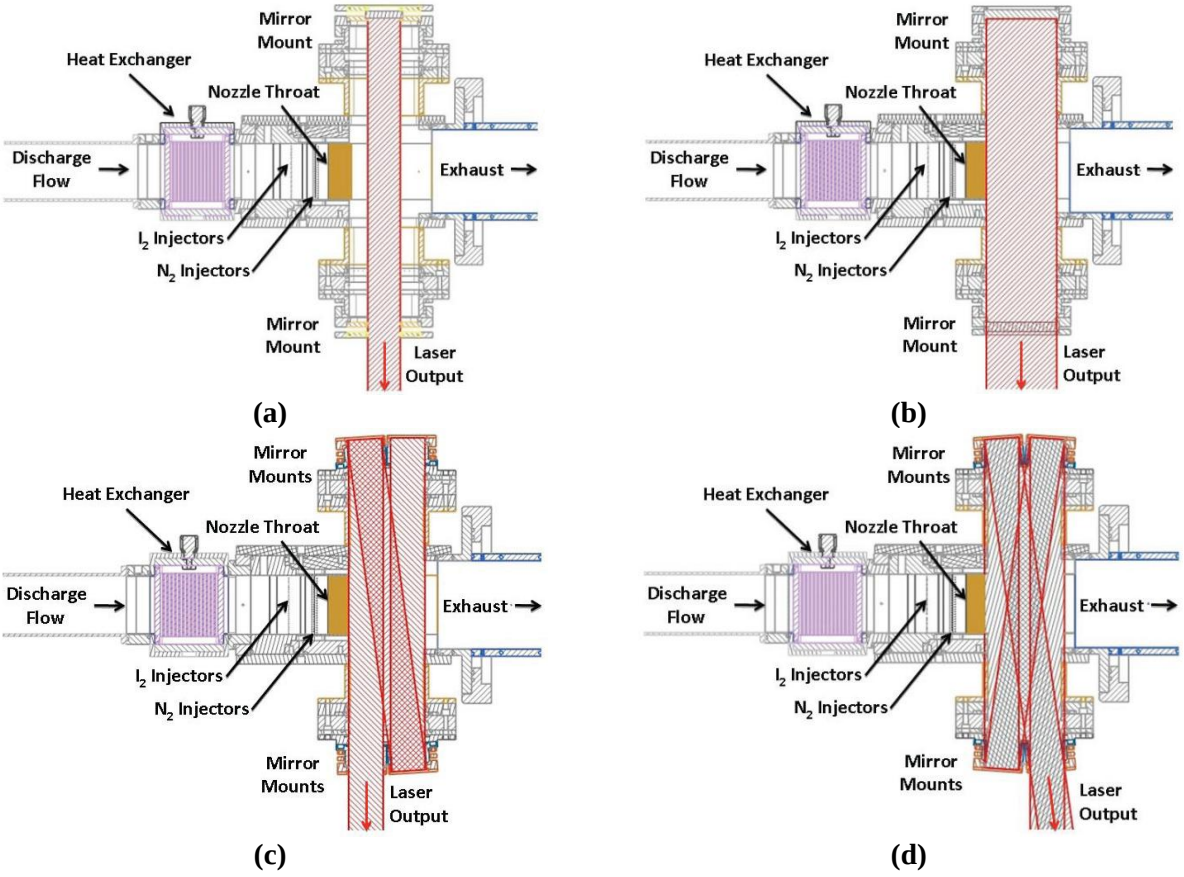

Figure 1.10. Top cutaway view of various resonator configurations tested with Cav6 hardware. Standard, stable resonators with (a) 5 cm diameter and (b) 10 cm diameter mirrors. (c) Stable Z-resonator and (d) stable X-resonator with 5 cm diameter mirrors [1.29].

1.8 Increasing Gain and Laser Power in EOIL

The research group at UIUC-CUA has been the leader in gain and power measurements for EOIL technology. By studying chemical kinetics and discharge production of $O_2(a)$ the

research group has been able to make large strides to increase gain and laser power in the EOIL system. Advances to laser cavity hardware has also resulted in increased gain length and allowed different resonator configurations to be implemented. An overview of the gain and power milestones made during the past few years is given in Table 1.1.

Table 1.1. History of EOIL Gain and Laser Power at UIUC-CUA

Year	Gain [% cm^{-1}]	Laser Power [W]	Ref.
2004	0.002	NA	[1.12]
2005	0.0067	0.220	[1.15]
2005	0.0156	0.510	[1.30]
2006	0.009	0.540	[1.31]
2006	0.022	1.47	[1.32]
2006	0.027	1.47	[1.33]
2007	0.067	4.5	[1.34]
2008	0.10	6.2	[1.35]
2008	0.17	12.3	[1.36]
2009	0.22	28	[1.37]
2009	0.26	54.8	[1.27]
2010	0.26	102.5	[1.38]
2010	0.26	109	[1.29]

1.9 References

[1.1] Verdeyen, J.T., *Laser Electronics*, Third Edition, Englewood Cliffs, NJ: Prentice-Hall (1995).

[1.2] Endo, M., and Walter, R. F., *Gas Lasers*, Boca Raton, FL: CRC Press, Taylor & Francis Group (2007).

[1.3] Kasper, J.V.V. and Pimentel, G.C., Atomic iodine photodissociation laser, *Appl. Phys. Lett.* 5, 231 (1964).

[1.4] Derwent, R.G., Kearns, D.R., and Thrush, B.A., The excitation of iodine by singlet molecular oxygen, *Chem. Phys. Lett.* 6(2), 115 (1970).

[1.5] McDermott, W.E., Pchelkin, D., Bernard, D.J., and Bousek, R.R., An electronic transition chemical laser. *Appl. Phys. Lett.* 32, 469 (1978).

[1.6] Truesdell, K.A., Helms, C.A., and Hager, G.D., A History of Coil Development in the USA. *Proc. SPIE* 2502, 217 (1994).

[1.7] Barmashenko, B.D. and Rosenwaks, S., Power dependence of chemical oxygen-iodine lasers on iodine dissociation, *AIAA J.* 34, 2569 (1996).

[1.8] Airborne Laser Test Bed (ALTB), *U.S. Department of Defense: Missile Defense Agency*, Accessed Online: 27 February 2011 <http://www.mda.mil/system/altb.html>.

[1.9] Airborne Laser Test Bed Successful in Lethal Intercept Experiment, *U.S. Department of Defense: Missile Defense Agency*, Accessed Online: 27 February 2011 <http://www.mda.mil/news/10news0002.html>.

[1.10] Henshaw, T.L., Madden, T.J., Manke, G.C., Anderson, B.T., Tate, R.F., Berman, M.R., Hager, G.D., Recent experimental results in the development of an all gas phase iodine laser, *AIAA 31st Plasmadynamics and Lasers Conference*, 19-22 June 2000, AIAA Paper 2000-2424.

[1.11] Carroll, D.L. and Solomon, W.C. ElectriCOIL: An Advanced Chemical Iodine Laser Concept, *Proceedings of the XIII International Symposium on Gas Flow and Chemical Lasers and High Power Laser Conference*, 18-22 September 2000, Florence, Italy, *SPIE*, 4184, pp. 40-44 (2000).

[1.12] Carroll, D.L., Verdeyen J.T., King, D.M., Zimmerman, J.W., Laystrom, J.K., Woodard, B.S., Richardson, N., Kittell, K., Kushner, M.J., and Solomon, W.C., Measurement of positive gain on the 1315 nm transition of atomic iodine pumped by $O_2(a^1\Delta)$ produced in an electric discharge, *Appl. Phys. Lett.* 85, 8, pp. 1320-1322 (2004).

[1.13] Zalesskii, V.Y., Gas-discharge laser operating on 1315 nm iodine transition, *Sov. Phys. JETP* 40 (1) 14 (1975).

[1.14] Fournier, G., Bonnet, J., and Pigache, D., Potential atomic iodine laser pumped by electrically generated $^1\Delta$ oxygen." *J. Physique. Colloque*, 41, 11, pp 449-453, (1980).

[1.15] Carroll, D.L., Verdeyen J.T., King, D.M., Zimmerman, J.W., Laystrom, J., Woodard, B.S., Benavides, G.F., Kittell, K., Stafford, D.S., Kushner, M.J., and Solomon, W.C., Continuous-wave laser oscillation on the 1315 nm transition of atomic iodine pumped by $O_2(a^1\Delta)$ produced in an electric discharge, *Appl. Phys. Lett.* 86, 111104-1 (2005).

[1.16] Rawlins, W.T., Lee, S., Kessler, W.J., and Davis, S.J., Observations of gain on the $I(^2P_{1/2}\rightarrow{}^2P_{3/2})$ transition by energy transfer from $O_2(a^1\Delta_g)$ generated by a microwave discharge in a subsonic-flow reactor, *Appl. Phys. Lett.* 86, 051105 (2005).

[1.17] Hicks, A., Utkin, Yu. G., Lempert, W.R., Rich, J.W. and Adamovich, I.V., Continuous wave operation of a non-self-sustained electric discharge pumped oxygen-iodine laser, *Appl. Phys. Lett.* 89, 241131 (2006).

[1.18] Ionin, A.A., Kochetov, I.V., Napartovich, A.P., and Yuryshev, N.N., Physics and engineering of singlet delta oxygen production in low-temperature plasma, *J. Phys. D: Appl. Phys.* 40, R25 (2007).

[1.19] Heaven, M.C., Recent advances in the development of discharge-pumped oxygen-iodine lasers, *Laser Photonics Rev.* 4, No. 5, 671-683 (2010).

[1.20] Carroll, D.L., Verdeyen J.T., King, D.M., Woodard, B.S., Skorski, L.W., Zimmerman, J.W., and Solomon, W.C., Recent Work on the Development of an Electric Discharge Oxygen Iodine Laser, *Proceedings of the XIV International Symposium on Gas Flow and Chemical Lasers and High Power Laser Conference*, 26-30 August 26-30 2002, Wroclaw, Poland, *SPIE*, Vol. 5120 (2003).

[1.21] Atkinson, R., Baulch, D.L., Cox, R.A., Hampson, R.F. Jr., Kerr, J.A., Rossi, M.J., and Troe, J., *J. Phys. Chem. Ref. Data*, 26, 3 pp. 550-962 (1997).

[1.22] Azyazov, V.N., Antonov, I.O., Ruffner, S., and Heaven, M.C., Quenching of $I(^2P_{1/2})$ by O_3 and $O(^3P)$, *SPIE*, Vol. 6101, 61011Y (2006).

[1.23] Rakhimova, T.V., Kovalev, A.S., Rakhimov, A.T., Klopovsky, K.S., Lopaev, D.V., Mankelevich, Y.A., Proshina, O.V., Braginsky, O.V., and Vasilieva, A.N., Radio-Frequency Plasma Generation of Singlet Oxygen in O_2 and O_2:Ar (He) Mixtures, *AIAA 34th Plasmadynamics and Lasers Conference*, 23-26 June 2003, AIAA Paper 2003-4306.

[1.24] Zimmerman, J.W., *Studies of Oxygen-Helium Discharges for Use in Electric Oxygen-Iodine Laser*, University of Illinois PhD Thesis (2010).

[1.25] Zimmerman, J.W., Woodard, B.S., Verdeyen, J.T., Carroll, D.L., Field, T.H., Benavides, G.F., and Solomon, W.C., Influence of frequency of $O_2(a^1\Delta)$ and oxygen atom production in transverse radio-frequency discharges, *J. Phys. D: Appl. Phys.* 41, 195209 (2008).

[1.26] Woodard, B.S., Zimmerman, J.W., Verdeyen, J.T., Carroll, D.L., Field, T.H., Benavides, G.F., Palla, A.D., and Solomon, W.C., Improved production of $O_2(a^1\Delta)$ in transverse radio-frequency discharges, *HPLA 2008 Conference*, 21-24 April 2008, *SPIE* Vol. 7005, pp. 70051L-1-9 (2008).

[1.27] Benavides, G.F., Zimmerman, J.W., Woodard, B.S., Carroll, D.L., Palla, A.D., Day, M.T., Verdeyen, J.T., and Solomon, W.C., Enhancement of electric oxygen-iodine laser performance using a rectangular discharge and longer gain length, *Appl. Phys. Lett.* 95, 221112 (2009).

[1.28] Woodard, B.S., Zimmerman, J.W., Benavides, G.F., Day, M.T., Palla, A.D., Carroll, D.L., Verdeyen, J.T., and Solomon, W.C., Investigation of the Production of $O_2(a^1\Delta)$ in Rectangular and Multi-Tube Radio-Frequency Discharges, *AIAA 41st Plasmadynamics and Lasers Conference*, 28 June - 1 July 2010, AIAA Paper 2010-5040.

[1.29] Zimmerman, J.W., Benavides, G.F., Woodard, B.S., Day, M.T., Carroll, D.L., Palla, A.D., Verdeyen, J.T., and Solomon, W.C., Electric Oxygen-Iodine Laser Performance Enhancement using Larger Discharge and Resonator Mode Volumes, *AIAA 41st Plasmadynamics and Lasers Conference*, 28 June - 1 July 2010, AIAA Paper 2010-5038.

[1.30] Carroll, D.L., Verdeyen J.T., King, D.M., Zimmerman, J.W., Laystrom, J.K., Palla, A.D., Woodard, B.S., Benavides, G.F., Kittell, K., and Solomon, W.C., Recent Experiments and Post-Discharge Modeling with the ElectricOIL Laser System, *Proc. of the ICONO/LAT 2005 Conference*, St. Petersburg, Russia, 10-15 May 2005.

[1.31] Verdeyen J.T., Carroll, D.L., King, D.M., Laystrom, J.K., Benavides, G.F., Zimmerman, J.W., Woodard, B.S., and Solomon, W.C., Continuous-wave laser oscillation in subsonic flow on the 1315 nm atomic iodine transition pumped by electric discharge produced $O_2(a^1\Delta)$, *Appl. Phys. Lett.* 89, pp. 101115 (2006).

[1.32] King, D.M., Carroll, D.L., Verdeyen J.T., Laystrom, J.K., Benavides, G.F., Palla, A.D., Zimmerman, J.W., Woodard, B.S., and Solomon, W.C., Power Enhancement of the Hybrid ElectricOIL Laser, AIAA Paper 2006-3756, *AIAA 37th Plasmadynamics and Lasers Conference*, 5-8 June 2006, AIAA Paper 2006-3756.

[1.33] Carroll, D.L., Verdeyen J.T., King, D.M., Palla, A.D., Laystrom, J.K., Benavides, G.F., Zimmerman, J.W., Woodard, B.S., and Solomon, W.C., Development of the electric discharge oxygen-iodine laser, *Proceedings of the XVI International Symposium on Gas Flow and Chemical Lasers and High Power Laser Conference*, Gmunden, Austria, 4-8 September 2006, *SPIE*, Vol. 6346, pp. 63460H-1-63460H-8 (2006).

[1.34] Benavides, G.F., Palla, A.D., King, D.M., Carroll, D.L., Verdeyen J.T., Laystrom, J.K., Field, T.H., Zimmerman, J.W., Woodard, B.S., and Solomon, W.C., Hybrid ElectricOIL Discharge, Gain, and Power Enhancements, *AIAA 38th Plasmadynamics and Lasers Conference*, 25-28 June 2007, AIAA Paper 2007-4623.

[1.35] Benavides, G.F., Zimmerman, J.W., Woodard, B.S., Carroll, D.L., Verdeyen, J.T., Field, T.H., Palla, A.D., and Solomon, W.C., Gain and continuous-wave laser power enhancement with a secondary discharge to pre-dissociate molecular iodine in an electric oxygen-iodine laser, *Appl. Phys. Lett.* 92, pp. 041116 (2008).

[1.36] Zimmerman, J.W., Woodard, B.S., Benavides, G.F., Carroll, D.L., Verdeyen, J.T., Palla, A.D., Field, T.H., and Solomon, W.C., Gain and continuous-wave laser power enhancement with a multiple discharge electric oxygen-iodine discharge, *Appl. Phys. Lett.*, Vol. 92, pp. 241115 (2008).

[1.37] Zimmerman, J.W., Benavides, G.F., Woodard, B.S., Carroll, D.L., Palla, A.D., Verdeyen J.T., and Solomon, W.C., Measurements of Improved ElectricOIL Performance, Gain, and Laser Power, *AIAA 40th Plasma Dynamics and Lasers Conference*, 22-25 June 2009, AIAA Paper 2009-4059.

[1.38] Woodard, B.S., Benavides, G.F., Zimmerman, J.W., Carroll, D.L., Palla, A.D., Day, M.T., Verdeyen, J.T., and Solomon, W.C., Enhancement of electric oxygen-iodine laser performance using larger mode volume resonators, 15 May 2010, *Optics Letters*, Vol. 35, No. 10, pp. 1611-1613 (2010).

2. Experimental Apparatus

In this section, the experimental apparatus will be discussed in detail. In the first part of this section, the basic laboratory setup and the equipment used during experimentation will be discussed. In the latter part of this section, the hardware that makes up the EOIL system will be discussed in more detail. The EOIL system hardware includes components related to the discharge, heat exchanger, supersonic nozzle, and laser cavity. Most of the equipment described in this section was used to obtain the data presented in later sections of this thesis.

2.1 The UIUC Laser Laboratory

The EOIL research group conducts experiments in the High Energy Laser Laboratory at UIUC. The laboratory is equipped with a vacuum pumping system capable of achieving the low pressures needed for EOIL operation. The vacuum system consists of two MD-90 roots blowers operating in series with a Kinney KT-850 vacuum pump. The exhaust from the KT-850 is routed through a mist eliminator apparatus which filters oil mist from the primary exhaust gases. The exhaust then passes through a scrubber which further cleans the exhaust before it exits outside.

The EOIL system is attached to these vacuum pumps using PVC tubing. Along the flow route, numerous valves are in place to direct the pumping to one of two experiment tables in the laboratory. Having multiple experiment tables allows increased flexibility as experiments can be set-up and run on two different tables. A number of the valves are hand-operated Bray butterfly valves. Additionally, there are two pneumatic valves which open and close using pressurized nitrogen gas. A schematic showing the flow system can be seen in Figure 2.1.

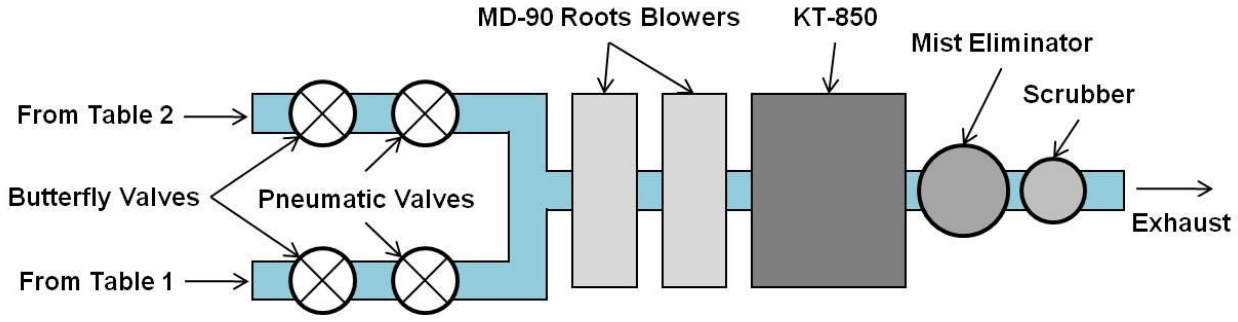

Figure 2.1 Schematic showing the setup of the vacuum pumping system used for EOIL experiments. The vacuum pumping system is routed through PVC tubing to one of two experiment tables in the laboratory. The flow moves left to right and the drawing is not to scale.

The laboratory is also well-equipped for storage of numerous bottles of oxygen and helium gas. High-pressure carrier lines, manifolds, and regulators are used to transport the gases to the experiment tables. Additionally, the laboratory is equipped with a liquid nitrogen (LN_2) storage tank. The tank provides easy access to LN_2 and also allows nitrogen gas to be drawn from the top of the tank. To measure the gas flow rate, Micro-Motion CMF and Omega FMA mass flow meters are used. The pressure is measured using capacitance manometers from MKS and Leybold.

2.2 Optical Diagnostics

In the EOIL system, many important measurements are made using optical diagnostics. These diagnostics are used to measure the emission profiles of certain excited states. Since the $O_2(a)$ molecule and I* atom emit in the near-infrared, special diagnostics are used to measure those emissions. Optical diagnostics can also be used to determine number densities of other important species in EOIL kinetics.

One of the more important pieces of equipment in the laboratory is the Princeton Instruments / Roper Scientific Optical Multi-channel Analyzer (OMA-V or OMA) which has a 1024-element InGaAs liquid nitrogen cooled array. The OMA is interfaced to an Acton Research Spectra Pro® 2300i monochromator which has 0.3 m Imaging Triple Grating and a 600 g-mm^{-1} grating blazed at 1 μm. The OMA is used to take scans of the $O_2(a)$ emission at 1268 nm. The $O_2(a)$ scans are very important during discharge optimization experiments as the scans are used to calculate the percent yield of $O_2(a)$. The process of determining $O_2(a)$ yield from an OMA scan can be found in [2.1].

Another important optical instrument is the thermoelectric-cooled Apogee E47 Charge-coupled Device (CCD) camera interfaced to an Acton Research Spectra Pro® 150 monochromator. The CCD is used to measure the emission from the $O_2(b)$ molecule at 768 nm, which is then used to calculate the gas temperature. Both the CCD and OMA are fiber-coupled using ThorLabs 600 μm × 5m multimode fibers. The use of fiber optics allows increased flexibility for instrument positioning. Instead of having to move the entire piece of equipment, the fiber optics can be moved to different measurement locations. The fiber attached to the OMA is also connected to a ThorLabs F810SMA-1310 collimator which attaches to the diagnostics block. Both the OMA and CCD can be seen in Figure 2.2.

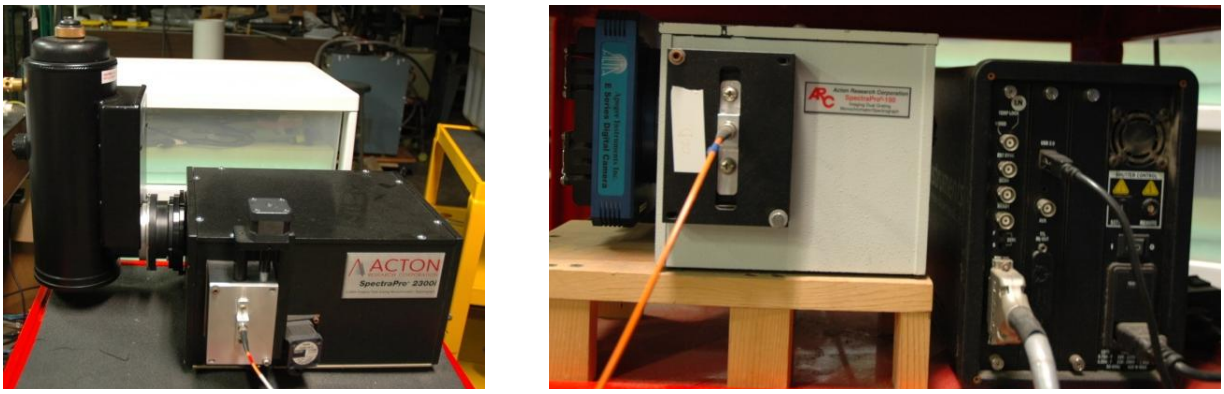

(a) **(b)**

Figure 2.2. (a) OMA used to take measurements of O_2(a) emission at 1268 nm and (b) CCD used to take measurements of O_2(b) at 768 nm. Both OMA and CCD are fiber-coupled, increasing measurement flexibility. The OMA has a collimator that attaches to the diagnostic block during experiments.

Another optical instrument used during experimentation is the Hamamatsu R955 photomultiplier tube (PMT), which measures the broadband emission of NO_2* using a narrowband 580 nm filter and a 50 mm focal length collection lens. The PMT measurement allows oxygen atom concentrations to be determined using the method described by Piper *et al.* [2.2].

The last optical diagnostic discussed in this subsection is the PSI Iodine Scan Diagnostic (ISD) which was developed by Davis *et al.* [2.3]. The ISD is used to measure the absorption or gain signal in the laser cavity. The system consists of a diode laser that generates light at 1.315 μm, which is the same wavelength as the six hyperfine transition lines of atomic iodine from $I_2(P_{1/2})$ to $I_2(P_{3/2})$. The ISD determines the fractional absorption or gain by detecting the on and off resonant line intensity.

The ISD consists of two diode lasers. One laser beam is passed through anti-reflection windows and into the gain region. The beam then exits the gain region and is focused on a detector. If positive gain is occurring, original beam is amplified and the signal read by the detector is larger than the original signal. The other diode laser is used as a reference and is passed through a cell containing iodine gas. Since positive gain is not occurring in the reference cell, the signal read by that detector always indicates absorption. The PMT collimator and the ISD diode lasers can be seen in Figure 2.3.

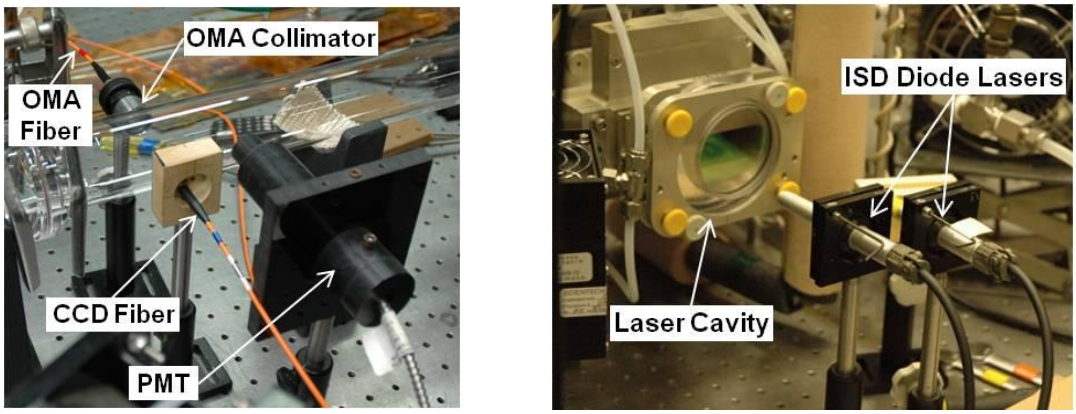

(a) **(b)**

Figure 2.3. (a) Experimental setup showing OMA fiber and collimator, CCD fiber, and PMT. These diagnostics are placed downstream of the discharge to measure O_2(a), O_2(b) and NO_2* emission. (b) The ISD lasers setup to take gain measurements at two locations in the laser cavity.

2.3 Discharge Power Supply Equipment

To obtain the excited species needed for laser operation, power must be transmitted into the flow via the discharge. The discharge power is supplied by ENI OEM-50 and ENI OEM-25A solid-state power generators that operate at 13.56 MHz. The OEM-50 is capable of input power levels of 5 kW while the OEM-25A supplies up to 2.5 kW. Attached to the power supplies are Bird Thruline model 43 wattmeters with plug-in elements to allow various power ranges to be measured. The wattmeters allow the forward and reflected power to be measured.

Matching the power from the generators to the discharge is accomplished using a traditional PI-matching network. The matching network is a set of capacitors and inductors used to match the RF power from the power supply to the discharge. The capacitor and inductor settings can be varied based on the discharge geometry to best couple the power into the gas. A detailed description of the matching network design can be found in Zimmerman [2.4]. Figure 2.4 shows photographs of the power supply equipment used in the laboratory.

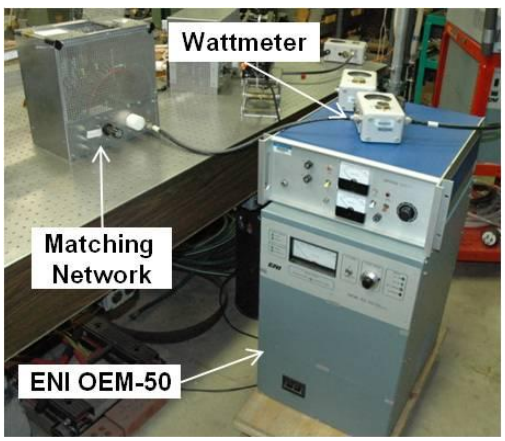

(a)

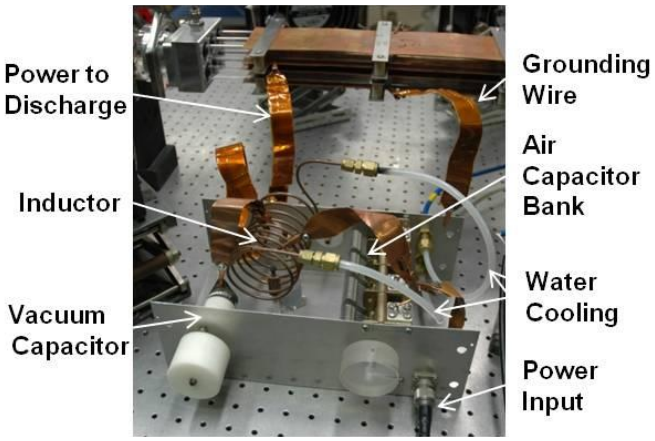

(b)

(c)

(d)

Figure 2.4. (a) Experimental setup showing the ENI OEM-50 solid-state power generator, the wattmeter, and the PI-matching network. (b) Internal components of the matching network which matches the power from the generators into the flow. (c) ENI OEM-25A solid-state power generator. (d) Wattmeter used to measure forward and reflected powers.

2.4 Laser Power Equipment

Laser power measurements are made with Scientech Astral™ model AC5000 and UC150HD40 calorimeters interfaced to a pair of Scientech Vector™ model S310 readouts. In some laser cavity configurations, the beam area is too wide to fit on the power meters. Therefore, a plano-convex lens model LPX-101.6-131.8-C with anti-reflective coating from 1050-1600 nm from CVI is used to focus the laser beam on the power meter. Also, special infrared detection cards are used to observe the beam profile since the laser emits in the infrared. The infrared cards are New Focus, Model 5842 and respond to light from 800-1600 nm. The beam profile is also observed by burning black polycarbonate plates. Figure 2.5 shows the equipment setup to measure laser power during an experiment. Laser mirrors were purchased from AT Films, Los Gatos Research, and CVI. Numerous reflectivity sets were used during experimentation based on the specific cavity configuration.

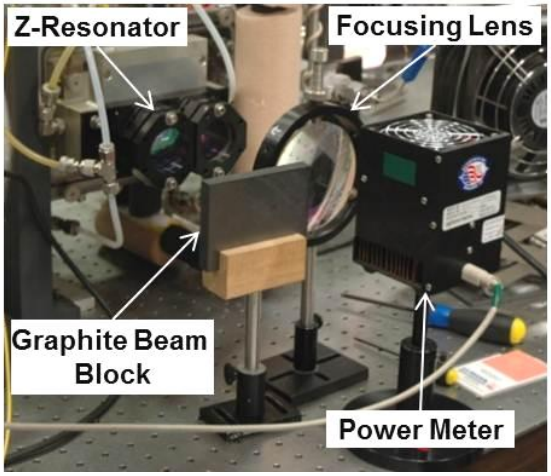

Figure 2.5. Experimental setup showing hardware used to measure laser power. The laser beam emerges from the low reflector (right mirror) of the Z-resonator and is focused on the power meter using a lens. A low power beam emerges from the high reflector (left mirror) and is blocked using a graphite beam block.

2.5 Discharge Hardware

As mentioned in the previous section, numerous experiments were conducted on discharge geometry. Since the discharge experiments were conducted concurrently with the research presented in this thesis, the data presented in this thesis comes from various discharge geometries. Therefore, the hardware that makes up each discharge will be briefly discussed.

The first discharge that will be discussed is the rectangular quartz. In order to examine the effect of discharge length on $O_2(a)$ production, tube lengths of 610 mm (2 ft.) and 1200 mm (4 ft.) were fabricated by Technical Glass Products. Both tubes had inner flow dimensions of 75 mm in width by 16 mm in height (3 mm wall thickness) for a cross-sectional flow area of 1200 mm^2. Copper plate electrodes were held in place by a supporting structure made of titanium and insulating PEEK. Alligator clips and copper wires were used to attach one of the electrodes to the matching network and the other to ground. The quartz tubes had end flanges that attached to fabricated end connectors specially made for the rectangular design. The upstream flange connected to an apparatus that distributed the gas flow equally in the rectangular tube, and a downstream flange connected to the heat exchanger.

Figure 2.5 shows the 610 mm and 1200 mm length rectangular quartz discharge tubes. Another photograph and schematic of the cross-section of the rectangular quartz tubes can be found in the previous section of this thesis. An additional discovery made during the experiments with the rectangular quartz tube involved the addition of a primer discharge [2.5]. The primer discharge has a shorter length electrode (but higher power densities) and facilitated proper discharge lighting.

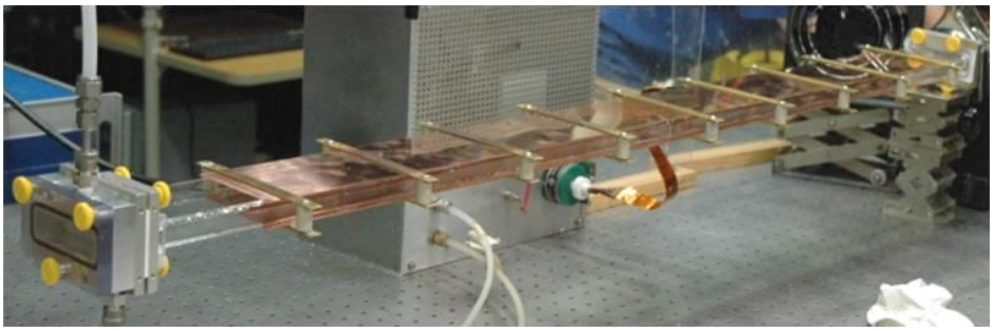

(a)

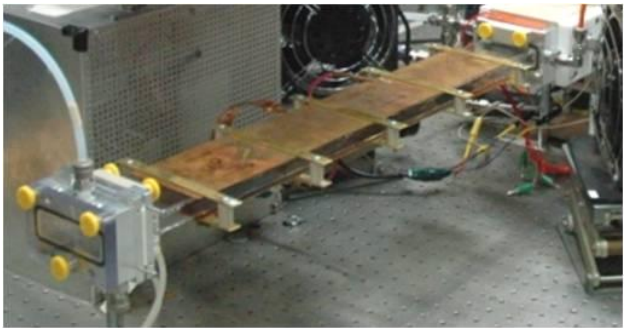

(b)

Figure 2.6. (a) Long and (b) short rectangular discharges. On the left sides, a manifold distributes the gas equally in the tubes. The copper electrodes are held to the tubes using mounts made from brass and PEEK. The flow moves left to right.

The next discharge that will be discussed is the rectangular alumina. The rectangular alumina tube was manufactured by Coors Tech. The tube did not have end flanges, so two flanges were fabricated in order to attach the tube to the EOIL system. A high-temperature epoxy was used to attach the flanges to the tube. Due to problems in the manufacturing process, the tube experienced some sagging in the middle. Therefore, a circular tube was taped to the top and bottom of the alumina tube in order to press the copper electrodes against the tube surface. A photograph and schematic of the rectangular alumina tube can be found in the previous section. The rectangular alumina tube was 610 mm (2 ft.) long and had inner flow dimensions of 70 mm (2.75 in.) in width by 13 mm (0.5 in.) in height for a total cross-sectional flow area of 910 mm^2.

The next discharge that will be discussed is the 6-tube. The 6-tube discharge used the same apparatus as the rectangular quartz discharge to distribute the flow equally in the tubes. It also used the same copper electrodes and electrode mounting hardware as the rectangular quartz. Two additional connection flanges were fabricated to connect the tubes to the distribution manifold on the upstream side and to the heat exchanger on the downstream side. The 6-tube discharge also had a primer discharge that promoted uniform discharge lighting in all six tubes. Figure 2.7 shows a photograph of the 6-tube discharge and the upstream flange used to hold the

tubes in place. Each tube was 81 cm long and had a 16 mm inner diameter (19 mm outer diameter). The total cross-sectional flow area of the 6-tube discharge was 1206 mm^2. A cross-sectional schematic of the 6-tube discharge can be found in the previous section.

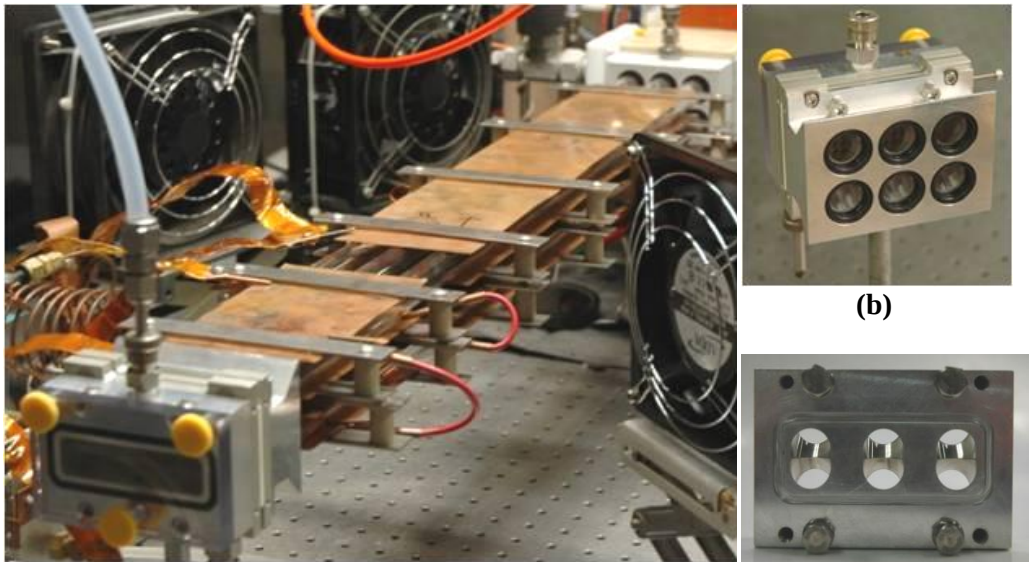

(a) **(b)** **(c)**

Figure 2.7. (a) 6-tube discharge, (b) upstream flange and flow distributor, and (c) downstream flange that connects the 6-tube discharge to the heat exchanger.

The last discharge that will be discussed is the concentric tube. There were two variations to the concentric design as the discharge gap was varied. The concentric design had upstream and downstream flanges that were specially designed to hold the two quartz tubes and inner electrode. The inner electrode was a brass cylinder with two plugs welded to the ends. The inner electrode also had a special built in water cooling system. On the upstream edge, water entered the hollow brass cylinder using a smaller diameter pipe. The pipe carried the water to the downstream edge of the brass cylinder where it exited the pipe and came into direct contact with the brass cylinder walls. The water then flowed back upstream and exited into plastic tubing.

The outer electrode was made by wrapping copper foil around the diameter of the outer tube. The outer electrode was at high voltage and the inner electrode was grounded. Figure 2.8 shows the large and short-gap concentric discharge tubes, electrode cooling system, and gas distribution manifold. Table 2.1 lists the quartz tube dimensions of the concentric discharge designs. All quartz tubes used in the concentric design were 90 cm long.

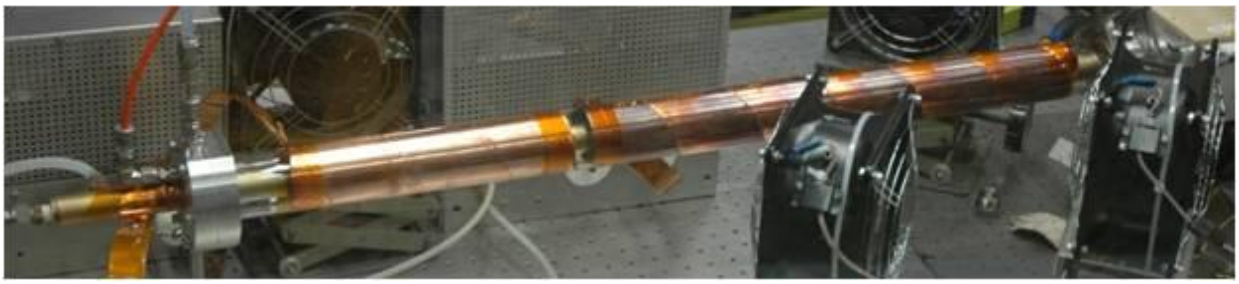

(a)

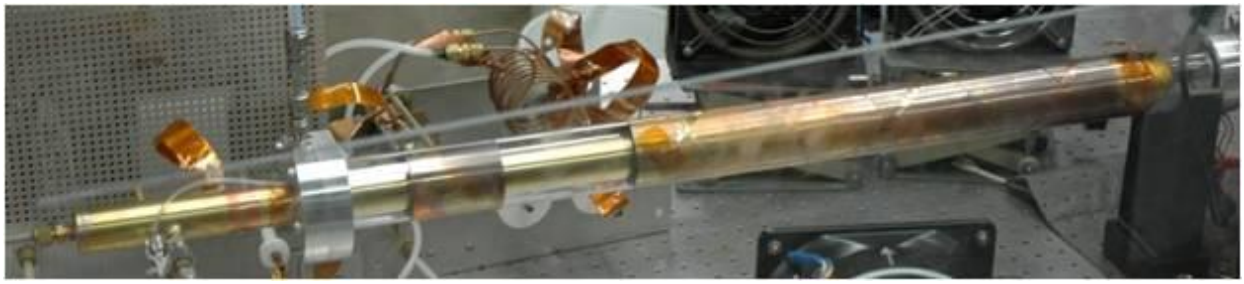

(b)

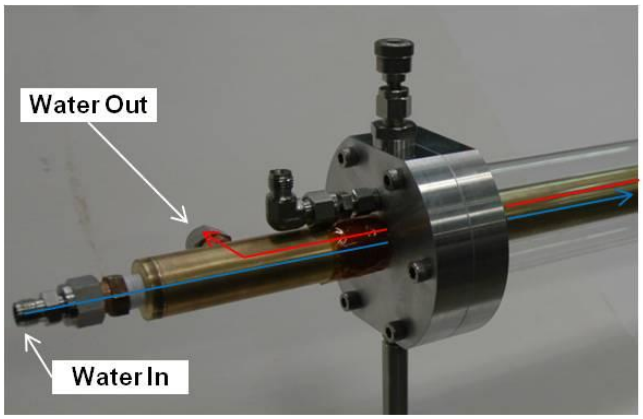

(c)

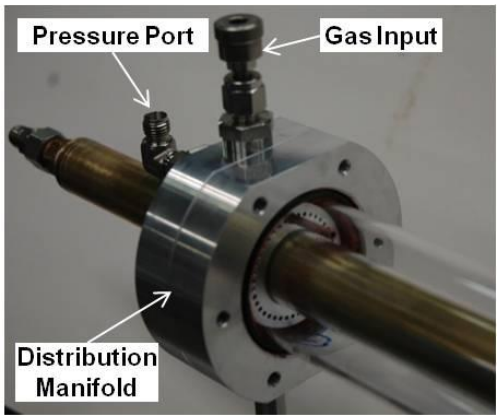

(d)

Figure 2.8. (a) Large-gap and (b) small-gap concentric discharge tubes. Both setups have an upstream primer discharge and a downstream primary discharge. The inner electrodes are brass cylinders with end caps welded on. The outer electrodes are copper foil wrapped around the outer quartz tube. The flow is from left to right. (c) Inner electrode cooling system for the large-gap concentric discharge. The water enters the electrode (blue line) and travels to the downstream side via inner tubing. The water travels back to the upstream edge (red line) and exits. (d) Close-up view of gas distribution manifold for the concentric discharge tubes. The manifold ensures even flow distribution in the discharge tube.

Table 2.1. Quartz Tube Dimensions for Concentric Discharges

Discharge Gap	Larger Tube		Smaller Tube		Cross-Sectional Flow Area [mm^2]
	OD [mm]	ID [mm]	OD [mm]	ID [mm]	
Large (23 mm)	58	52	29	26	1463
Small (15 mm)	57	53	38	35	1072

2.6 Heat Exchanger Hardware

Immediately downstream from the discharge, a heat exchanger removes excess heat from the gas. As the EOIL system has been evolving, different heat exchanger designs have been tested [2.6]. The work presented in this thesis was also used to calculate heat exchanger performance. The most obvious heat exchanger performance index is flow temperature reduction. This is accomplished by simply measuring the flow temperature after the heat exchanger. The other important performance indices are not as obvious. These include $O_2(a)$ and O atom deactivation and pressure loss. The goal of heat exchanger design in the EOIL system is to design an apparatus that maximizes temperature reduction while not quenching $O_2(a)$ molecules and keeping pressure losses at a minimum.

For this thesis, the data was taken using two different heat exchanger designs. For the first design (HEX-1), a solid block of aluminum had numerous holes drilled through in the flow direction. The holes resembled a honeycomb structure and the heat from the flow was conducted through the surface area. Additional holes were drilled perpendicular to the flow to carry the coolant. Figure 2.9 shows the internal structure of HEX-1 and also shows HEX-1 attached to the Cav6 laser configuration.

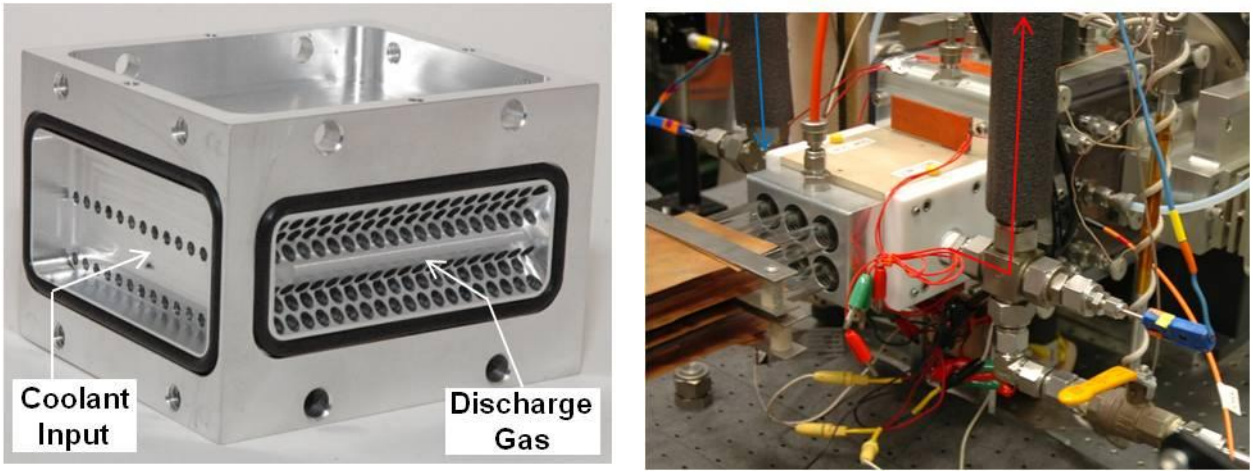

Figure 2.9. (a) Honeycomb heat exchanger (HEX-1) showing the holes through which the discharge gas pass. The coolant holes are perpendicular to the discharge gas holes and heat is carried away by the coolant. (b) Experimental setup showing HEX-1 attached to the 6-tube discharge and Cav6 laser cavity. A blue arrow is drawn to show the coolant path entering HEX-1 and a red arrow shows the coolant path as it exits the heat exchanger. Thermocouples can be seen which monitor the input and exit coolant temperature.

The next heat exchanger (HEX-2) was also fabricated from a block of aluminum. However, HEX-2 was designed so that the gas would pass through an array of tubes which carried the coolant. The heat from the gas would conduct through the tube walls and into the coolant. Figure 2.10 shows the internal structure of HEX-2 and also shows HEX-2 attached to the Cav6 laser configuration. HEX-2 was also designed in hopes that the $O_2(a)$ loss through the heat exchanger would be less than HEX-1. For both HEX-1 and HEX-2, the coolant flow rate was monitored by an Omega model FTB-1412 mass flow meter. The temperature of the coolant was also measured by thermocouples at the input and exit of the heat exchanger. The experiments performed with HEX-1 and HEX-2 will be discussed in a subsequent section of this thesis.

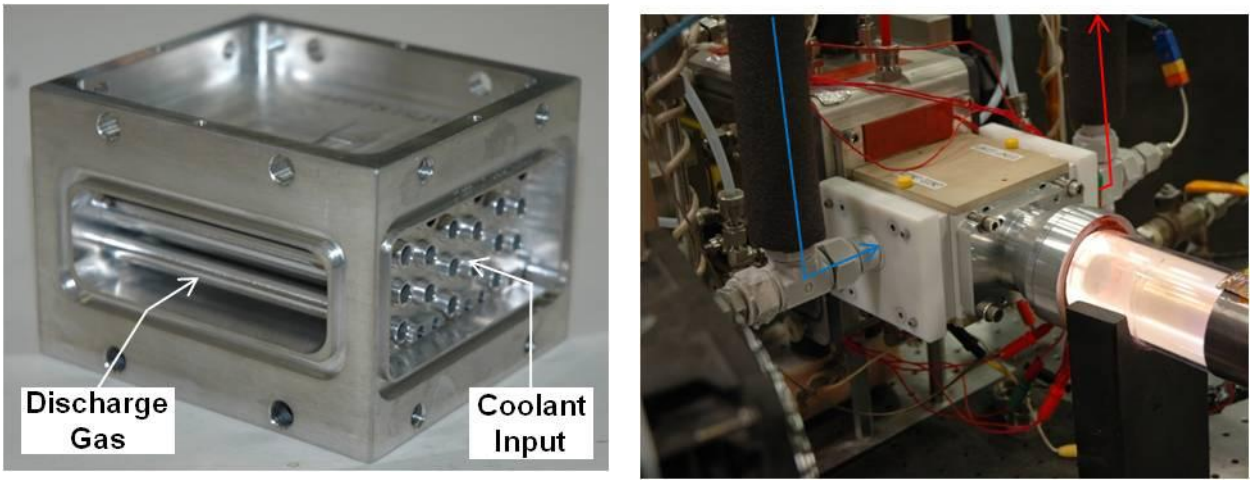

(a) **(b)**

Figure 2.10. (a) Multiple-tube heat exchanger (HEX-2) showing the tubes encountered by the hot discharge gases. The coolant flows through the tubes which run perpendicular to the flow direction. (b) Experimental setup showing HEX-2 attached to the large-gap concentric discharge and Cav6 laser cavity. A blue arrow is drawn to show the coolant entering HEX-2 and a red arrow shows the coolant path as it exits the heat exchanger. Thermocouples can be seen which monitor the input and exit coolant temperature.

2.7 Laser Cavity Hardware

After the gas exits the heat exchanger, it passes through an injection region and then is expanded into a supersonic laser cavity region. As previously mentioned, this research was conducted using Cav6 laser hardware. In Cav6, the gas enters the converging section of a nozzle and iodine gas is injected. The iodine gas is routed to the nozzle from an iodine sublimation cell

that heats crystalline iodine using heater pads. The iodine gas is carried to the nozzle using helium gas. A detailed description of the iodine sublimation cell can be found in King [2.7].

Further downstream, LN_2-cooled nitrogen gas is injected to further cool the flow. The gas then reaches the nozzle throat and expands supersonically to Mach 2. The supersonic expansion and cold gas injection further cools the flow to temperatures between 100 and 130 K. The laser mirrors are arranged around the supersonic expansion section of the nozzle. Figure 2.12 shows a schematic and photograph of the supersonic nozzle used in the Cav6 laser cavity.

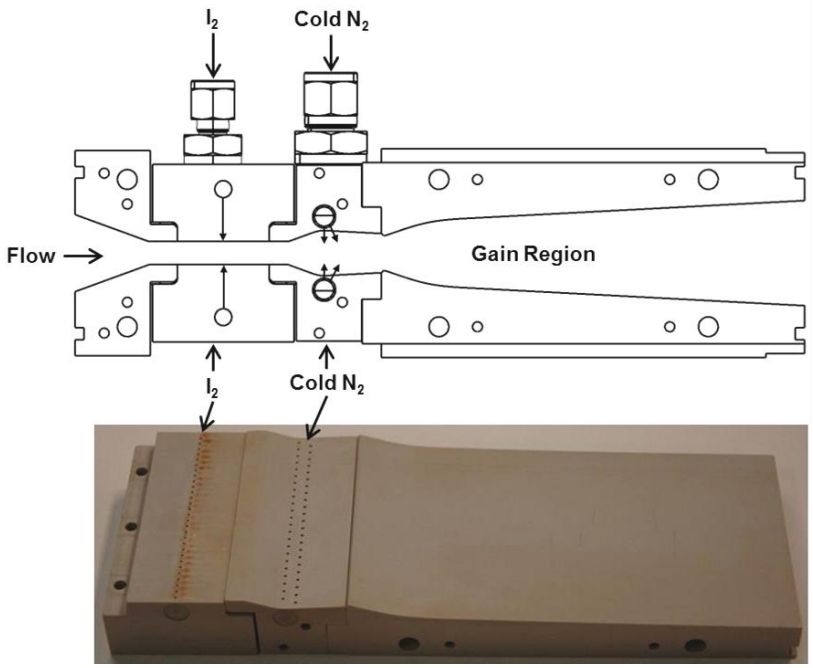

Figure 2.11. Side-view schematic and photograph of the Cav6 supersonic nozzle (flow is from left to right). The I_2 is injected by the first array of holes and the cold N_2 is injected further downstream. The gain region is in the supersonic section of the nozzle where the temperature of the gas has been lowered by the supersonic expansion and cold gas injection. The laser mirrors are arranged around the gain region.

As mentioned in the previous section, different laser resonator designs were experimented. The first resonator configuration was the standard stable two-mirror laser resonator. For the two-mirror resonator, experiments were conducted with both 5 cm (2 in.) and 10 cm (4 in.) diameter optics. Aluminum mirror mounts were fabricated that held the mirrors in place. The mirror mounts also had a built in apparatus to flow a purge gas and keep the mirrors separated from the iodine flow. The mirror mounts also had gate valves which could be closed to allow optics to be changed. Figure 2.12 shows a photograph and schematic of the stable two-mirror resonator with 10 cm diameter mirrors.

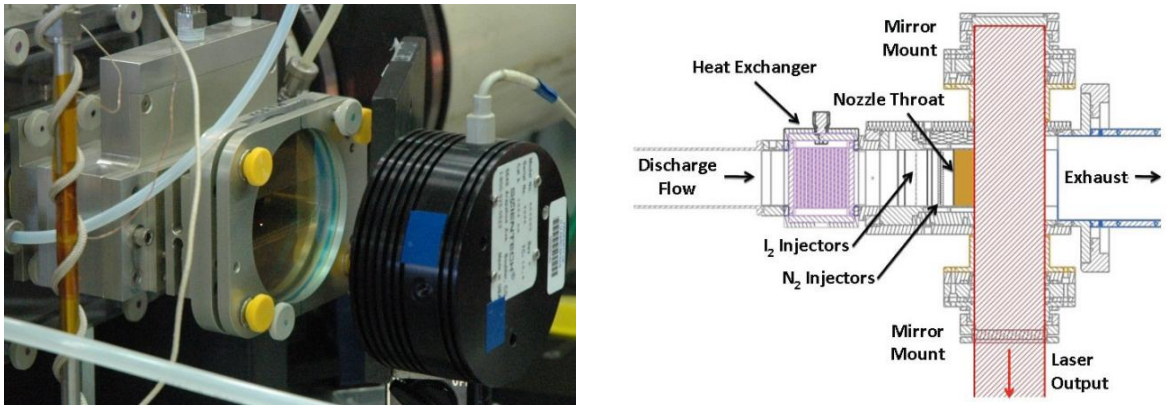

(a) **(b)**

Figure 2.12. (a) Photograph and (b) top view schematic showing the stable two-mirror laser resonator. The configuration that is shown uses 10 cm (4 in.) diameter mirrors. The Cav6 hardware also allows 5 cm (2 in.) diameter mirrors.

The other laser resonator designs included the X and Z-resonators. The hardware for the X-resonator consisted of a base plate that connected to the Cav6 mirror mount assembly. Attached to the base plate were four 5 cm (2 in.) diameter mirrors. The base plate had angled surfaces which tilted the optics inward. The X-resonator name comes from the X shape made by photons as they bounce off mirrors and travel through the gain region.

The Z-resonator had a different base plate which also connected to the mirror mount assembly. The Z-resonator differed from the X-resonator in that only one side of the base plate was angled. This meant that two mirrors were perpendicular to the flow direction while the other two mirrors were angled toward one another. The photons traveled in a Z-shaped path. The Z-resonator also used four 5 cm (2 in.) diameter mirrors. Figure 2.13 shows a photograph and top-view schematic of the X and Z-resonator hardware. At first glance, the photographs of the X and Z-resonator hardware may look the same. On closer inspection, it can be seen that the base plate for the X-resonator hardware has two angled surfaces while the Z-resonator hardware has only one.

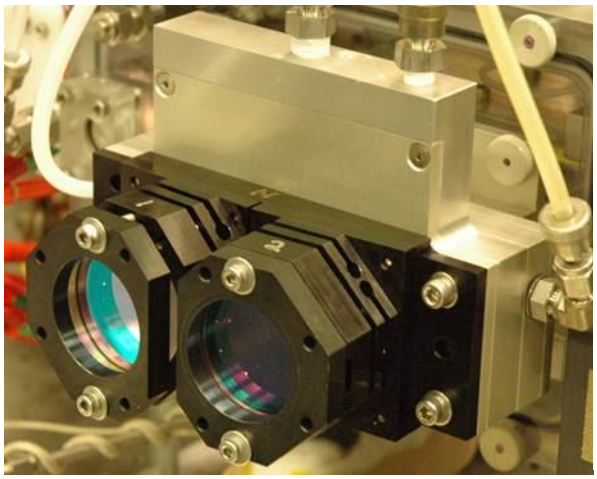

(a)

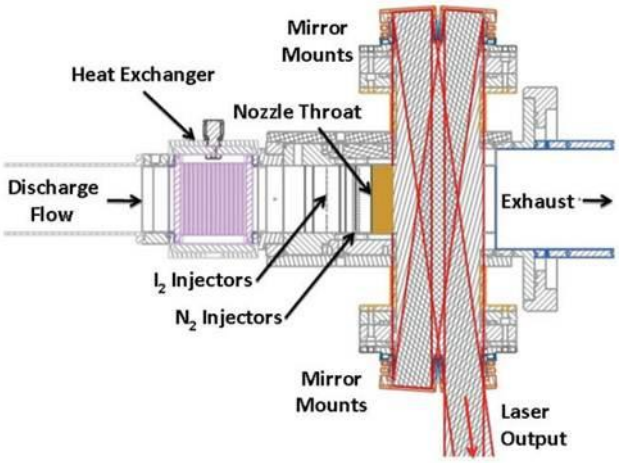

(b)

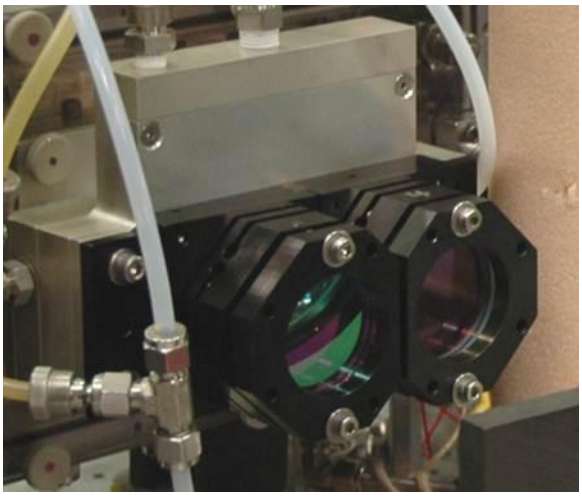

(c)

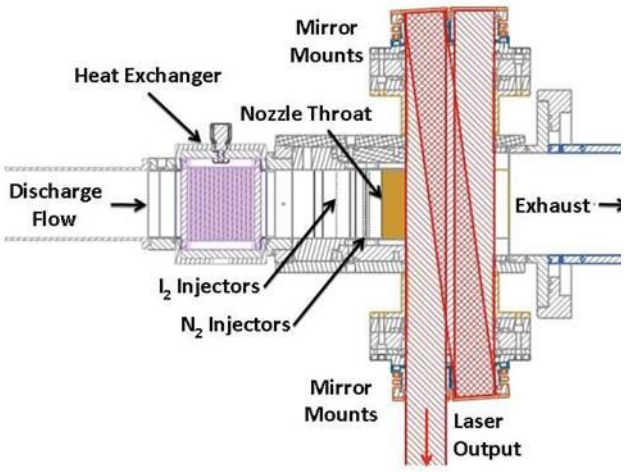

(d)

Figure 2.13. (a) Photograph showing two of the four mirrors used in the X-resonator. (b) Top view schematic of the X-resonator design. (c) Photograph showing two of the four mirrors in the Z-resonator design. (b) Top view schematic of the Z-resonator. Two mirrors are perpendicular to the flow direction and the other two are angled to complete the photon path through the gain region. In both X and Z-resonator combinations, the mirrors are 5 cm in diameter.

2.8 Diffuser Hardware

After the gas leaves the laser resonator, it heads further downstream to the diffuser. The purpose of the diffuser is to raise the gas pressure between the nozzle and the vacuum pumping system. At the downstream edge of the nozzle, typical pressures are around 2 Torr. The diffuser raises the gas pressure to around 12 Torr. The pressure rise is significant because the vacuum pumps only need to pump the system at 12 Torr instead of the 2 Torr at the nozzle exit. This is

important as pumping capacity is limited. Also, as the EOIL system has been increasing in size, the gas flow rates have increased. Gaining more pressure recovery in the diffuser has helped the EOIL system move to higher flow rates while utilizing existing pumping capacity. Figure 2.14 shows a photograph of the diffuser that was used with the Cav6 laser hardware. Fabricated from polycarbonate plates, the diffuser has a supersonic section which has a rectangular cross-section. The supersonic section also has three pressure ports to measure the pressure rise through the diffuser. Further downstream, a subsonic section has top and bottom pieces that diverge at three degree angles.

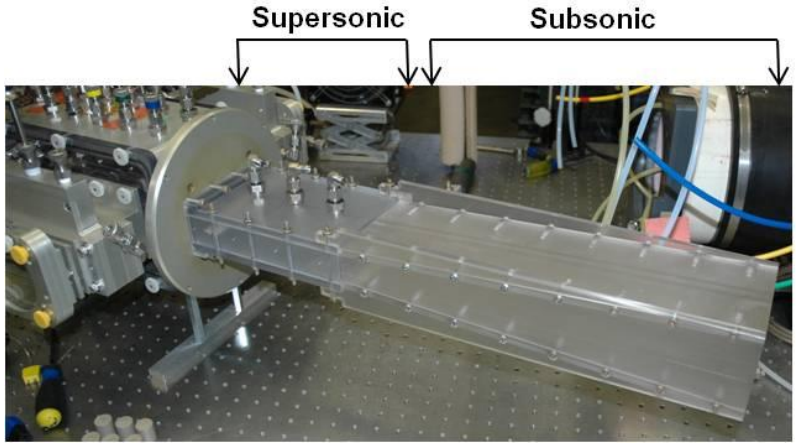

Figure 2.14. Photograph showing the supersonic and subsonic sections of the diffuser immediately downstream from the laser resonator. The supersonic section has a rectangular cross-section. Three pressure ports and located on the top of the supersonic section. The top and bottom pieces of the subsonic section diverge at three degree angles.

2.9 References

[2.1] Carroll, D.L., Verdeyen, J.T., King, D.M., Benavides, G.F., Woodard, B.S., Kittell, K., Solomon, W.C., Rawlins, W.T., Davis, S.J., and Kessler, W.J., Preliminary yield measurements in the ElectriCOIL system, *Proceedings of the Gas and Chemical Lasers and Applications IV Conference*, 26 January 2004, *SPIE* Vol. 5334, pp. 79-87 (2004).

[2.2] Piper, L.G., Caledonia, G.E., and Kennealy, J.P., Rate constants for deactivation of $N_2(A^3\Sigma_u^+, v'=0,1)$ by O, *J. Chem. Phys.* **75** 2847 (1981).

[2.3] Davis, S.J., Allen, M.G., Kessler, W.J., McManus, K.R., Miller, M.F., and Mulhall, P.A., Diode laser-based sensors for chemical oxygen iodine lasers, *Proc. SPIE* 2702, pp. 195-201 (1996).

[2.4] Zimmerman, J.W., *Studies of Oxygen-Helium Discharges for Use in Electric Oxygen-Iodine Laser*, University of Illinois PhD Thesis (2010).

[2.5] Woodard, B.S., Zimmerman, J.W., Benavides, G.F., Day, M.T., Palla, A.D., Carroll, D.L., Verdeyen, J.T., and Solomon, W.C., Investigation of the Production of $O_2(a^1\Delta)$ in Rectangular and Multi-Tube Radio-Frequency Discharges, *AIAA 41st Plasmadynamics and Lasers Conference*, 28 June - 1 July 2010, AIAA Paper 2010-5040.

[2.6] Zimmerman, J.W., Benavides, G.F., Woodard, B.S., Carroll, D.L., Palla, A.D., Verdeyen, J.T., and Solomon, W.C., Measurements of Improved ElectricOIL Performance, Gain, and Laser Power, *AIAA 40th Plasmadynamics and Lasers Conference*, 22-25 June 2009, AIAA Paper 2009-4059.

[2.7] King, D.M., *Experimental Optimization of a Nitrogen-Diluted Chemical Oxygen Iodine Laser*, University of Illinois Master's Thesis (2000).

3. Temperature Diagnostics for EOIL System

In this section, the importance of gas temperature in the EOIL system will be discussed. Due to the importance of temperature, the gas temperature must be measured at different locations throughout the EOIL system. Problems with traditional measurement techniques have led to molecular spectroscopy being relied upon for gas temperature measurements. In the past, all temperature information was calculated using the O_2(b) emission. This section discusses a new temperature diagnostic developed so that gas temperatures can be obtained from the O_2(a) emission spectrum.

3.1. Importance of Gas Temperature

Very early in the work with EOIL, it was known that temperature would be a driving factor in laser performance. The critical aspect of temperature control results from the equilibrium of the pumping reaction (Equation 1.2) where the desired state $I(^2P_{1/2})$ is produced from the forward reaction. However, this reaction is countered by the reverse reaction where $I(^2P_{1/2})$ is converted back into $I(^2P_{3/2})$. The forward k_f and reverse k_r reaction rates are temperature dependent and are provided in Table 3.1.

Table 3.1. Pumping Reaction Rates for EOIL [3.1]

Reaction	Rate [cm^3-s^{-1}]
k_f	7.8 (10^{-11})
k_r	1.04 (10^{-10})exp(-401/T)

The important thing to note from Table 3.1 is that the reverse rate is slower when the temperature is decreased. Lower temperatures favor the excitation process of $I(^2P_{3/2})$ to $I(^2P_{1/2})$, leading to increased laser performance. The equilibrium constant K_{eq} for these reactions is the ratio of the forward to reverse rates and is shown as Equation (3.1) [3.2]

$$K_{eq} = k_f / k_r = 0.75\exp(401/T) \tag{3.1}$$

where T is the temperature. When Equation (3.1) is in equilibrium, the following [Equation (3.2)] holds true

$$k_f[O_2(a^1\Delta)][I(^2P_{3/2})] = k_r[O_2(X^3\Sigma)][I(^2P_{1/2})] \quad (3.2)$$

which can be rearranged to give Equation (3.3).

$$\frac{[I(^2P_{1/2})]}{[I(^2P_{3/2})]} = K_{eq}\frac{[O_2(a^1\Delta)]}{[O_2(X^3\Sigma)]} \quad (3.3)$$

For population inversion to take place, the following [Equation (3.4)] must be true.

$$\frac{[I(^2P_{1/2})]}{[I(^2P_{3/2})]} > 0.5 \quad (3.4)$$

Combining Equations (3.3) and (3.4) results in Equation (3.5)

$$\frac{[O_2(a^1\Delta)]}{[O_2(X^3\Sigma)]} = \frac{1}{2K_{eq}} \quad (3.5)$$

which can be rearranged through the following steps to end with Equation (3.6).

$$\frac{[O_2(X^3\Sigma)]}{[O_2(a^1\Delta)]} = 2K_{eq}$$

$$\frac{[O_2(X^3\Sigma)]}{[O_2(a^1\Delta)]} + \frac{[O_2(a^1\Delta)]}{[O_2(a^1\Delta)]} = 2K_{eq} + 1$$

$$\frac{[O_2(X^3\Sigma)]+[O_2(a^1\Delta)]}{[O_2(a^1\Delta)]} = 2K_{eq} + 1$$

$$\frac{[O_2(a^1\Delta)]}{[O_2(a^1\Delta)]+[O_2(X^3\Sigma)]} = (2K_{eq} + 1)^{-1} \quad (3.6)$$

The term on the left side in Equation (3.6) is the minimum amount of $O_2(a)$ needed to produce positive gain (also known as the threshold yield). The threshold yield Y_{TH} is shown in Equation (3.7).

$$Y_{TH} = (2K_{eq} + 1)^{-1} \quad (3.7)$$

The equilibrium constant given in Equation (3.1) then can be inserted into Equation (3.7) to give the temperature-dependent equation for threshold yield [Equation (3.8)].

$$Y_{TH} = [1+1.5\exp(401/T)]^{-1} \quad (3.8)$$

Equation (3.8) is then plotted as Figure 3.1 to show the dependence of threshold yield on temperature.

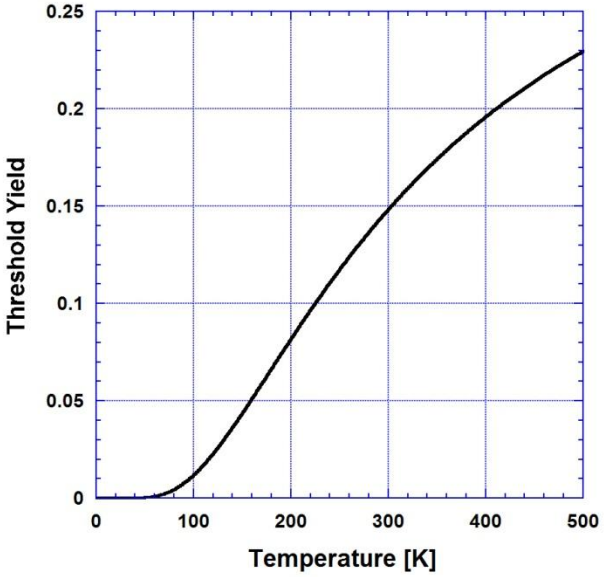

Figure 3.1. Threshold yield Y_{TH} of $O_2(a)$ needed for positive gain as a function of laser cavity temperature. The yield of $O_2(a)$ needed for positive gain decreases as the laser cavity temperature decreases. For this reason, a supersonic nozzle and cold gas injection are used to cool the gas before it enters the laser cavity.

As seen in Figure 3.1, the threshold yield of $O_2(a)$ needed for positive gain decreases as the laser cavity temperature is decreased. This characteristic of EOIL means that increased gain and laser power can be achieved at lower gas temperatures. Since lower temperatures are desired, a nozzle is used to expand the flow supersonically before it enters the laser cavity. Additionally, cold nitrogen gas is injected to further cool the flow.

3.2 Problems with Typical Gas Temperature Diagnostics

The gas temperature changes drastically as the flow progresses through the EOIL system. Typically, the gas exits the discharge at very high temperatures (500 K to 700 K) and is quickly cooled to low temperatures (100 K to 140 K) as it enters the laser cavity. A temperature diagnostic is important as it allows the temperature to be monitored at different stages in the laser system. In particular, temperature measurements are useful at the entrance and exit of the heat exchanger as they allow the heat exchanger performance to be quantified. Additionally, temperature measurements in the laser cavity allow the performance of the supersonic nozzle to

be monitored. The most common use of a temperature diagnostic occurs during discharge experiments, where temperature readings are used in the calculation of O_2(a) yield. Therefore, gas temperature measurements are made very often in the EOIL system.

Traditional temperature diagnostics cannot be used in the EOIL system for a number of reasons. Thermocouples are probably the most common method of measuring fluid temperature in the laboratory. However, there are many reasons why thermocouples cannot be used within the EOIL system. Thermocouples cannot be used near the discharge as there is a chance of arcing from the electrodes to the metal thermocouple. Additionally, thermocouples provide metal surfaces on which oxygen atoms can rapidly recombine. Oxygen atom recombination is an exothermic process [3.3], causing heat release on the surface of the thermocouple. The heat released from oxygen atom recombination on the thermocouple surface leads to elevated temperature readings that do not accurately represent the flow temperature.

Finally, the addition of thermocouples to a vacuum system is not easily accomplished without affecting the gas dynamics of the system. Thermocouples need to extend into the flow region in order to obtain accurate temperature readings. This would be very difficult to accomplish as temperature probe ports would need to be built into the hardware at various locations in the laser system. Also, the addition of a thermocouple in the nozzle would result in the formation of shocks, negatively affecting laser performance.

Since the common method of measuring gas temperature cannot be used in the EOIL system, molecular spectroscopy is used as a non-intrusive way for the flow temperature to be determined. Spectroscopic measurements can be taken through quartz tubing or through viewing ports in the system. By placing the spectroscopic tools outside the flow tubes, the gas dynamics are not affected. Also, the spectroscopic tools are fiber-coupled so that the measurement location can be changed relatively easily. The optical fibers can be moved so that measurements can be made at multiple locations in the laser system. This increased flexibility allows the optical fibers to be placed anywhere along the flow axis.

3.3 O_2(b) Temperature Diagnostic

Historically, the gas temperature in EOIL work has been determined from the O_2(b) emission spectrum. Assuming that the flow temperature is approximately equal to that of the O_2(b) molecules, the entire flow temperature can be determined. A sample experimental

emission spectrum from O_2(b) can be seen in Figure 3.2. The O_2(b) spectrum is centered at 762 nm and is composed of two emission branches, labeled R and P. The P-branch consists of emissions on the higher-wavelength side of 762 nm, while the R-branch consists of emissions on the lower-wavelength side.

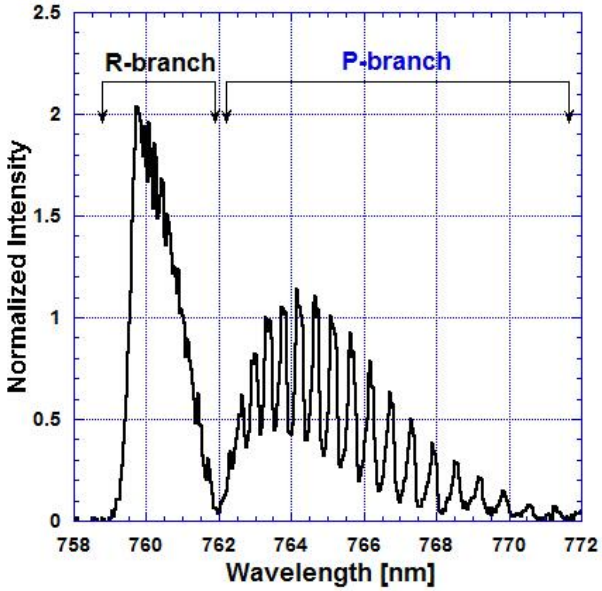

Figure 3.2. Experimental O_2(b) spectrum showing the normalized intensity versus the wavelength. The O_2(b) emission is comprised of the R and P branches. Temperature is calculated using the emission intensities of the P-branch.

O_2(b) measurements can be taken throughout the laser system and temperature information can be obtained by comparing the experimental spectra to temperature-dependent theoretical spectra. The line intensities are temperature dependent, so the emission profile of O_2(b) changes as a function of temperature. To illustrate this fact, Figure 3.3 is provided to show two experimental O_2(b) spectra at 420 K and 645 K, respectively. These measurements were taken at the discharge exit, and the temperature difference was obtained by varying the discharge power [1000 W for Figure 3.3(a) and 5000 W for Figure 3.3(b)]. As the O_2(b) temperature increases, the emission intensities on the lower-wavelength side of the R-branch increase, resulting in the sharper peak seen in Figure 3.3(b). The increasing temperature also causes emission intensities on the higher-wavelength side of the P-branch to increase in magnitude.

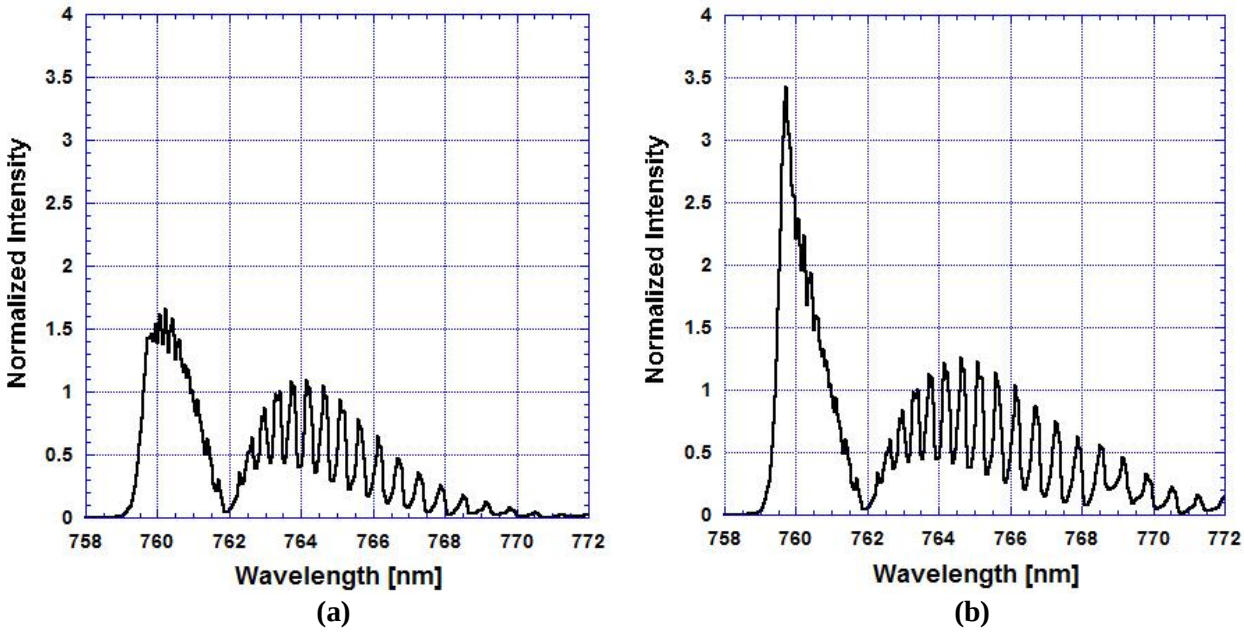

Figure 3.3. Experimental O_2(b) spectra at (a) 420 K and (b) 645 K. The spectra were taken immediately downstream from the discharge at discharge powers of (a) 1000 W and (b) 5000 W. The intensities are normalized to a peak around 763 nm.

The O_2(b) temperature diagnostic presently used in the laboratory was developed by Woodard [3.4]. Woodard used the work of Touzeau *et al.* [3.5] and Ritter and Wilkerson [3.6] to calculate the theoretical line intensities of the O_2(b) molecule based on rotational quantum number and temperature. The temperature is calculated from an experimental spectrum since the quantum numbers and the emission intensities are known.

From looking at Figures 3.2-3.3, it can be seen that the spectral resolution is better (individual emissions are more defined) along the P-branch. This differs from the R-branch, where the emission lines are so close to one another that the individual peaks are superimposed to form one large peak. The resolution obtained from experimental spectra is affected by the resolution of the spectrometer used during experimentation and other broadening effects. Due to the greater spectral resolution along the P-branch, the emission intensities of the P-branch are used to calculate temperature.

In its simplest form, the temperature diagnostic developed by Woodard uses the ratio of two peaks in the P-branch. By taking the ratio of two peaks, an expression was derived for temperature and is given as Equation (3.9)

$$kT = \frac{B\left[J_2\left(J_2+1\right) - J_1\left(J_1+1\right)\right]}{\ln\left[C_R \frac{I_1}{I_2}\left(\frac{2J_2+2.75}{2J_1+2.75}\right)\right]} \tag{3.9}$$

where kT is the temperature (in wavenumber), B = 1.391 cm^{-1} is the rotational constant for oxygen, I_x is the intensity of the emission with rotational quantum number J_x, and C_R is a constant which accounts for the spectral resolution and changes based on the quantum numbers used in the calculation. More specifically, the peaks with rotational quantum numbers J_1 = 6 and J_2 = 16 (C_R = 0.955) are used to calculate the temperature. When the known constants are inserted to Equation (3.9) the following [Equation (3.10)] is obtained.

$$kT = \frac{320}{\ln\left(2.25 C_R \frac{I_1}{I_2}\right)} \tag{3.10}$$

Therefore, the temperature can be found by inserting the peak intensity values associated with the J_1 = 6 and J_2 = 16 quantum numbers. A more detailed description of this temperature calculation can be found in Carroll *et al.* [3.7] and Woodard [3.4].

To implement Equation (3.10) in the data acquisition process, a Microsoft Excel macro was written which found the two peak intensity values from experimental spectra and output temperature. This allowed temperature information to be obtained from experimental O_2(b) spectra almost immediately after data was taken in the laboratory. While this method is fast and easy, the accuracy obtained from using such a simplified model is questionable. One source of inaccuracy stems from only using two peaks of the P-branch to calculate the temperature. This inaccuracy was mentioned by Woodard [3.4]. Other sources of inaccuracy will be discussed in another section.

Woodard went on to describe an improved method for determining the O_2(b) temperature. A computer program was written which developed a temperature-dependent spectrum to best match the experimental spectrum. To accomplish this, the temperature-dependent equation for line intensity was inserted into the program. Additionally, a lineshape function was applied to the theoretical intensities so that the experimental lineshape could be matched. The computer program varied the temperature until a theoretical spectrum best matched the experimental spectrum. The matching procedure used numerous peaks and valleys

of the P-branch to match theoretical spectra to the data. The improved accuracy stemmed from using many peaks and valleys [versus only using two peaks in Equation (3.10)] to calculate the temperature. More information about the computer code written by Woodard that determines the O_2(b) temperature can be found in [3.4].

3.4 Gain Temperature Diagnostic

While the O_2(b) emission is used to determine temperature in many parts of the laser system, there are locations where using the O_2(b) emission for temperature measurements is not desired. For instance, O_2(b) is not used to determine the gas temperature inside the laser cavity. Since O_2(b) has a relatively short lifetime due to deactivation, the concentration of the molecule is not very high by the time it reaches the laser cavity. Therefore, the emission signal is not strong, and the measured spectra are not useful for temperature measurements.

A better way of measuring the laser cavity temperature is using the iodine scan diagnostic [3.8]. The iodine scan diagnostic measures the gain signal, and temperature information can be extracted from the gain profile. The gain profile can be described by a Voigt function, which is a convolution of Doppler and Lorentzian profiles. Both the Doppler and Lorentzian linewidths cause the experimental gain lineshape to be broadened. The Lorentzian broadening occurs from collisional broadening effects (pressure) and broadening due to the iodine scan diagnostic's laser linewidth (approximately 8 MHz). The collisional broadening effect can be calculated from the gas pressure collisional broadening coefficients [3.9]. If one knows the gas flow rates and pressures inside the laser cavity, the Lorentzian broadening effects can be calculated.

Once the Lorentzian lineshape is known, Doppler broadening can be examined. The gas temperature causes variations to Doppler broadening. Therefore, determining the Doppler linewidth provides information about the gas temperature. To determine the Doppler linewidth, a nonlinear least-squares-fit procedure is used to fit the Voigt function to the experimental gain profile. The Doppler linewidth serves as a fitting parameter and is varied until a best fit to the data is found. Once the Doppler linewidth is found, temperature information can be determined from Equation (3.11)

$$T = \frac{mc^2}{8k \ln 2}\left(\frac{\Delta \nu_D}{\nu_0}\right)^2 \tag{3.11}$$

where T is the temperature, m is the molecular weight, c is the speed of light, k is the Boltzmann constant, Δv_D is the Doppler linewidth, and v_0 is the center frequency. A more detailed discussion on determining the temperature from the gain profile can be found in [3.8]-[3.10]. Figure 3.4 provides an example of how the temperature can be found from the gain signal. The experimental lineshape is shown and the temperature-dependent fit to the data has been made.

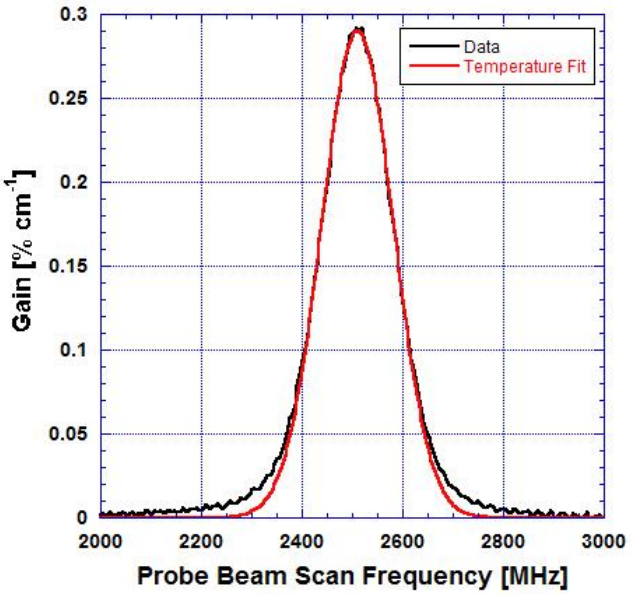

Figure 3.4. Experimental gain lineshape in the supersonic cavity as a function of probe beam scan frequency. A temperature of 122 K was found by fitting a Gaussian lineshape to the data.

3.5 O_2(a) Temperature Diagnostic

While the O_2(b) emission spectrum and iodine scan diagnostic are used to measure gas temperature, there are limitations on where each diagnostic can be used in the laser system. As previously mentioned, O_2(b) measurements are not useful for measuring temperature in the cavity and the iodine scan diagnostic is only useful in locations where iodine atoms are present (i.e. in the laser cavity). An additional temperature diagnostic was desired that could be placed anywhere in the EOIL system from the discharge exit to the laser cavity. Since the O_2(b) emission was already being used for temperature measurements, it was decided that the gas temperature could also be determined from the O_2(a) emission spectrum.

Using $O_2(a)$ emissions for temperature measurements is useful and convenient for a number of reasons. First, $O_2(a)$ measurements are already being made in the laser system as a way to measure $O_2(a)$ yield. Therefore, all the equipment needed to create another diagnostic was already in place. Also, $O_2(a)$ has a longer lifetime compared to $O_2(b)$. The long lifetime means that the $O_2(a)$ concentration is significant from the discharge exit all the way through the laser cavity. The fact that $O_2(a)$ is present (and abundant) throughout the entire laser system makes it a desirable candidate for a temperature diagnostic. The part of the laser system that benefits most from an $O_2(a)$ temperature diagnostic is the nozzle. Due to its long lifetime, the concentration of $O_2(a)$ in the cavity is still high enough for useful temperature measurements. This allows laser cavity temperature measurements to be made without having to flow the iodine needed for the ISD temperature diagnostic.

The $O_2(a)$ temperature diagnostic was developed using the previous work of Woodard [3.4] as a guide. However, there are some significant differences between the two methods. The following section details the development of the $O_2(a)$ temperature diagnostic.

3.6 Temperature-Dependent Theoretical Spectra from HITRAN

As with $O_2(b)$, determining the temperature from $O_2(a)$ is accomplished by matching the experimental spectrum to a temperature-dependent, theoretical spectrum. The theoretical spectrum is formulated using the **hi**gh-resolution **tran**smission (HITRAN) molecular database [3.11]. HITRAN provides the locations of the spectral line transitions and the linestrength absorption intensities. Since measurements made in the UIUC laboratory are emission spectra, the emission intensities can be calculated from the given HITRAN absorption intensities. The process of converting from absorption to emission intensities will be described in more detail later in this section.

For the $O_2(a)$ molecule, there are transitions from the O, P, Q, R, and S branches, which overlap to form the overall $O_2(a)$ spectrum. The spectral line transition locations, normalized emission intensities at 296 K, and corresponding transition branches for the $O_2(a)$ molecule are shown in Figure 3.5(a). A sample experimental emission spectrum for the $O_2(a)$ molecule can be seen in Figure 3.5(b). As seen in Figure 3.5(b), the individual branches cannot be distinguished in the $O_2(a)$ emission spectrum. This is very different compared to the $O_2(b)$ emission, where the P and R branches can easily be distinguished.

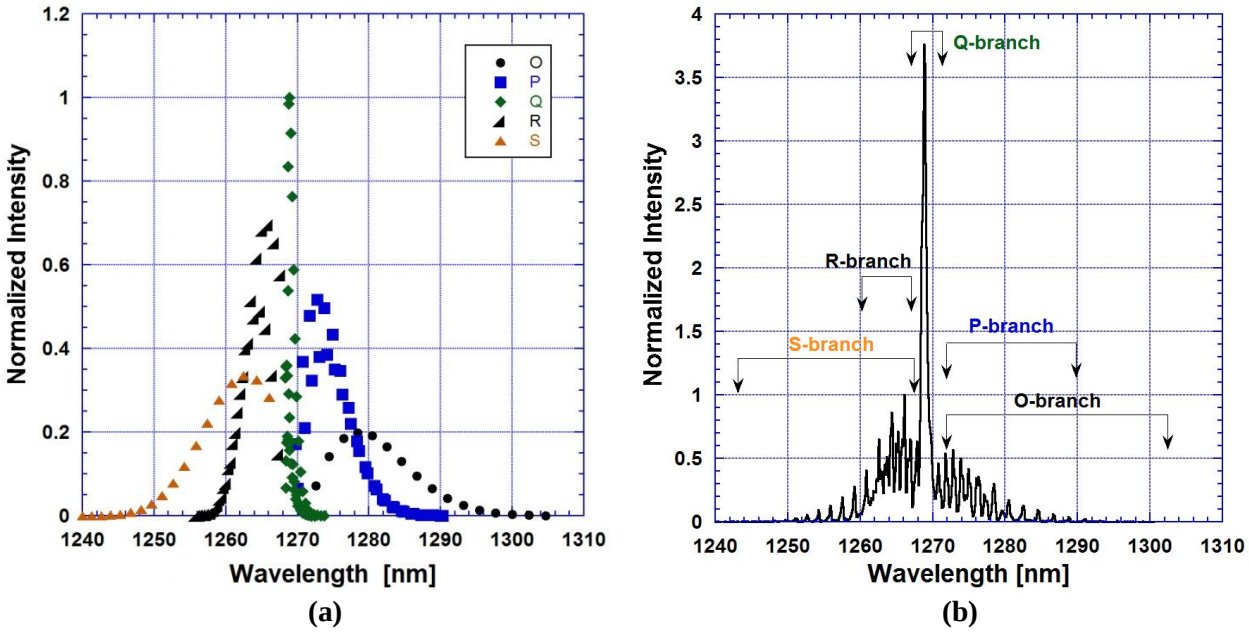

Figure 3.5. (a) Theoretical O_2(a) emission intensities versus the wavelength for the O through S branches calculated from HITRAN at 296 K. The intensities are normalized to the peak intensity value. (b) Experimental O_2(a) spectrum showing the normalized intensity versus wavelength.

The HITRAN database provides absorption intensities at a reference temperature of 296 K. Therefore, an equation is needed to calculate intensity values at different temperatures. The temperature correction of line intensity is given by Rothman *et al.* [3.12] and is provided as Equation (3.12).

$$S_{12} = S_{12}(T_{REF})\frac{Q(T_{REF})}{Q(T)}\frac{\exp(-c_2E_1/T)}{\exp(-c_2E_1/T_{REF})}\frac{[1-\exp(-c_2\nu_{12}/T)]}{[1-\exp(-c_2\nu_{12}/T_{REF})]} \tag{3.12}$$

In Equation (3.12), S_{12} is the spectral line intensity, T is the temperature, $Q(T)$ is the total internal partition function, E_1 is the lower state energy of the transition, ν_{12} is the spectral line transition frequency, and c_2 is the second radiation constant. The second radiation constant is defined in Equation (3.13)

$$c_2 = hc/k \tag{3.13}$$

where h is Planck's constant.

Next, groups of terms in Equation (3.12) are simplified. The total internal partition functions are given in Equations (3.14) and (3.15)

$$Q(T) = \sum_{\eta} g_{\eta} \exp(-c_2 E_{\eta} / T) \tag{3.14}$$

$$Q(T_{REF}) = \sum_{\eta} g_{\eta} \exp(-c_2 E_{\eta} / T_{REF}) \tag{3.15}$$

where g_η and E_η are the statistical weight and energy of the lower state, respectively. The values are summed over the entire lower state. Gamache *et al.* [3.13] provide a detailed analysis of the total internal partition function and also give a method for approximating Q as a function of temperature. The approximation for $Q(T)$ is given as Equation (3.16)

$$Q(T) = a + bT + cT^2 + dT^3 \tag{3.16}$$

where a, b, c, and d are coefficients in a third-degree polynomial fit to the values calculated using Equation (3.14). The coefficients for Equation (3.16) for the oxygen molecule are given in Table 3.2.

Table 3.2. Coefficients in Polynomial Fit for Internal Partition Sum of O_2 [3.13]

Temperature Range [K]	a	b	c	d
$70 \leq T \leq 500$	0.35923	0.73534	-0.64870 (10^{-4})	0.13073 (10^{-6})
$500 < T \leq 1500$	0.36539 (10^{2})	0.57015	0.16332 (10^{-3})	0.45568 (10^{-7})

Equation (3.16) can be applied to form Equation (3.17).

$$\frac{Q(T_{REF})}{Q(T)} = \frac{a + bT_{REF} + cT_{REF}^2 + dT_{REF}^3}{a + bT + cT^2 + dT^3} \tag{3.17}$$

The ratio of internal partition sums for the reference temperature and temperature can be approximated by Equation (3.18).

$$\frac{Q(T_{REF})}{Q(T)} \approx \frac{T_{REF}}{T} \tag{3.18}$$

The approximation given by Equation (3.18) can be verified graphically by comparing plots of Equations (3.17) and (3.18) as a function of temperature. These plots are shown in

Figure 3.6. Figure 3.6(a) shows that Equation (3.18) is a valid approximation over the entire range of 70 K to 500 K as the two lines barely deviate. In Figure 3.6(b), Equation (3.18) approximates (3.17) very well from temperatures of 500 K to 700 K. After 700 K, the lines deviate by a small margin. However, based on previous experimentation, flow temperatures are not expected to exceed values of 750 K so this method should still be extremely accurate.

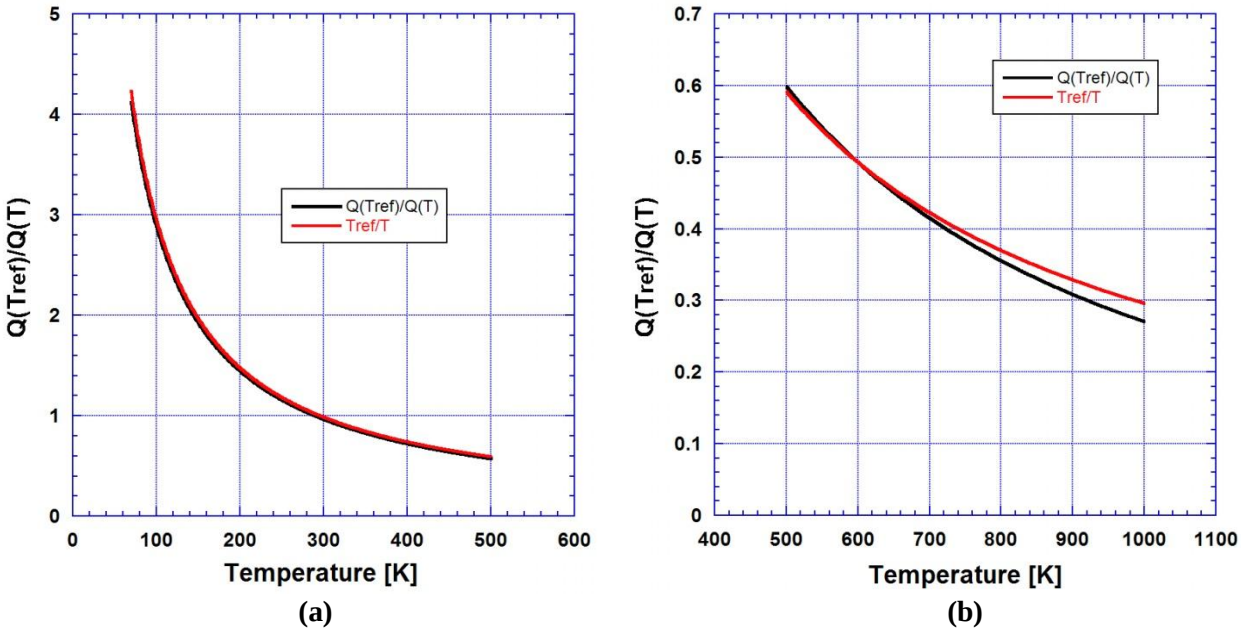

Figure 3.6. Ratio of total internal partition sums of the reference temperature to the temperature between (a) 70 K and 500 K and (b) 501 K and 1000 K. These plots show that Equation (3.18) is a valid approximation up to 750 K.

The following term from Equation (3.12) is also simplified algebraically.

$$\frac{\exp(-c_2 E_1 / T)}{\exp(-c_2 E_1 / T_{REF})} = \exp[c_2 E_1 (1/T_{REF} - 1/T)] \tag{3.19}$$

For large wavenumbers, which is true for O_2(a), the following expression is valid.

$$\frac{[1-\exp(-c_2 \nu_{12} / T)]}{[1-\exp(-c_2 \nu_{12} / T_{REF})]} \approx 1 \tag{3.20}$$

The following expression is obtained by substituting Equations (3.18) through (3.20) into Equation (3.12).

$$S_{12} = S_{12}(T_{REF})\frac{T_{REF}}{T}\exp[c_2 E_1(1/T_{REF} - 1/T)] \tag{3.21}$$

Equation (3.21) calculates the absorption line intensities at different temperatures. However, the data taken during experiments are emission spectra. Therefore, the absorption line intensities need to be converted to emission intensities. This involves relating the Einstein coefficient for induced absorption B_{12} to the Einstein coefficient for spontaneous emission A_{21}. Equation (3.22) relates B_{12} to A_{21} [3.11]

$$A_{21} = 8\pi h\nu_{12}^3 B_{12}\frac{g_1}{g_2} \tag{3.22}$$

where g_1 and g_2 are the lower and upper statistical weights, respectively. The Einstein coefficient for induced absorption is related to the absorption intensity by Equation (3.23) [3.11]

$$B_{12} = S_{12}\frac{c}{h\nu_{12}}\frac{N}{n_1} \tag{3.23}$$

where n_1 is the number density of the lower state and N is the total molecular number density. The ratio of total to lower state number densities is given by Equation (3.24) [3.11].

$$\frac{N}{n_1} = \frac{Q(T)}{g_1\exp(-c_2 E_1/T)} \tag{3.24}$$

Equations (3.21), (3.23), and (3.24) are substituted into (3.22) to get the following.

$$A_{21} = 8\pi c\nu_{12}^2 S_{12}(T_{REF})\frac{T_{REF}}{T}\frac{Q(T)}{g_2}\exp(c_2 E_1/T_{REF}) \tag{3.25}$$

The emission intensity S_{21} is given by the following expression

$$S_{21} = \frac{n_2}{N}A_{21} \tag{3.26}$$

where n_2 is the number density of the upper state. The ratio of upper state to total number densities is given by Equation (3.27)

$$\frac{n_2}{N} = \frac{g_2 \exp(-c_2 E_2 / T)}{Q(T)} \tag{3.27}$$

where E_2 is the energy of the upper state. The energy of the upper state is found by summing the lower state energy E_1 and the energy of the transition v_{12}. Substituting Equations (3.25) and (3.27) into (3.26) results in Equation (3.28).

$$S_{21} = 8\pi c \nu_{12}^2 S_{12}(T_{REF}) \frac{T_{REF}}{T} \exp(-c_2 E_2 / T) \exp(c_2 E_1 / T_{REF}) \tag{3.28}$$

Equation (3.28) is the final expression for the emission intensity of each line as a function of temperature. The effect on the intensities after converting from absorption to emission can be seen in Figure 3.7. In Figure 3.7, the normalized absorption and emission intensities for O_2(a) at the reference temperature of 296 K are plotted. The effect of converting from absorption to emission intensity is best illustrated by looking at the intensity values on the low and high-wavelength sides of the spectra. On the low-wavelength side (S branch), the intensity values for emission are lower compared to the absorption. The opposite is true on the high-wavelength side (O branch), where the intensity values for emission are higher than the absorption values. It is important to note that the individual branches (O through S) are not labeled in Figure 3.7. The distinctions between the individual branches can be seen in Figure 3.5.

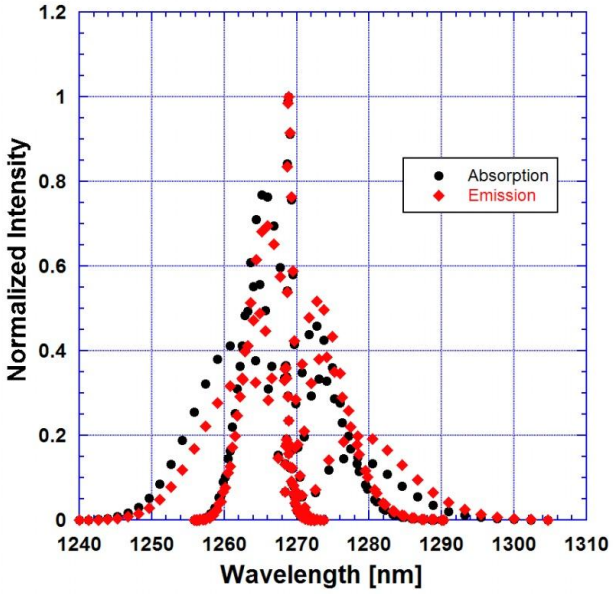

Figure 3.7. The absorption and emission intensities for O_2(a) at the reference temperature of 296 K. The intensity values are normalized to the peak intensity. It is important to note that the five branches (O through S) have not been individually labeled. The individual branch labels can be seen in Figure 3.5.

Next, a temperature-dependent O_2(a) spectral model is created from the HITRAN data. The absorption line strength intensities at the reference temperature of 296 K are input to a Mathematica program. The program uses Equation (3.28) to convert absorption intensities to emission intensities and calculates the intensity as a function of temperature. Equation (3.28) becomes a function to temperature T and the location of the line centers λ_0. The modified emission intensity equation is shown as Equation (3.29).

$$S_{21}(T,\lambda_0) = 8\pi c\nu_{12}^2(\lambda_0)S_{12}(T_{REF},\lambda_0)\frac{T_{REF}}{T}\exp[-c_2E_2(\lambda_0)/T]\exp[c_2E_1(\lambda_0)/T_{REF}] \qquad (3.29)$$

In addition to the line strength absorption intensities at the reference temperature $S_{12}(T_{REF},\lambda_0)$, the following parameters are input from HITRAN: the spectral line transition frequency $\nu_{12}(\lambda_0)$, the lower state energy of the transition $E_1(\lambda_0)$, and the upper state energy of the transition $E_2(\lambda_0)$. The values for $\nu_{12}(\lambda_0)$ and $E_1(\lambda_0)$ are provided directly from HITRAN. As previously stated, the value for $E_2(\lambda_0)$ is obtained by summing the values of $\nu_{12}(\lambda_0)$ and $E_1(\lambda_0)$.

After the line intensities have been calculated, a lineshape function must be used to transform the infinitesimally thin emission line into a distribution of emitted photons. A third-order, or super-Lorentzian, lineshape was used to fit the experimental data. The super-Lorentzian is given as Equation (3.30).

$$g(\lambda,\Delta\lambda,\lambda_0) = \frac{(\Delta\lambda/2)^2}{\left[|\lambda-\lambda_0|^3 + (\Delta\lambda/2)^3\right]} \qquad (3.30)$$

where λ is the wavelength and $\Delta\lambda$ is the resolution. The program then outputs emission intensity as a function of wavelength, temperature, and resolution. The intensity equation sums the contributions from the individual lineshapes to get the overall spectrum as seen during experimentation. The intensity I is given as Equation (3.31).

$$I(\lambda,T,\Delta\lambda) = \sum_{\lambda_0} S_{21}(T,\lambda_0)g(\lambda,\Delta\lambda,\lambda_0) \qquad (3.31)$$

3.7 Matching the Experimental and Theoretical Spectra

The process of matching temperature-dependent theoretical spectra to experimental spectra is looked at next. The computer code reads the data and finds intensity values of

numerous peaks and valleys of the experimental spectra. It then attempts to match peak and valley values from the data with the theoretical spectra. The code runs through different theoretical O_2(a) spectra by varying the temperature and resolution until the best fit to the data is found. Increasing or decreasing the flow temperature leads to increasing/decreasing peak values at certain wavelengths. The resolution also has an effect on the peak and valley heights, as a high resolution leads to more distinct peaks.

A variety of peaks and valleys from approximately 1255 nm to 1270 nm were used to match the experimental to a theoretical spectrum. An example of an experimental O_2(a) spectrum is shown a Figure 3.8(a). A "zoomed-in" version of this plot is shown as Figure 3.8(b), which has labels for the peaks (P) and valleys (V) used in the matching process. The maximum intensity of these peaks changes as the flow temperature changes. Therefore, a comparison of the relative intensity between peaks and valleys allows the computer code to match theoretical spectra and temperatures to the data. A more detailed discussion of the matching procedures is discussed next.

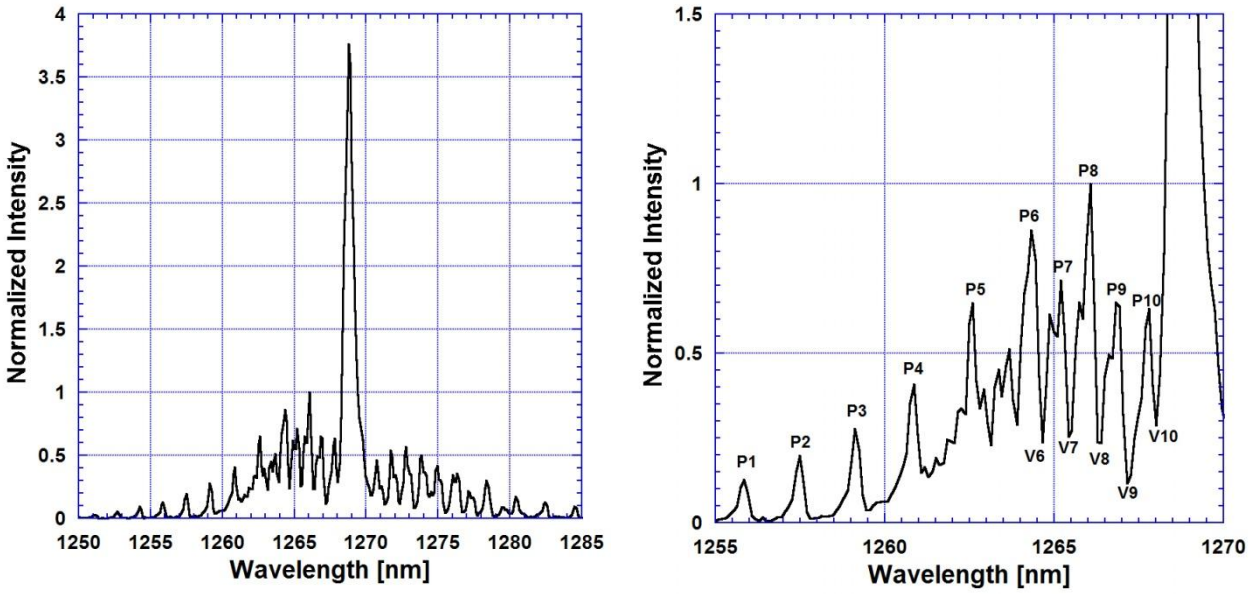

Figure 3.8. (a) Experimental O_2(a) spectrum showing the normalized intensity versus the wavelength. (b) Enhanced version of (a) showing peaks 1 through 10 and valleys 6 through 10 used to match the experimental and theoretical spectra.

The matching is accomplished by minimizing the sums of the square of the difference between peak and valley values from the data and the program. In order to compare the theoretical output with the data, the intensity values needed to be normalized in each case. Before matching occurs, the theoretical and experimental spectra intensity values are normalized to eighth peak (P8) to ensure that comparisons between theoretical and experimental peaks can be made. The eighth peak was chosen as the normalizing peak since it usually had the highest intensity. The function that is minimized $f(T,\Delta\lambda)$ is given as Equation (3.32)

$$f(T,\Delta\lambda)=\sum_{i=1}^{N}\left[P(i)_T(T,\Delta\lambda)-P(i)_E\right]^2+\sum_{i=1}^{J}\left[V(i)_T(T,\Delta\lambda)-V(i)_E\right]^2 \qquad (3.32)$$

where $P(i)$ is the peak intensity value of the i-th peak, $V(i)$ is the minimum intensity value of the i-th valley, and the subscripts T and E refer to the theoretical and experimental spectra, respectively. The theoretical peak and valley intensities are functions of the temperature and resolution and are varied by the code until a minimized solution is reached.

An alternative method for matching the spectra is to compare the ratio of peak to peak and peak to valley intensity values. The function that is minimized in this case is shown in Equation (3.33).

$$f(T,\Delta\lambda)=\sum_{i=1}^{N}\left[\frac{P(i)_T(T,\Delta\lambda)}{P(REF)_T(T,\Delta\lambda)}-\frac{P(i)_E}{P(REF)_E}\right]^2+\sum_{i=1}^{J}\left[\frac{P(i)_T(T,\Delta\lambda)}{V(i)_T(T,\Delta\lambda)}-\frac{P(i)_E}{V(i)_E}\right]^2 \qquad (3.33)$$

where $P(REF)$ is a reference peak that is chosen to normalize the theoretical and experimental results.

3.8 O_2(b) Temperature Diagnostic from HITRAN Data

Since the HITRAN database contains information about the O_2(b) molecule, the process described above also was completed with O_2(b). This would allow temperature comparisons to be made between O_2(a) and O_2(b) using the same HITRAN data. Having an additional O_2(b) temperature diagnostic would also allow comparisons to be made between the O_2(b) method using HITRAN and the current O_2(b) temperature method.

The spectral line transition locations and calculated emission intensities for the O_2(b) molecule were found using the HITRAN database as described above. Figure 3.9(a) shows the

normalized emission intensities as a function of wavelength. An experimental spectrum is also shown in Figure 3.9(b) to compare with the theoretical line intensities.

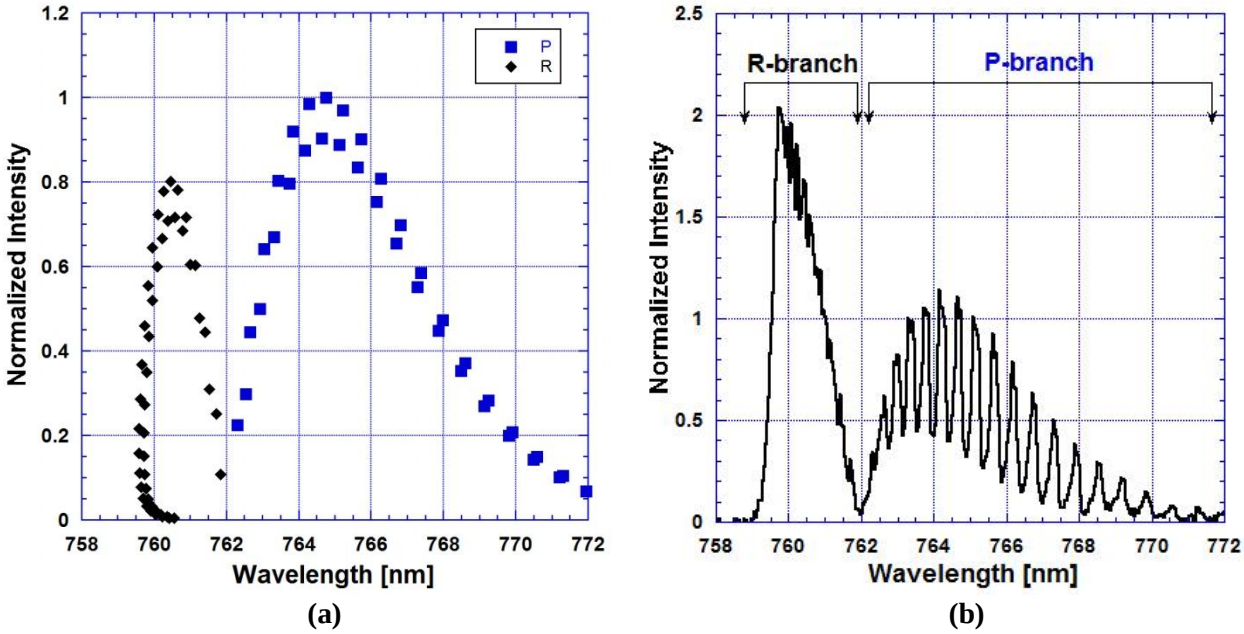

Figure 3.9. (a) O_2(b) normalized emission intensities versus wavelength for the P and R branches calculated from HITRAN at 296 K. The intensity values are normalized to the peak intensity value. (b) Experimental O_2(b) spectrum with R and P branches labeled showing the normalized intensities versus the wavelength.

As with O_2(a), the HITRAN data for O_2(b) needed to be converted from absorption to emission. The absorption intensities were calculated using the same process described above for the O_2(a) molecule. Figure 3.10(a) shows the absorption intensities and the calculated emission intensities. Again, the P and R branches have not been individually labeled in Figure 3.10(a). The individual distinctions between the branches can be seen in Figure 3.9(a).

The matching procedure was carried out in a similar fashion to the O_2(a) molecule. A variety of peaks and valleys from approximately 763 nm to 767 nm were used to match experimental spectra to theoretical spectra. A "zoomed-in" version of Figure 3.9(b) is shown as Figure 3.10(a), which has labels for the peaks (P) and valleys (V) used in the matching process. Since the maximum intensity of these peaks changed as the flow temperature changed, a comparison of the relative intensity between peaks and valleys allows the computer code to match theoretical spectra and temperatures to the data.

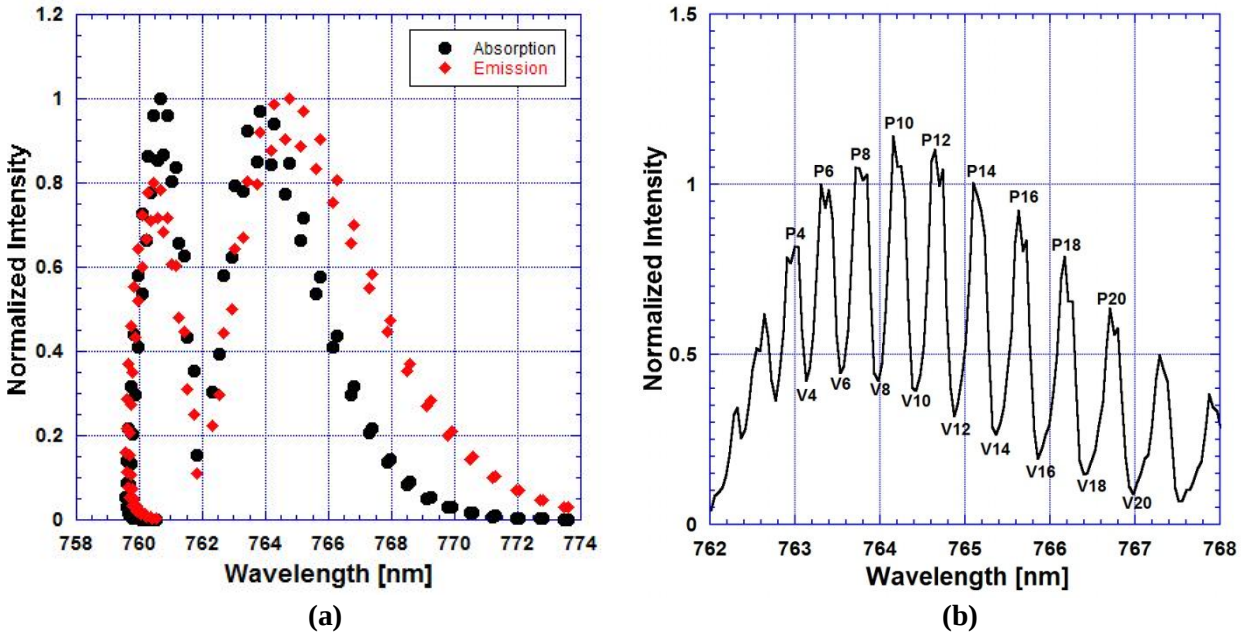

Figure 3.10. (a) Absorption and emission intensities for O_2(b) at the reference temperature of 296 K. The intensity values are normalized to the peak intensity. It is important to note that the two branches (P and R) have not been individually labeled. (b) Enhanced Figure 3.9(b) showing peaks 4 through 20 and valleys 4 through 20 used to match the experimental and theoretical spectra.

3.9 Summary of Gas Temperature Diagnostics

This section explained the four temperature diagnostics used in the EOIL system. A summary of the first two methods [O_2(b) and gain temperature determination] was provided in the text above. The development of the last two methods was the subject of this section. In subsequent sections, experimental data will be analyzed using these temperature methods and comparisons among the four methods will be made. To help the reader avoid confusion, Table 3.3 gives a brief description of each method and the shorthand names that will be used in the remainder of this thesis.

Table 3.3. Summary of Temperature Diagnostics and Shorthand Name

Molecule	Description	Shorthand Name
O_2(b)	Developed by Woodard [3.4] using Equation (3.10) and implemented using an Excel Macro	O_2(b)_Macro
O_2(b)	Developed by Woodard [3.4] using computer program to match theoretical spectra to experimental spectra	O_2(b)_BSW
I*	Uses method described by Davis *et al.* [3.10] to determine temperature from Doppler linewidth of gain profile	Gain Diagnostic
O_2(a)	Developed in this thesis using HITRAN data for O_2(a). Uses computer program to match theoretical spectra to experimental spectra	O_2(a)_MTD
O_2(b)	Developed in this thesis using HITRAN data for O_2(b). Uses computer program to match theoretical spectra to experimental spectra	O_2(b)_MTD

3.10 References

[3.1] Perram, G.P. and Hager, G.D., The Standard COIL Kinetics Package, A*ir Force Weapons Laboratory, Kirtland Air Force Base, Final Report*, AFWL-TR-88-50 (1988).

[3.2] Hon, J., Hager, G., Helms, C., and Truesdell, K., *AIAA Journal*, Vol. 34, No. 8, pp. 1595-1603 (1996).

[3.3] Melin, G.A. and Madix, R.J., Energy accommodation during oxygen atom recombination on metal surfaces, *Transactions of the Faraday Society*, Vol. 67, pp. 198-211 (1971).

[3.4] Woodard, B.S., Trials and Tribulations Along the Path to Positive Gain in an Electrically Assisted Oxygen-Iodine Laser System, *University of Illinois at Urbana-Champaign Master's Thesis* (2004).

[3.5] Touzeau, M., Vialle, M., Zellagui, A., Gousset, G., Lefebvre, M., and Pealat, M., Spectroscopic temperature measurements in oxygen discharges, *J. Phys. D: Appl. Phys.* 24 pp. 41-47 (1991).

[3.6] Ritter, K.J. and Wilkerson, T.D., High-Resolution Spectroscopy of the Oxygen A Band, *J. Mol. Spectrosc.* 121 pp. 1-19 (1987).

[3.7] Carroll, D.L., Verdeyen, J.T., King, D.M., Woodard, B.S., Zimmerman, J.W., Skorski, L.W., and Solomon, W.C., Recent Experimental Measurements of the ElectriCOIL System, AIAA Paper 2003-4029 (2003).

[3.8] Davis, S.J., Kessler, W.J., and Keating, P.K., Progress in the Development of Sensors for COIL Devices, *SPIE Gas Phase and Chemical Lasers and Intense Beam Interactions*, Proc. SPIE 3931, Paper 24, pp. 156-161 (2000).

[3.9] Furman, D., Bruins, E., Rybalkin, V., Barmashenki, B.D., and Rosenwaks, S., Parametric Study of Small-Signal Gain in a Slit Nozzle, Supersonic Chemical Oxygen-Iodine Laser

Operating without Primary Buffer Gas, *IEEE J. Quantum Electron.*, Vol. 37, No. 2 (2001).

[3.10] Davis, S.J., Allen, M.G., Kessler, W.J., McManus, K.R., Miller, M.F., and Mulhall, P.A., Diode laser-based sensors for chemical oxygen iodine lasers, *Proc. SPIE* 2702, pp. 195-201 (1996).

[3.11] Rothman, L.S., Gordon, I.E., Barbe, A., Benner, D.C., Bernath, P.F., *et al.*, The HITRAN 2008 molecular spectroscopic database, *J. of Quant. Spectros. & Radiat. Transfer*, Vol. 110, pp. 533-572 (2009).

[3.12] Rothman, L.S., Rinsland, C.P., Goldman, A., Massie, S.T., Edwards, D.P., *et al.*, The HITRAN molecular spectroscopic database and HAWKS (HITRAN Atmospheric Workstation): 1996 Edition, *J. of Quant. Spectros. & Radiat. Transfer*, Vol. 60, No. 5, pp. 665-710 (1998).

[3.13] Gamache, R.R., Kennedy, S., Hawkins, R., Rothman, L.S., Total internal partition sums for molecules in the terrestrial atmosphere, *J. Molecular Structure*, 517-518, pp. 407-425 (2000).

4. Experimental Results

The previous section described different methods for calculating temperature in the EOIL system. In this section, the processes of determining temperature from $O_2(a)$ and $O_2(b)$ will be further discussed. In particular, this section will look at some problems encountered while trying to calculate temperature from $O_2(a)$ and $O_2(b)$. Additionally, numerous experiments will be presented where the $O_2(a)$ and $O_2(b)$ temperature diagnostics were used to analyze data. This includes a preliminary use of the $O_2(a)$ temperature diagnostic in the VertiCOIL system. Also, the temperature diagnostics will be used to calculate gas temperatures versus discharge operating time at constant power. In addition, the temperature diagnostic tools will be used to investigate gas temperatures at the discharge exit and within the laser cavity. Finally, the performance of two heat exchanger designs will be examined using the $O_2(a)$ and $O_2(b)$ temperature diagnostics.

4.1 Problems with $O_2(a)$ and $O_2(b)$ Spectra in EOIL

Calculating temperature from $O_2(a)$ and $O_2(b)$ emission spectra consists of matching experimental spectra to temperature-dependent theoretical spectra. However, the spectral measurements taken in the laboratory are not always ideal for matching procedures. Since other factors inherent to the EOIL system affect the experimental spectra, preprocessing must occur before attempting to match the data to theoretical spectra.

One of the main problems associated with experimental $O_2(a)$ and $O_2(b)$ emission spectra in the EOIL system involves the NO_2* emission. As mentioned in Section 1, NO_2* is produced from the reaction of NO with O atoms. This reaction is favorable from a laser power standpoint as the addition of NO controls the O atom quenching of I*. However, the broadband emission of NO_2* affects the spectroscopic measurement tools needed to determine $O_2(a)$ yield and gas temperature. The NO_2* emission, also known as "air afterglow," can be seen in the flow tubes as a yellow-green glow. Since the NO_2* emission is so broad, the spectrum interferes with both the $O_2(a)$ and $O_2(b)$ measurements [4.1]. Figure 4.1 shows the effect of the NO_2* emission on the $O_2(a)$ and $O_2(b)$ experimental spectra. In Figure 4.1, measured spectra are shown with and without NO. Other than adding NO, the gas flow conditions and discharge power were the same for both the red and blue spectra. The NO_2* emission causes the measurements to have a ramped baseline that elevates and rotates the spectra.

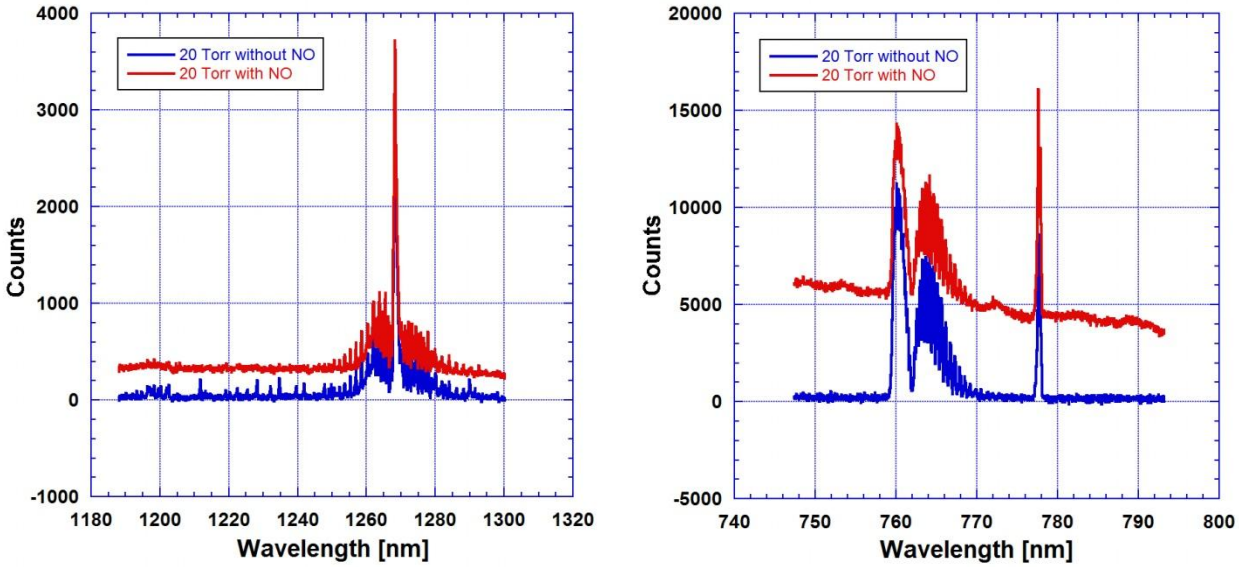

Figure 4.1. (a) O_2(a) and (b) O_2(b) scans showing the effect of NO on the spectra. The spectra taken without NO (blue) do not have the "air afterglow" and the tails of the spectra have a baseline near zero. The spectra with NO (red) have a ramped baseline which must be corrected before O_2(a) yield and temperatures can be obtained from the spectra. The flow conditions were O_2:He:NO 10:33:0 and 10:33:0.18 mmol-s^{-1} and the discharge power was 600 W for both cases.

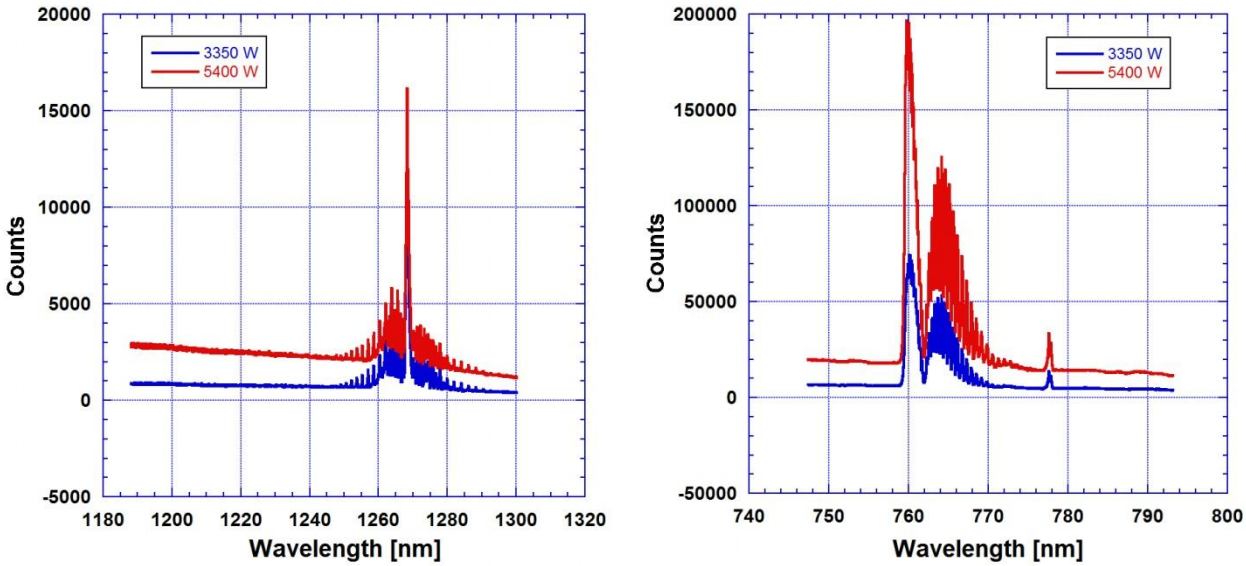

Figure 4.2. Experimental O_2(a) and O_2(b) spectra showing the effect of discharge power on the ramped baseline. (a) O_2(a) spectra at 3350 W and 5400 W input power. Both spectra were at 40 Torr and had flow rates of O_2:He:NO 45:150:1.0 mmol-s^{-1}. (b) O_2(b) spectra at 3350 W and 5400 W input power. Both spectra were at 50 Torr and had flow rates of O_2:He:NO 45:150:0.26 mmol-s^{-1}. Increasing the discharge power increases the O_2(a) and O_2(b) signals but also increases ramped baseline from the NO_2* emission.

The strength of the "air afterglow" effect is dependent on discharge power and pressure. It is strongest at high discharge powers as the NO_2* signal grows proportionally to input power. Figure 4.2 shows the effect of discharge power on the NO_2* signal. In Figure 4.2, the pressure and gas flow rates were constant and the discharge power was changed from 3350 W to 5400 W. Increasing the discharge power increases the O_2(a) and O_2(b) signals but also increases ramped baseline from the NO_2* emission.

The "air afterglow" effect is also strongest at low pressures. The O_2(a) and O_2(b) signals are weaker at lower pressures due to the lower densities in the optical diagnostics duct. Since the O_2(a) and O_2(b) signals are weaker, the NO_2* signal has a greater effect on the measured signals. Figures 4.3 and 4.4 show the effects of pressure on the NO_2* emission. In Figures 4.3 and 4.4, the gas flow rates and discharge power were constant and the pressure was changed from 50 Torr to 80 Torr. Experimental spectra are shown with and without the addition of NO. Both O_2(a) and O_2(b) spectra at the higher pressure have a decreased baseline from the NO_2* emission.

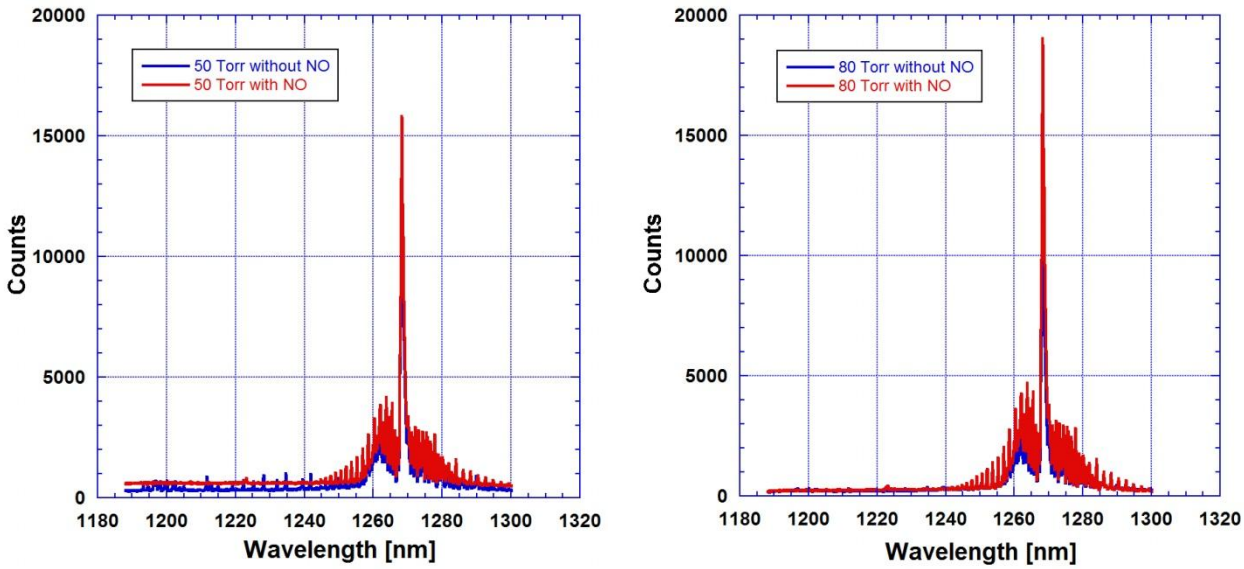

Figure 4.3. O_2(a) spectra showing the effect of pressure and NO flow rate on the ramped baseline. O_2(a) spectra at (a) 50 Torr and (b) 80 Torr with NO (red) and without NO (blue). The effect of NO on the spectra is much greater at lower pressures. Flow rates were O_2:He:NO 45:150:0 and 45:150:1.4 mmol-s^{-1} and the discharge power was constant at 4500 W.

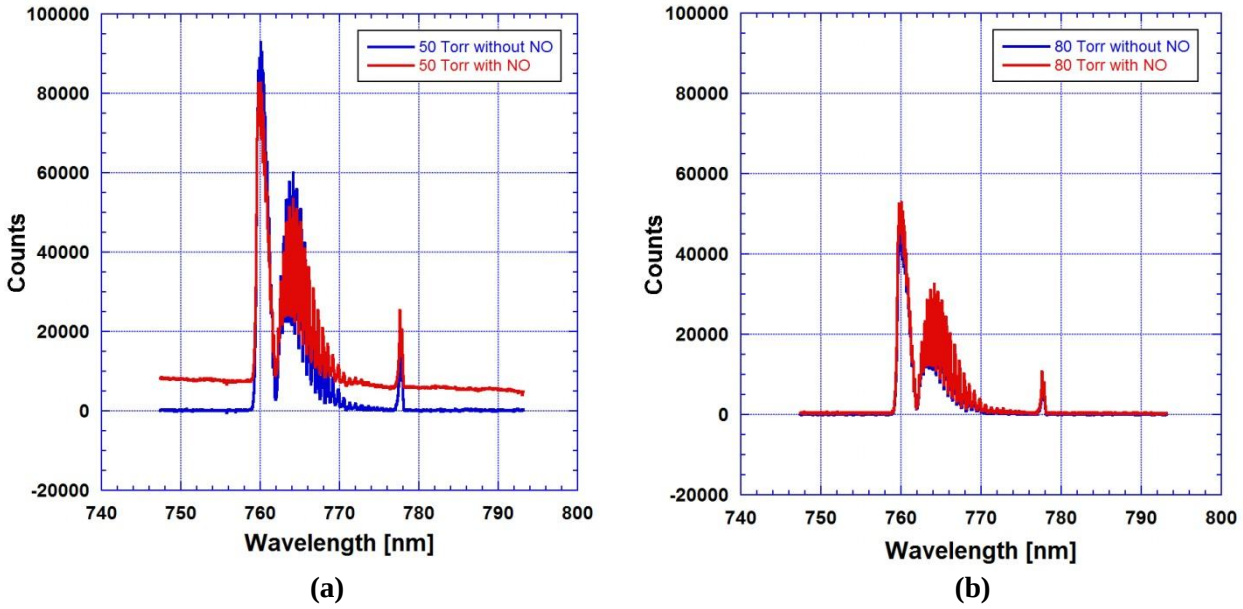

Figure 4.4. O_2(b) spectra showing the effect of pressure and NO flow rate on the ramped baseline. O_2(b) spectra at (a) 50 Torr and (b) 80 Torr with and without NO. The effect of NO on the spectra is much greater at lower pressures. Flow rates were O_2:He:NO 45:150:0 and 45:150:1.4 mmol-s^{-1} and the discharge power was constant at 4500 W.

In order to obtain O_2(a) percent yield and gas temperature from the spectra affected by the NO_2* emission, a ramped baseline needs to be subtracted. The current data reduction relies on two Excel Macros. For the O_2(a) scans, a Macro reads the raw data and subtracts a ramped baseline. The Macro is a fast and easy way to correct the O_2(a) spectra almost immediately after data are taken in the laboratory. The Macro uses the corrected data to integrate the counts under the O_2(a) spectra, which are then used to calculate the O_2(a) percent yield [4.2]. Correcting the data quickly allows immediate calculations of O_2(a) percent yield. For the O_2(b) molecule, another Macro was written which also subtracts a ramped baseline from the data. The Macro then uses the procedure described in Section 3 to calculate the gas temperature [O_2(b)_Macro method]. The O_2(b) gas temperature then is used in the O_2(a) yield calculation.

For O_2(a) temperature determination [O_2(a)_MTD method], the raw data (no baseline applied) is read into the program. The program then calculates and applies a ramped baseline to the data. The procedure used to correct the ramped baseline is shown in Figure 4.5. The first ten and last ten count values are averaged to give points on the lower and higher wavelength side of the spectrum. The slope of the line between these point is calculated and divided by the total number of points in the O_2(a) scan (1024 points for the OMA) to get a slope-per-point value.

This slope-per-point value is then multiplied by the OMA point number (from 0 to 1024) and added to the original count value. For example, the first point on the lower wavelength side (Point 0) would get nothing added to it and the last point on the higher wavelength side (Point 1024) would get the most. This process rotates the spectrum to a level setting. Lastly, the average of the first ten count values is subtracted from the entire spectrum to lower the spectral tails to zero counts. The same process described above is used to subtract the ramped baseline from the O_2(b) spectra in the O_2(b)_MTD method.

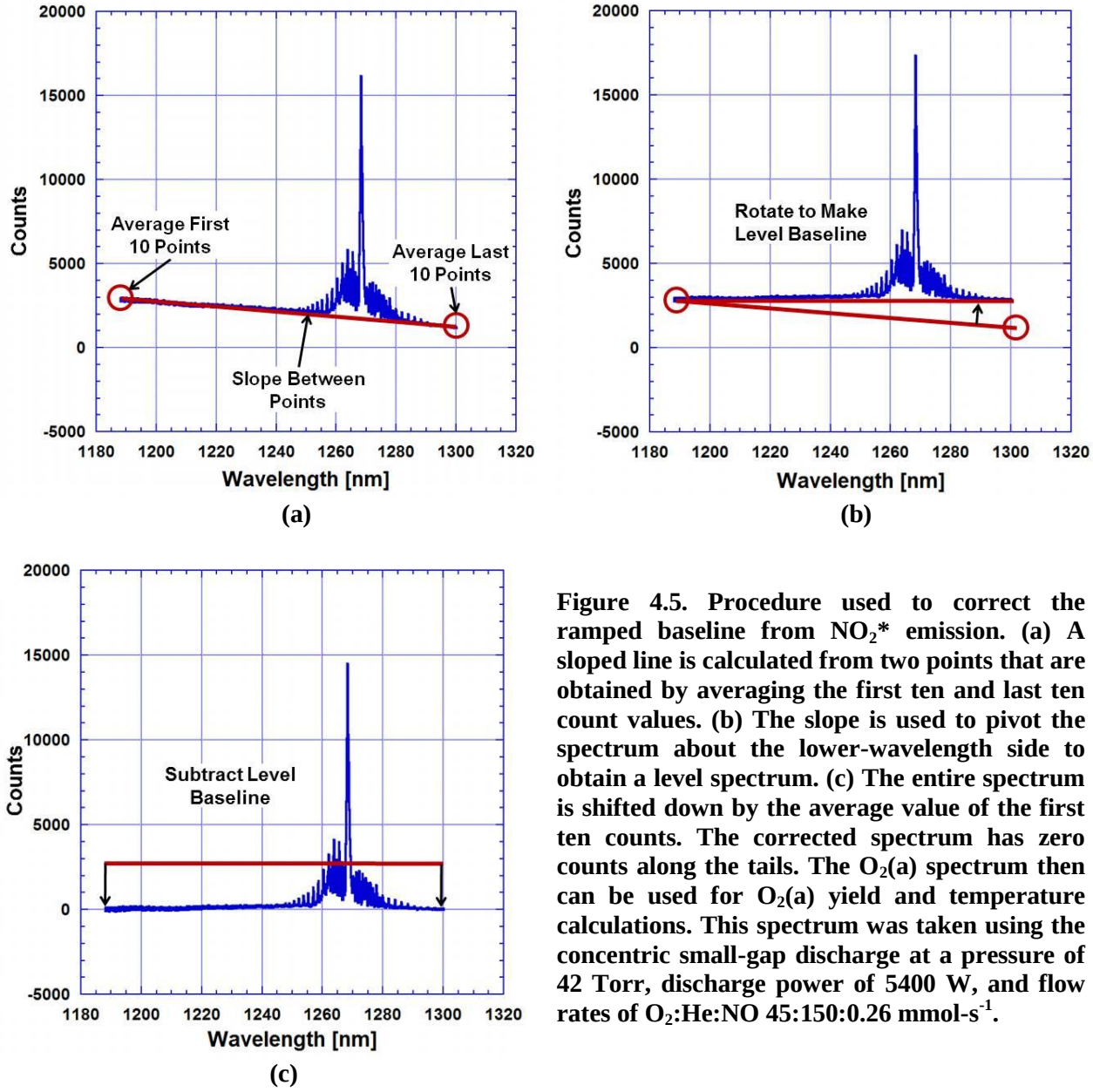

Figure 4.5. Procedure used to correct the ramped baseline from NO_2* emission. (a) A sloped line is calculated from two points that are obtained by averaging the first ten and last ten count values. (b) The slope is used to pivot the spectrum about the lower-wavelength side to obtain a level spectrum. (c) The entire spectrum is shifted down by the average value of the first ten counts. The corrected spectrum has zero counts along the tails. The O_2(a) spectrum then can be used for O_2(a) yield and temperature calculations. This spectrum was taken using the concentric small-gap discharge at a pressure of 42 Torr, discharge power of 5400 W, and flow rates of O_2:He:NO 45:150:0.26 mmol-s^{-1}.

In addition to the NO_2* emission, another excited state interferes with the O_2(a) measurement. The NO (C→A) emission affects O_2(a) measurements made immediately downstream from the discharge. A product of the discharge, the NO (C→A) emission is centered at 1220 nm [4.3] and extends from approximately 1200 nm to 1260 nm. Parts of the NO emission overlap with the O_2(a) spectra. The overlapping NO (C→A) and O_2(a) emission lines become superimposed, leading to elevated peaks and valleys in the O_2(a) emission. The elevated peaks and valleys in the O_2(a) emission result in calculated O_2(a) rotational temperatures that are higher than the actual flow temperature.

Figure 4.6 shows the effect of the NO (C→A) emission on an experimental O_2(a) spectrum taken approximately 5 cm downstream from the discharge. Since the measurement was taken so close to the discharge, the NO (C→A) emission affects the lower-wavelength side of the O_2(a) spectrum. Figure 4.6 also shows a "zoomed-in" version of the spectrum where the elevated peaks and valleys of the O_2(a) emission are seen. While the NO (C→A) emission has a dramatic effect on O_2(a) spectra near the discharge, it has a short lifetime and does not show up in spectra that are farther downstream. It is for this reason that the NO (C→A) emission cannot be seen in the remainder of the O_2(a) spectra presented in this thesis. However, the presence of the NO (C→A) emission makes O_2(a) temperature measurements and O_2(a) yield calculations immediately downstream from the discharge useless. This does not mean that gas temperature information cannot be obtained through other means. The NO (C→A) emission does not affect the O_2(b) spectrum, so temperature measurements immediately downstream from the discharge can be made using the O_2(b) emission.

The discussions above about the NO "air afterglow" and the NO (C→A) emission demonstrate that problems do exist when trying to measure O_2(a) spectra in EOIL without background noise from other excited states. Obtaining "clean" spectra without the background emissions are ideal for the matching process since the theoretical spectra used to calculate the gas temperature are not subject the same background emissions seen during experiments. Preprocessing the data to obtain O_2(a) measurements most resembling the theoretical spectra (i.e. tail baselines near zero) is the best way to obtain accurate results. But even preprocessing data cannot allow useful information to be obtained from some spectra. There are cases where the O_2(a) or O_2(b) spectra have too many background emissions or may lack a strong enough signal to allow useful calculations to be made. This topic will be revisited in the next section of this

thesis. The next subsection will present the first temperature calculations obtained from the $O_2(a)$ spectra.

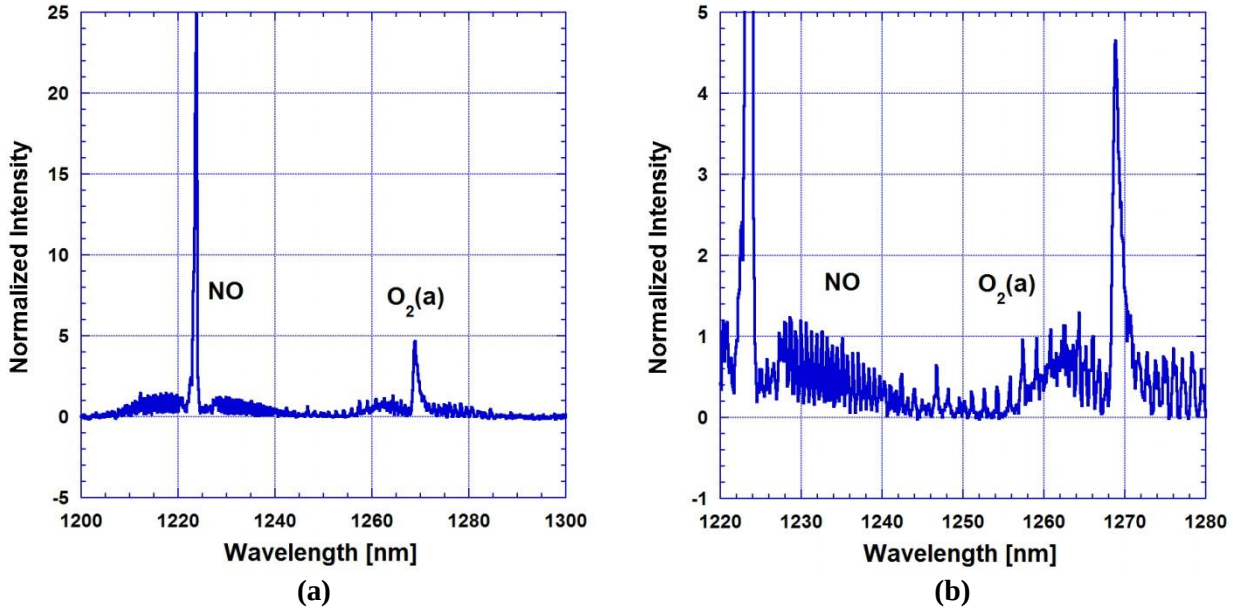

Figure 4.6. (a) $O_2(a)$ spectrum taken approximately 5 cm downstream from the discharge exit. Since the scan was taken very close to the discharge exit, the NO (C→A) emission is observed at 1220 nm. Emissions on the right-hand side of the NO (C→A) spectrum elevate the peaks and valleys of the $O_2(a)$ spectrum between 1250 and 1270 nm. The elevated peaks and valleys result in calculated $O_2(a)$ temperatures that are higher than the actual flow temperature. (b) Enhanced version of (a) showing the NO (C→A) emission affecting the left-hand side of the $O_2(a)$ spectrum. The flow rates were O_2:He:NO 45:150:0.26 mmol-s^{-1}, the pressure was 50 Torr, and the discharge power was 5000 W.

4.2 Gas Temperatures from $O_2(a)$ in VertiCOIL

To first test the $O_2(a)$ temperature determination method, $O_2(a)$ measurements made in the VertiCOIL system at UIUC-CUA were analyzed. Due to the high $O_2(a)$ yields in VertiCOIL, the $O_2(a)$ signal is very strong and the measured spectra have little or no background noise. The liquid chemistry used to produce $O_2(a)$ in VertiCOIL also ensures that no other species are present in the OMA scans. As previously described, the RF discharge and the addition of NO in EOIL creates other electronic states that interfere with both $O_2(a)$ and $O_2(b)$ signals. In some cases, the interaction of these excited states with the $O_2(a)$ and $O_2(b)$ emissions can hinder the temperature fit and give unreliable results.

Since the spectra from VertiCOIL provide the strongest $O_2(a)$ signals with the least background noise, they are the best starting point for the $O_2(a)$ temperature determination method. Obtaining good spectral fits and reasonable temperatures are the first steps toward proving that the $O_2(a)$ temperature method is possible. If the temperatures calculated from the VertiCOIL spectra are unreasonable based on physical intuition, then success of the $O_2(a)$ temperature method in the EOIL system [where $O_2(a)$ scans are not pristine] would be doubtful.

The $O_2(a)$ spectral measurements were taken in the VertiCOIL diagnostics duct. The diagnostics duct is downstream from the liquid SOG and upstream from the supersonic nozzle. The liquid chemistry in the SOG produces $O_2(a)$ which then flows upward into the diagnostics duct. Figure 4.7 shows a schematic of the VertiCOIL gas flow column. To obtain the data, one second exposures were taken using the OMA. Four different data series were taken (100s series through 400s series) as the gas flow rates and pressure were changed between data series. The average flow conditions for each series are provided in Table 4.1. The O_2 and chlorine flow rates are based off a chlorine utilization of 85 percent in the SOG. The $O_2(a)$ temperature fit was performed for each spectral measurement. The average temperature and standard deviation for each series are provided in Table 4.2.

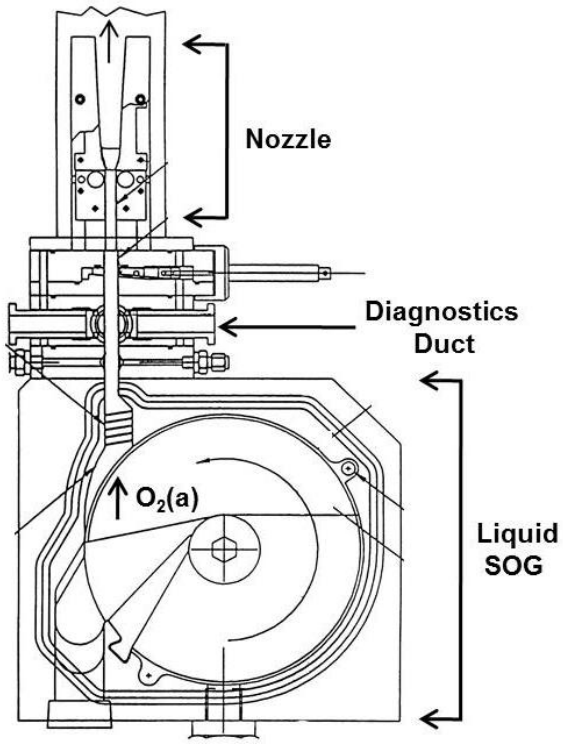

Figure 4.7. Schematic of the VertiCOIL gas flow column showing the liquid SOG, diagnostics duct, and nozzle. The $O_2(a)$ is produced in the SOG and travels upward, through the diagnostics duct, and into the nozzle. The $O_2(a)$ measurements were taken in the diagnostics duct using the OMA. The liquid temperatures in the SOG were approximately -22°C (251 K) for the 100s-300s series and -16°C (257 K) for the 400s series. Chlorine gas at approximately 20°C (293 K) was added at the top of the SOG for all four data series. The flow is from bottom to top.

Table 4.1. Flow Conditions for $O_2(a)$ Temperature Measurements in COIL

Series	Diagnostic Block Pressure [Torr]	Flow Rates [mmol-s^{-1}]			
		O_2	N_2	Cl	Total
100	17.5	20.9	71.4	3.70	96.0
200	20.5	20.5	72.4	3.60	96.5
300	32.0	31.5	107	5.50	144
400	46.6	64.9	107	12.1	184

Table 4.2. Gas Temperatures from $O_2(a)$ Measurements in COIL

Series	Number of Scans	Average Temperature [K]	Standard Deviation [K]	Range [K]
100	25	252	1.37	5.05
200	25	255	2.81	8.80
300	20	270	2.69	8.72
400	15	298	3.12	10.2

There are a number of points to be made about the temperature results. First, the small standard deviation for each data series shows that the calculated temperatures are precise. Since the scans were taken rapidly for each hundreds series, it is expected that the gas temperatures should be close in magnitude. Second, the average gas temperature increases as each successive series was taken. The increasing temperature can be explained by the increasing gas flow rates and the corresponding pressure rise. These results show that the $O_2(a)$ temperature determination method captures the expected trend in the data. Last, the gas temperatures are also reasonable based on the other temperatures being measured in the VertiCOIL system. The liquid in the SOG was approximately -22°C (251 K) for the 100s-300s series and -16°C (257 K) for the 400s series. The 251 K liquid SOG temperature matches closely with the 252 K average gas temperature of the 100s series. As the pressure increases in the 300s and 400s series, the gas is travelling slower and has more time to heat up between leaving the SOG and entering the diagnostics duct. Therefore, it is expected that the temperatures for the 300s and 400s series would increase with pressure. Also, the chlorine gas is entering the SOG at approximately 20°C (293 K). So increasing the chlorine flow rate increases the amount of hot gas entering the SOG and should increase the overall flow temperature. Again, this behavior is captured in the temperatures.

Experimental $O_2(a)$ spectra and theoretical temperature fits from the 100s, 300s, and 400s series are shown in Figure 4.8. The calculated temperatures for each of these spectra can be

found in Table 4.3. The calculated temperatures from O_2(a)_MTD were compared to the O_2(a) rotational temperatures obtained by a correspondent from PSI. The correspondent from PSI has independently developed a method for computing temperatures from O_2(a) spectra [4.4]. The same data used by O_2(a)_MTD was sent to the PSI correspondent, and the temperatures calculated by this individual are listed in Table 4.3.

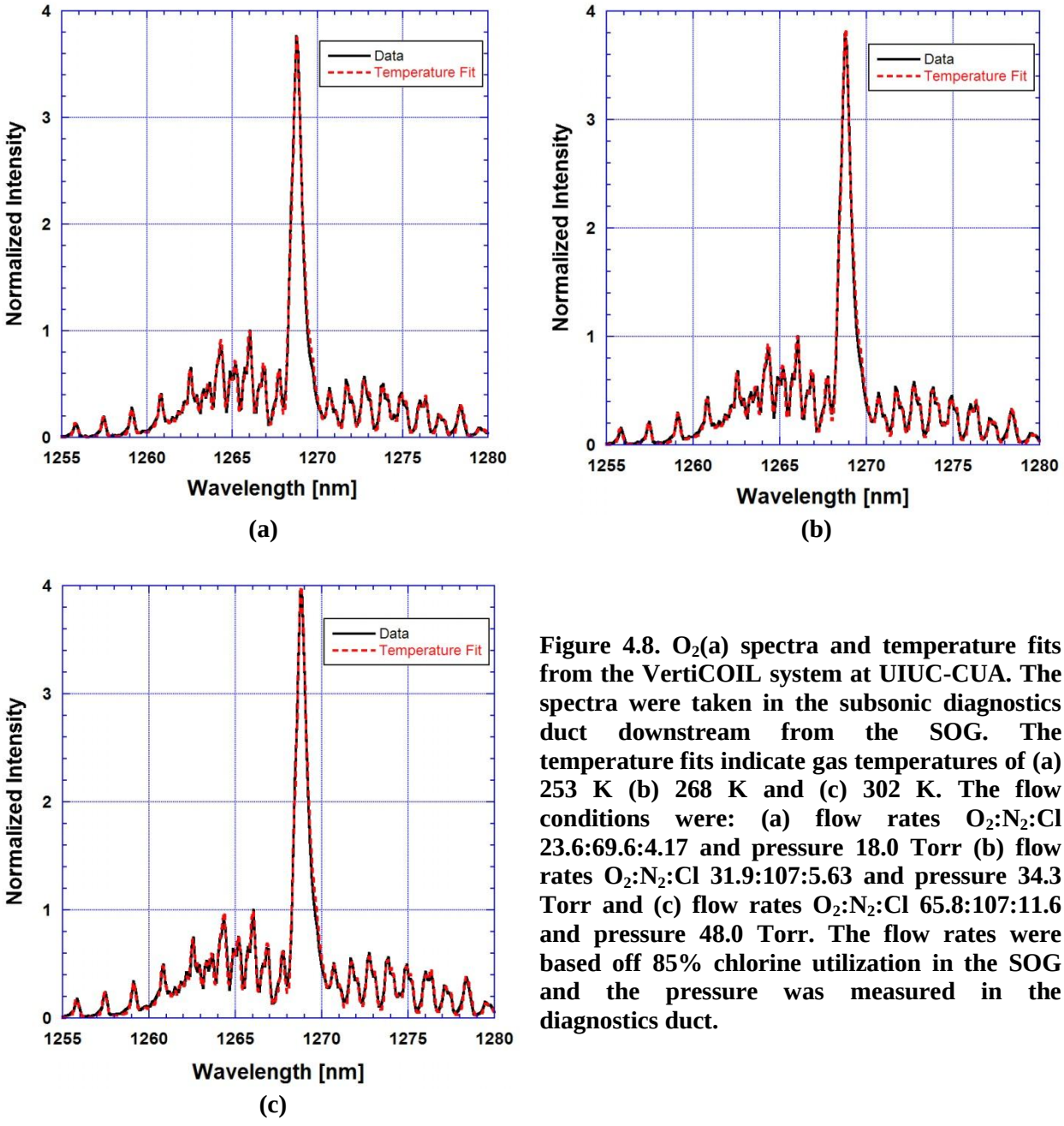

Figure 4.8. O_2(a) spectra and temperature fits from the VertiCOIL system at UIUC-CUA. The spectra were taken in the subsonic diagnostics duct downstream from the SOG. The temperature fits indicate gas temperatures of (a) 253 K (b) 268 K and (c) 302 K. The flow conditions were: (a) flow rates O_2:N_2:Cl 23.6:69.6:4.17 and pressure 18.0 Torr (b) flow rates O_2:N_2:Cl 31.9:107:5.63 and pressure 34.3 Torr and (c) flow rates O_2:N_2:Cl 65.8:107:11.6 and pressure 48.0 Torr. The flow rates were based off 85% chlorine utilization in the SOG and the pressure was measured in the diagnostics duct.

Table 4.3. $O_2(a)$ Temperatures from COIL Data

OMA Scan	Temperature $O_2(a)$_MTD [K]	Temperature $O_2(a)$ PSI [K]
101	253	245 ± 5
301	268	265 ± 5
401	302	300 ± 5

The $O_2(a)$ temperatures obtained from $O_2(a)$_MTD agree very well with the temperatures obtained by the PSI correspondent. The calculated temperatures are remarkably close to one another given that they were calculated using independently-developed methods. One thing to note is that the temperatures calculated from the PSI correspondent have upper and lower error bars, while the calculated temperatures from $O_2(a)$_MTD do not. Determining upper and lower error bars is still a work in progress for $O_2(a)$_MTD.

4.3 Gas Temperatures versus Discharge Operating Time

Originally, calculations of gas temperature had been plotted against discharge power since the flow temperature is expected to increase as more power is deposited into the gas. However, plots of gas temperature versus discharge power did not always show consistent trends. This inconsistency occurs because the tube walls heat up and increase the gas temperature while the discharge operates. This effect is usually seen during discharge power sweeps when trying to optimize $O_2(a)$ production. During these experiments, the discharge is turned on and matched such that the forward power going into the discharge is ideal. The discharge matching procedure is not always immediate and can take several minutes to complete. Since the discharge needs to be operating for matching to occur, the flow tubes heat up during the matching process. By the time the discharge is matched and the OMA and CCD scans are taken, the flow temperature can change. Plotting gas temperature versus discharge power is not ideal since the discharge operating time affects the gas temperature.

To examine the effect of discharge operating time on gas temperature, three experiments were conducted to measure the temporal rise of gas temperature at constant input power. These experiments also allow four different temperature diagnostics to be compared: $O_2(a)$_MTD, $O_2(b)$_MTD, $O_2(b)$_BSW, and $O_2(b)$_Macro. Descriptions of each method can be found in Section 3 of this thesis. In prior experiments, temperature calculations from $O_2(a)$ and $O_2(b)$ were not in agreement. In general, the calculated $O_2(a)$ temperatures were higher than the $O_2(b)$

temperatures. One hypothesis for this difference was that the O_2(a) and O_2(b) temperature measurements approached equilibrium temperatures at different rates, and therefore provided different temperature readings at different times. It was thought that both O_2(a) and O_2(b) measurements would approach the same steady-state temperature when given enough time. The following experiments allowed this hypothesis to be tested.

Three experiments were conducted to examine the effect of discharge operating time on gas temperature. For the first experiment, the OMA and CCD fibers were oriented approximately 16.5 cm downstream from the discharge. Two clamshell discharges (5-cm diameter) [4.5] were operated in series at 1000 W and 20 Torr. Figure 4.9 shows a schematic and photograph of the experimental setup. To examine the effect of NO on the temperature calculations, data was taken with and without NO. Flow rates were O_2:He:NO 10:33:0.17 mmol-s^{-1} and 10:33:0 mmol-s^{-1}. The discharge was turned on and matched prior to any spectral measurements. After matching was completed, the discharge was turned off and the flow tubes were allowed to cool to room temperature. This allowed the experimenters to turn on the pre-matched discharge and begin measurements, avoiding the usual time spent matching the discharge. Ten second measurements were taken immediately after the discharge was turned on and continued every 15 seconds for a period of approximately 150 seconds.

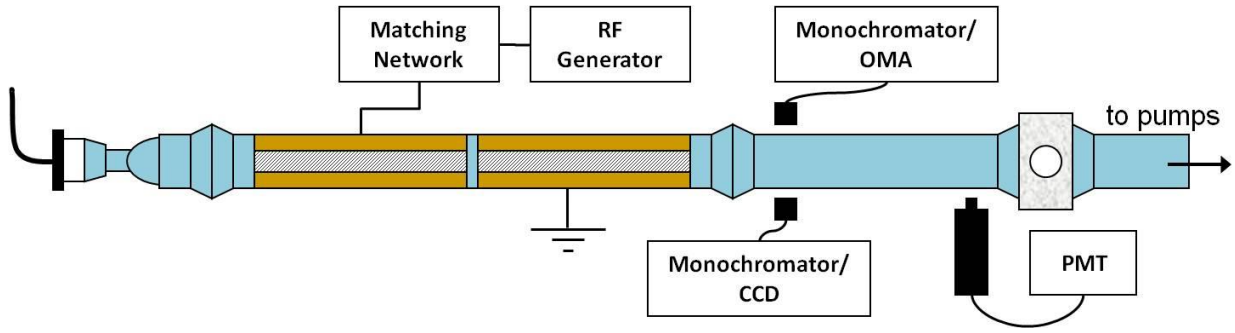

(a)

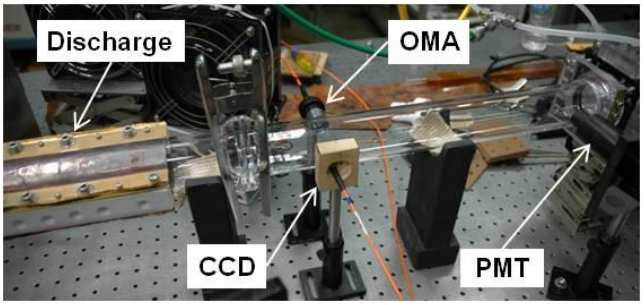

(b)

Figure 4.9. (a) Schematic of the experimental setup for the first temporal sweep of gas temperature. Two clamshell discharges were operated in series at 1000 W and 20 Torr. The OMA and CCD fibers were oriented 16.5 cm downstream from the discharge. The PMT was located farther downstream. (b) Photograph of the experimental setup.

Figure 4.10 shows the calculated gas temperatures versus discharge operating time using the four different methods. As expected, the flow temperature increases as the discharge operating time increases, even though the power input, gas flow rates, and pressure are held constant. For the case with NO, the calculated temperatures are somewhat erratic for all four methods. However, each method captures the expected trend of the gas temperature increasing with time. For the case without NO, the calculated flow temperatures from O_2(a)_MTD, O_2(b)_MTD, and O_2(b)_BSW all exhibit the same behavior and track one another reasonably well. A source of discrepancy between the calculations made from the data with NO versus the data without NO may be the "air afterglow" seen in the scans with NO. While the plots in Figure 4.10 provide some useful information, they do not reveal a steady-state temperature since both plots indicate that the gas temperature is still increasing with time. For the second and third experiments, the time period was extended beyond 150 seconds to capture the steady-state temperature.

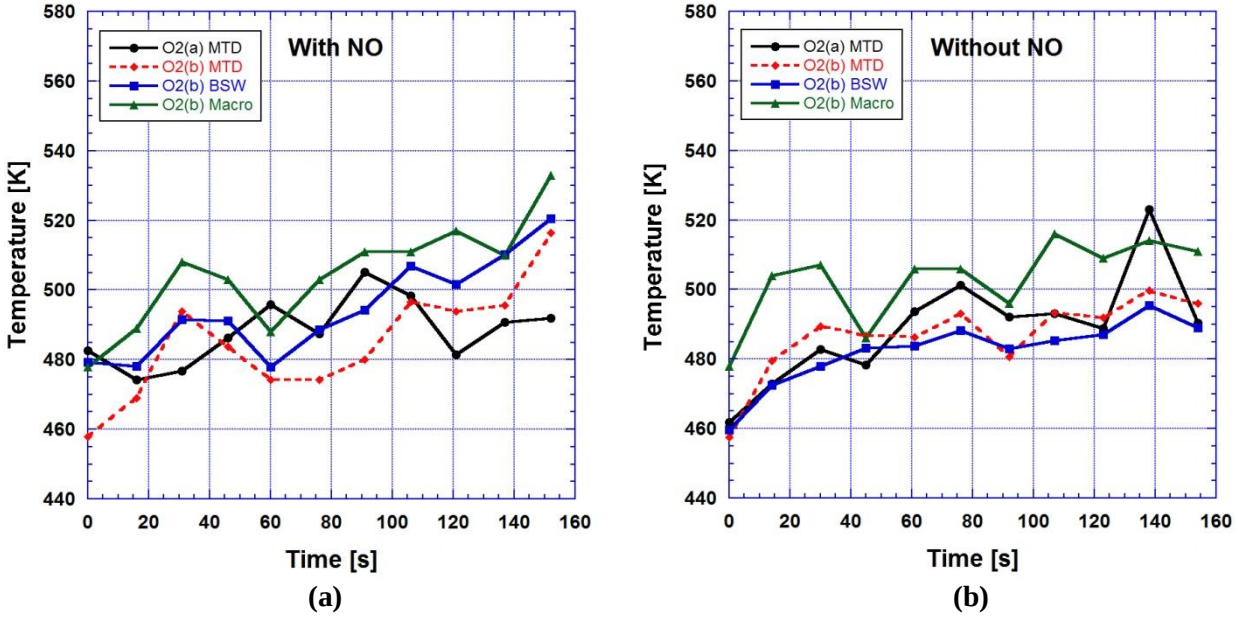

Figure 4.10. Gas temperature versus discharge operating time (a) with NO and (b) without NO. Flow conditions were O_2:He:NO 10:33:0.17 mmol-s^{-1} and 10:33:0 mmol-s^{-1}. Discharge power and pressure were held constant at 1000 W and 20 Torr, respectively. Four methods were used to determine gas temperature: O_2(a)_MTD, O_2(b)_MTD, O_2(b)_BSW, and O_2(b)_Macro.

The second experimental setup was very similar to the first. The only difference was that the PMT was moved to the CCD and OMA measurement locations so that O atom measurements

could be made. Figure 4.11 shows a schematic and photograph of the experimental setup. Ten second OMA and CCD measurements were made every 15 seconds for a period of 300 seconds. Again, data series were taken with and without NO. The discharge power and pressure were set at 1000 W and 20 Torr and the flow rates were O_2:He:NO 10:33:0.16 mmol-s^{-1} and 10:33:0 mmol-s^{-1}.

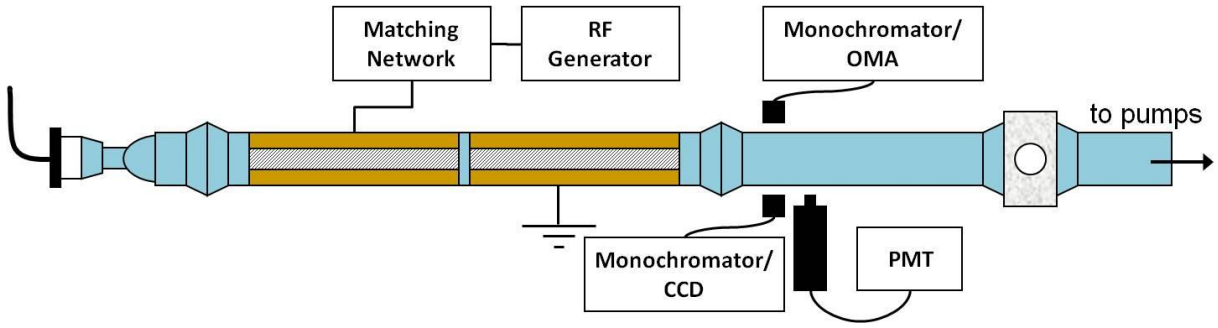

(a)

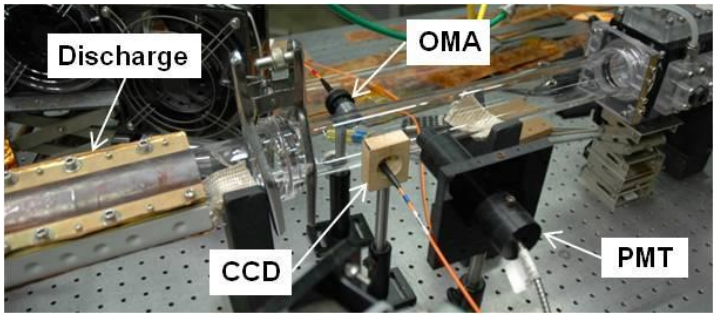

(b)

Figure 4.11. (a) Schematic of the experimental setup for the second temporal sweep of gas temperature. Two clamshell discharges were operated in series at 1000 W and 20 Torr. The OMA, CCD, and PMT were 16.5 cm downstream from the discharge. (b) Photograph of the experimental setup.

Figure 4.12 shows the calculated gas temperatures versus discharge operating time using the four different methods. Again, all four methods show an increase in temperature as the discharge operating time increases. However, a consistent steady-state temperature never seems to be reached for the case with NO. For instance, the flow temperature spikes up and down between 200 and 250 seconds for all four methods. This shows that calculated gas temperature fluctuations can be as high 40 K between measurements made 15 seconds apart. There is also a noticeable discrepancy between the four temperature measurements. The lack of agreement between the four methods for the case with NO is again attributed to the "air afterglow" that affects the experimental spectra. The flow temperatures are much more consistent for the case without NO. The gas temperatures are all within 30 K at the last data point and seem to be leveling out to a steady-state value.

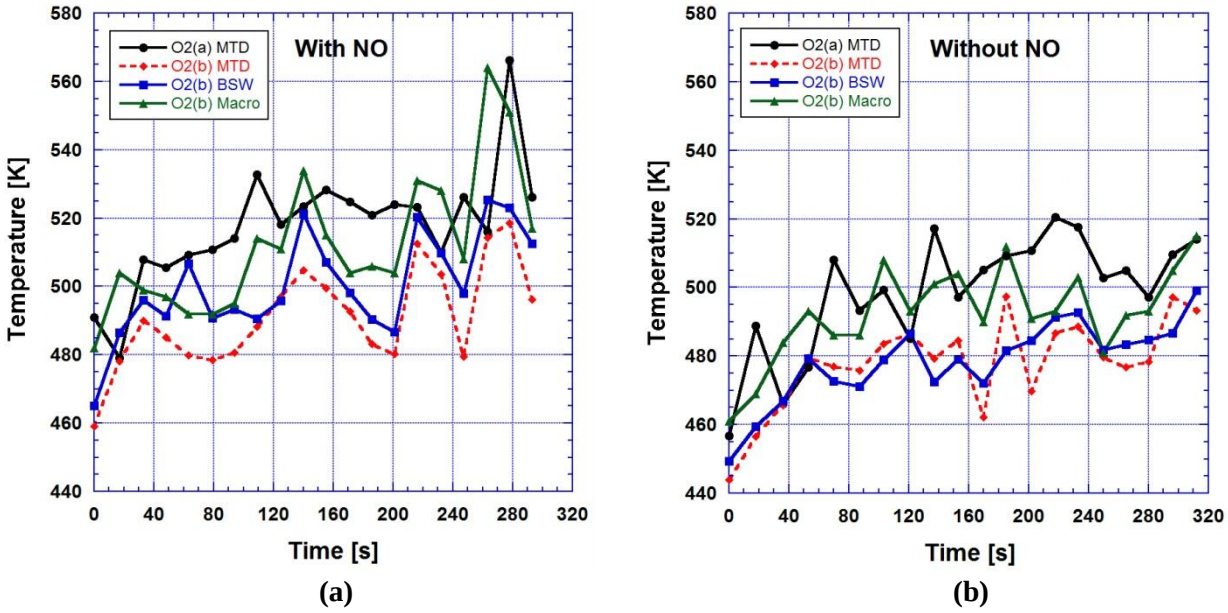

Figure 4.12. Gas temperature versus discharge operating time (a) with NO (b) without NO. Flow conditions were O_2:He:NO 10:33:0.16 mmol-s^{-1} and 10:33:0 mmol-s^{-1}. Discharge power and pressure were held constant at 1000 W and 20 Torr, respectively. Four methods were used to determine gas temperature: O_2(a)_MTD, O_2(b)_MTD, O_2(b)_BSW, and O_2(b)_Macro.

For the last experiment, the OMA and CCD measurements were moved farther downstream to the diagnostics duct. The discharge power was also lowered to 600 W. Lowering the discharge power and moving the OMA and CCD measurements farther away from the discharge was done to limit the background "air afterglow" from the NO_2* emission. The PMT was positioned in front on the diagnostics duct so that O atom measurements could be made. Figure 4.13 shows a schematic and photograph of the experimental setup. Twenty second scans were taken every 30 seconds for a period of 350 seconds. The pressure was set at 20 Torr and the flow rates were O_2:He:NO 10:33:0.18 mmol-s^{-1} and 10:33:0 mmol-s^{-1}.

Figure 4.14 shows the calculated gas temperatures versus discharge operating time. Due to the lower discharge power and the increased length between the discharge and the measurement location, the gas temperature is much lower than the previous two experiments. Also, the gas temperature does not seem to be increasing with time at the same rate as the previous two experiments. Again, this is attributed to the lower discharge power and increased length between the discharge and measurement location. The lower discharge power means that it takes less time for the gas to reach the steady-state temperature. The gas temperatures shown in Figure 4.14 either have reached steady-state or are approaching steady-state at a much lower rate.

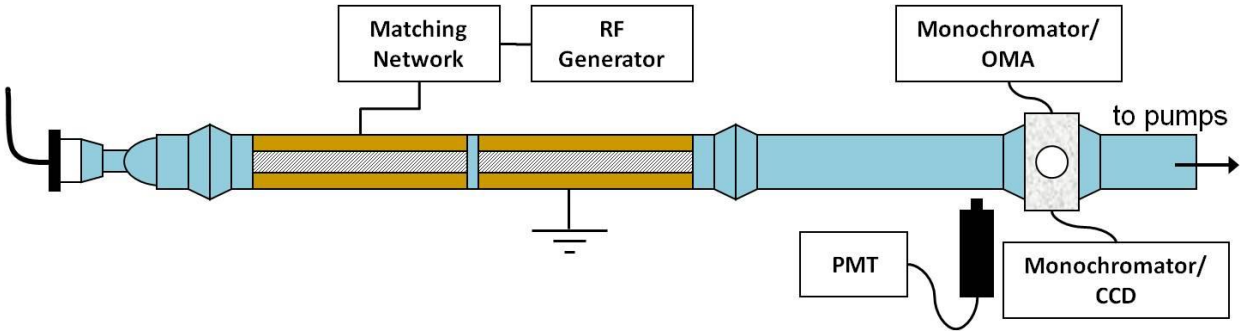

(a)

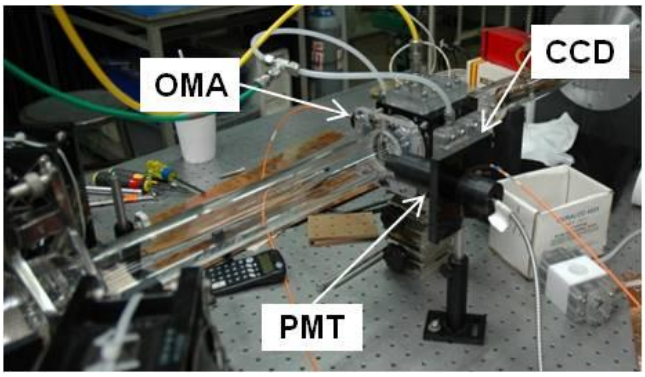

(b)

Figure 4.13. (a) Schematic of the experimental setup for the third temporal sweep of gas temperature. Two clamshell discharges were operated in series at 600 W and 20 Torr. The OMA and CCD were positioned in the diagnostics block. The PMT was positioned in front of the diagnostics block. (b) Photograph of the experimental setup.

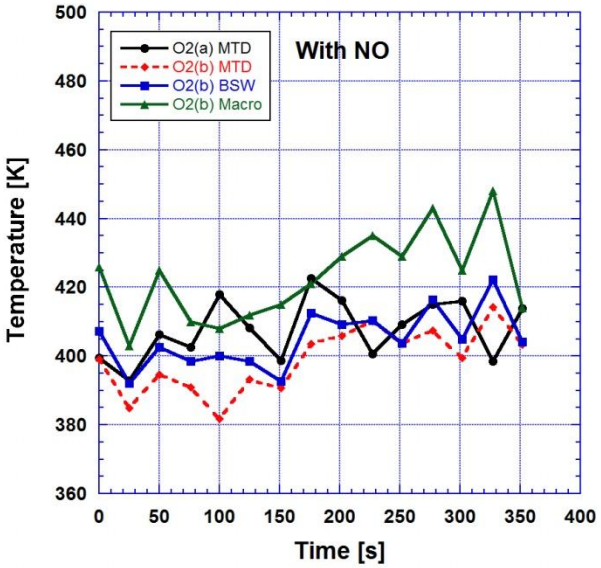

(a)

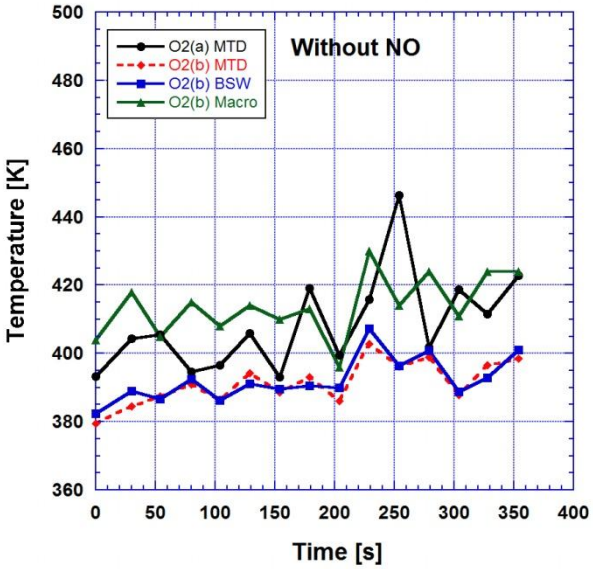

(b)

Figure 4.14. Gas temperature versus discharge operating time (a) with NO (b) without NO. Flow conditions were O_2:He:NO 10:33:0.18 mmol-s^{-1} and 10:33:0 mmol-s^{-1}. Discharge power and pressure were held constant at 600 W and 20 Torr, respectively. Four methods were used to determine gas temperature: O_2(a)_MTD, O_2(b)_MTD, O_2(b)_BSW, and O_2(b)_Macro.

A few general conclusions can be made about the results obtained from the three experiments described above. In all three experiments, the calculated flow temperatures seemed to increase and drop erratically at some points. This is evident by unexpected spikes and valleys in the plots. Instead of observing constantly increasing temperatures, the plots seemed to behave as if something else was causing the spikes and valleys. Due to the more erratic features of the plots with NO, it can be assumed that the "air afterglow" is responsible for these effects. The most obvious observation from the above experiments is that the four methods do not give the same calculated flow temperatures, even at steady-state. Some hypotheses for this lack of agreement are provided in the next section of this thesis.

4.4 Laser Cavity Temperatures from $O_2(a)$ and $O_2(b)$

One of the main purposes of an $O_2(a)$ temperature diagnostic is to measure temperature in the supersonic cavity. The goal of this experiment was to measure temperature in the laser cavity versus the discharge power. For this experiment, the rectangular quartz discharge tube and HEX-1 were attached to the Cav6 laser hardware. The pressures and flow rates were set according to values normally used for gain and laser power experiments. The discharge pressure was held constant at about 46 Torr and the primary flow rates were O_2:He:NO 45:150:0.26 mmol-s^{-1}. The only gas that was not added to the system was iodine, as the I* emission would interfere with the $O_2(a)$ measurement. Even though it did not carry iodine, the warm helium carrier gas was still injected in the nozzle at a flow rate of 42 mmol-s^{-1}. Tertiary nitrogen gas was injected in the nozzle at a flow rate of 295 mmol-s^{-1} and a temperature of -185°C (88 K). Figure 4.15 shows a schematic and photograph of the experimental setup. The discharge power was varied between 1000 W and 4000 W. Thirty second OMA and CCD measurements were taken at each input power. The results from the temperature fits can be found in Table 4.4.

The calculated temperatures from $O_2(a)$_MTD, $O_2(b)$_MTD, and $O_2(b)$_BSW are in good agreement. The calculated temperatures from the $O_2(b)$_Macro are not consistent with the other values. This is due to the poor signal quality of the peaks used in the $O_2(b)$_Macro calculation. Also, since the $O_2(b)$_Macro method only uses two peaks to calculate temperature, any small deviations in these peaks can cause poor temperature results. The $O_2(b)$_Macro method lacks the robustness needed to measure temperatures in the laser cavity. It is also interesting to note that the laser cavity temperature does not experience drastic changes when the discharge power

increases. During discharge optimization experiments, such drastic changes to discharge power usually show very large increases in gas temperature. However, the gas temperature in the cavity increases only by about 10 K after power increases from 1000 W to 4000 W.

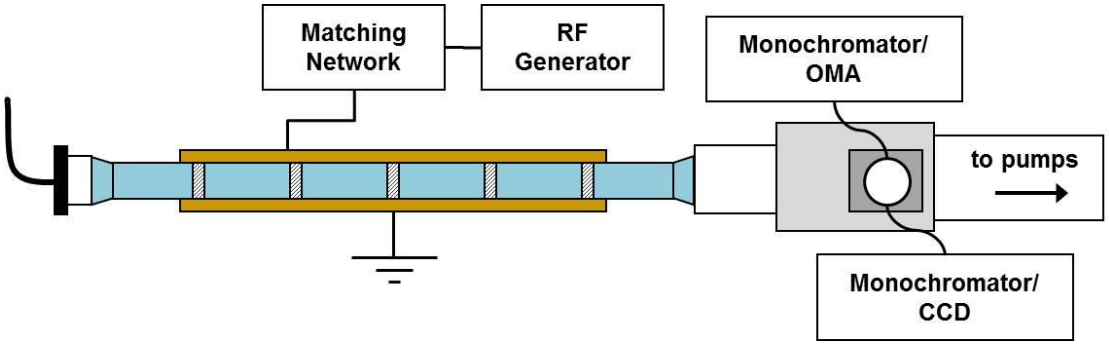

(a)

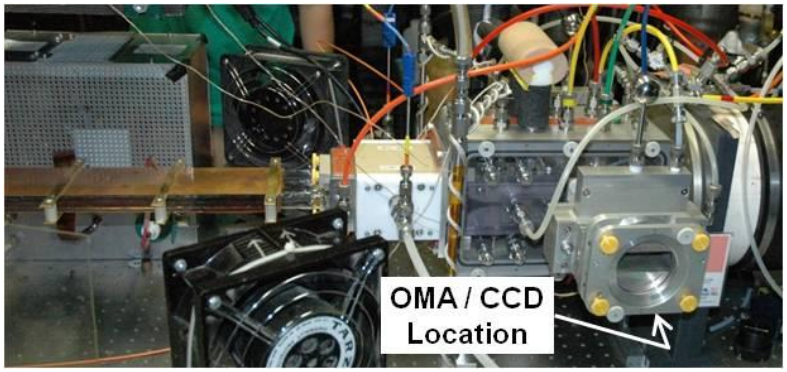

(b)

Figure 4.15. (a) Schematic of the experimental setup used to measure gas temperature in the nozzle. The rectangular quartz discharge was operated at different powers. The OMA and CCD fibers were located near the Cav6 mirror mounts. (b) Photograph of the experimental setup.

Table 4.4. Laser Cavity Temperatures from O_2(a) and O_2(b) Spectra

Discharge Power [W]	Calculated Temperature [K]			
	O_2(a)_MTD	O_2(b)_MTD	O_2(b)_BSW	O_2(b)_Macro
1000	111	90	NA	NA
2000	113	98	102	207
3000	116	102	104	175
4000	114	104	105	163
4000	117	105	107	156
4000	96	92	90	154

Figure 4.16 shows experimental O_2(a) and O_2(b) spectra from the laser cavity. The O_2(a) spectrum indicated a laser cavity temperature of 114 K and the O_2(b) gave a temperature of 104 K. For an additional comparison, the O_2(a) spectra shown in Figure 4.16 was sent to the

correspondent at PSI who performed a temperature fit to the data [4.4]. The PSI correspondent calculated a gas temperature of 105 ± 5 K, which is in agreement with the values obtained in this work.

Immediately following the O_2(a) and O_2(b) scans in the cavity, gain measurements were made as a function of RF power. Since gain measurements require the I* state, O_2(a) and O_2(b) measurements cannot be made concurrently with the gain measurements. To compare gain temperatures measured in the cavity to the O_2(a) and O_2(b) measurements, the same flow rates (with the addition of iodine), pressure, and discharge power were used. The gain measurements indicated a flow temperature of 160 K. However, the experimenters suspect that RF interference from the discharge may have disrupted the gain diagnostic tools. Gain temperatures between 120 K and 130 K are usually seen in the laser cavity. Table 4.5 summarizes the temperature measurements in the cavity.

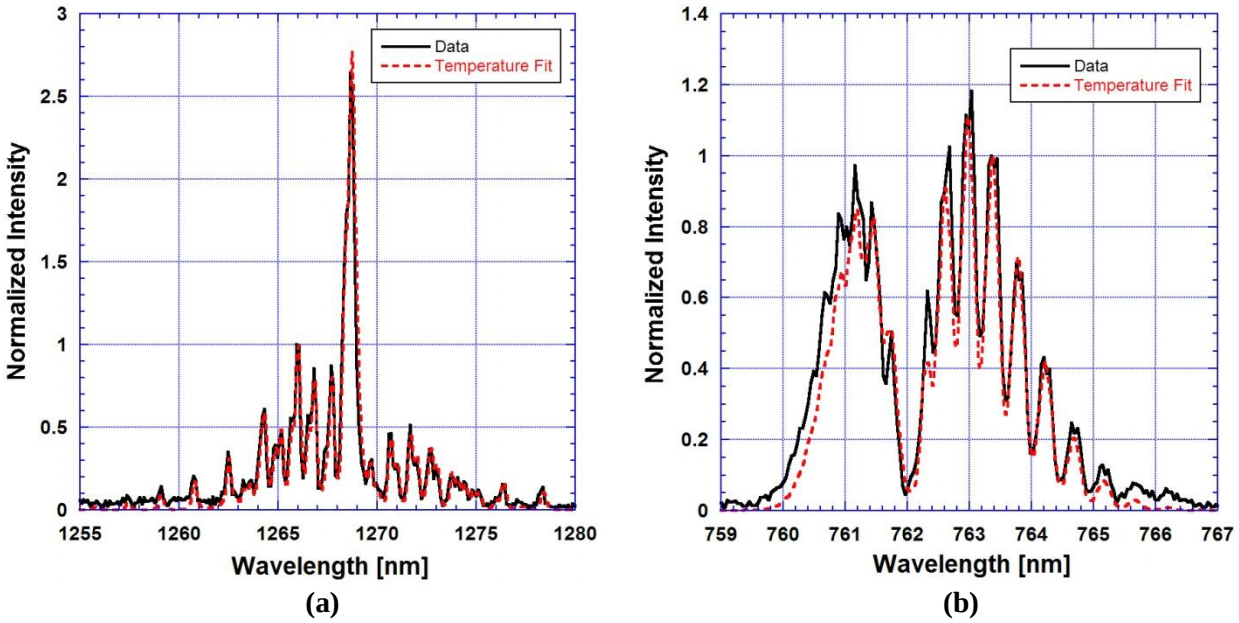

Figure 4.16. (a) O_2(a) spectrum and temperature fit and (b) O_2(b) spectrum and temperature fit [using O_2(b)_MTD] from measurements made in the laser cavity. The temperature fits indicate gas temperatures of 114 K for the O_2(a) spectrum and 104 K for the O_2(b) spectrum. The discharge power was 4000 W and the flow rates were O_2:He:NO 45:150:0.26 mmol-s^{-1} and He:N_2 42:295 mmol-s^{-1} with N_2 temperature of -183°C (88 K). The nozzle pressure was approximately 5 Torr.

Table 4.5. Summary of Laser Cavity Temperature Measurements in [K]

O_2(a)_MTD	O_2(a)_PSI	O_2(b)_MTD	O_2(b)_BSW	O_2(b)_Macro	Gain
114	105 ± 5	104	105	163	160

In addition to the above experiment, other cavity temperature measurements were made using O_2(a) spectra. Table 4.6 lists additional laser cavity temperature measurements made from O_2(a) spectra. The primary oxygen and helium flow rates were O_2:He 45:150 mmol-s^{-1} for each measurement. The data in Table 4.6 are from four other experiments that were conducted using a similar setup to the previous experiment. The only difference was that the data were taken using the 6-tube discharge. The data in Table 4.6 shows that laser cavity temperature measurements using O_2(a) spectra provide consistent results from one experiment to the next.

Table 4.6. Additional Cavity Temperature Measurements from O_2(a) Spectra

Discharge Power [W]	O_2(a)_MTD Temperature [K]	Discharge Pressure [Torr]	Flow Rates [mmol-s^{-1}]			N_2 Temperature [K]
			NO	He Carrier	N_2	
4800	108	46.5	0.57	40	303	91
4800	105	46.4	0.57	40	309	91
5000	98	46.5	0.62	39	315	83
5000	98	46.5	0.62	39	315	83
4900	105	45.7	0.65	NA	307	81
4900	109	46.1	0.65	NA	307	84
5000	101	46.2	0.47	NA	306	80
5000	103	47.4	0.47	NA	306	80
5000	102	47.5	0.47	NA	306	80
5000	100	47.6	0.47	NA	306	80
5000	99	47.4	0.47	NA	306	80
5000	100	47.4	0.47	NA	306	80

4.5 Discharge Exit Temperatures from O_2(b)

The previous subsection presented the results of gas temperatures calculated from O_2(a) and O_2(b) spectra in the laser cavity. The laser cavity is the part of the EOIL system with the lowest gas temperatures due to supersonic expansion and the addition of N_2 gas at temperatures between 80 K and 95 K. On the other hand, gas temperatures are highest at the discharge exit. Since it is advantageous to have a robust temperature diagnostic capable of measuring the wide range of temperatures in the EOIL system, flow temperatures at the discharge exit were measured. As previously mentioned, the O_2(a) spectra at the discharge exit contain too much interference from the NO (C→A) emission for accurate temperature calculations. Therefore, only the O_2(b) spectra will be used for temperature calculations at the discharge exit.

The purpose of the following experiment was to measure the gas temperature exiting the discharge at different discharge powers to see if the O_2(b) temperature calculations followed expected trends. For this experiment, the OMA and CCD fibers were positioned 5 cm downstream from the discharge exit. The rectangular quartz discharge tube and HEX-1 heat exchanger were attached to the Cav6 laser hardware. The discharge pressure and flow rates were constant at 50 Torr and O_2:He:NO 45:150:0.26 mmol-s^{-1}, respectively. The discharge power was varied from 1000 W to 5000 W. Figure 4.17 shows a schematic and photograph of the experimental setup.

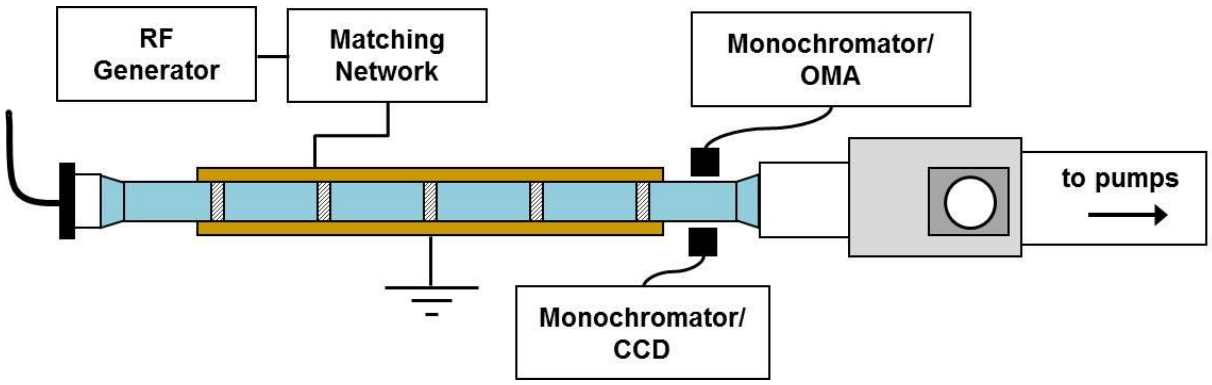

(a)

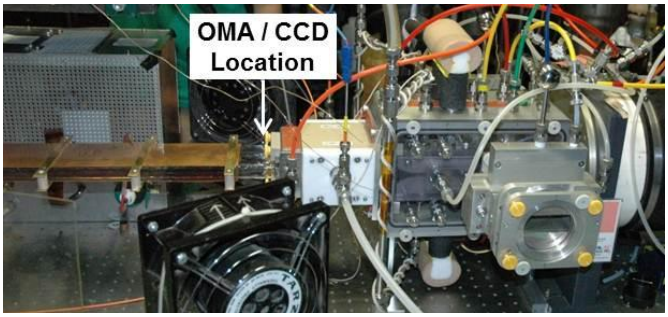

(b)

Figure 4.17. (a) Schematic of the experimental setup used to measure the gas temperature at the discharge exit. The rectangular quartz discharge tube and HEX-1 heat exchanger were attached to the Cav6 laser hardware. The OMA and CCD fibers were positioned 5 cm downstream from the discharge exit. (b) Photograph of the experimental setup.

Figure 4.18 shows the measured O_2(b) spectra at different discharge powers. As expected, increasing the discharge power increases the gas temperature. Increasing the gas temperature changes the intensity values of the various transitions as the population of upper rotational states redistributes. In the R-branch (left-hand side), the higher temperatures favor the lower-wavelength emissions. This behavior is seen in 4.18(b) as the higher temperature spectra have a higher amplitude and more distinct peak. In the P-branch [Figure 4.18(c)], higher temperatures result in greater intensities at higher-wavelength emissions.

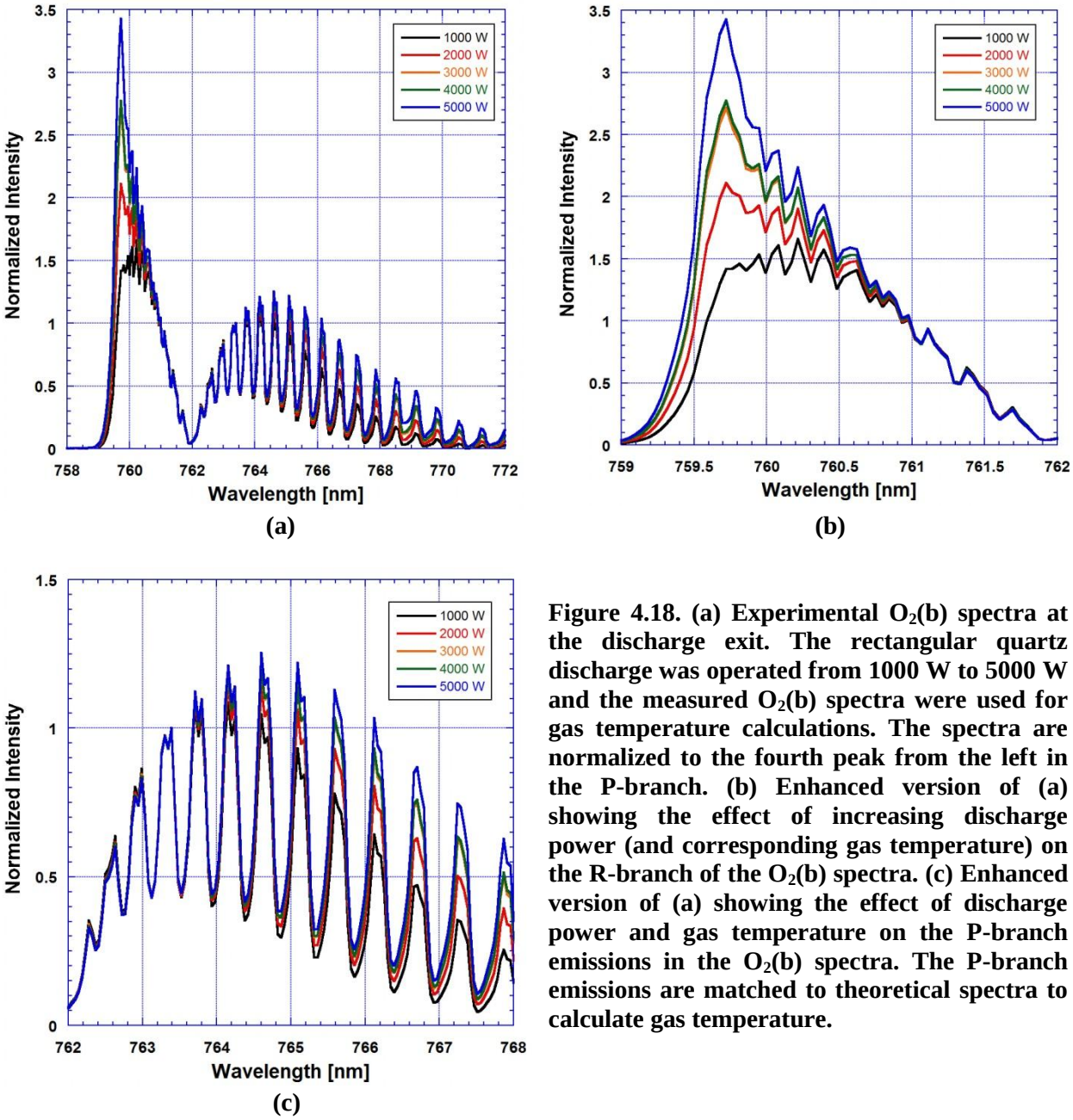

Figure 4.18. (a) Experimental O_2(b) spectra at the discharge exit. The rectangular quartz discharge was operated from 1000 W to 5000 W and the measured O_2(b) spectra were used for gas temperature calculations. The spectra are normalized to the fourth peak from the left in the P-branch. (b) Enhanced version of (a) showing the effect of increasing discharge power (and corresponding gas temperature) on the R-branch of the O_2(b) spectra. (c) Enhanced version of (a) showing the effect of discharge power and gas temperature on the P-branch emissions in the O_2(b) spectra. The P-branch emissions are matched to theoretical spectra to calculate gas temperature.

The gas temperatures were calculated using the three different O_2(b) methods: O_2(b)_MTD, O_2(b)_BSW, O_2(b)_Macro. Figure 4.19 shows the calculated temperatures plotted against discharge power. In plotting against discharge power, it is assumed that the discharge was matched quickly and the flow tube heating due to discharge operating time did not greatly affect the gas temperature. In this case, Figure 4.19 shows a direct relationship between gas temperature and discharge power. Figure 4.19 also shows that gas temperatures exiting the discharge can vary between 400 K and 650 K based on discharge power.

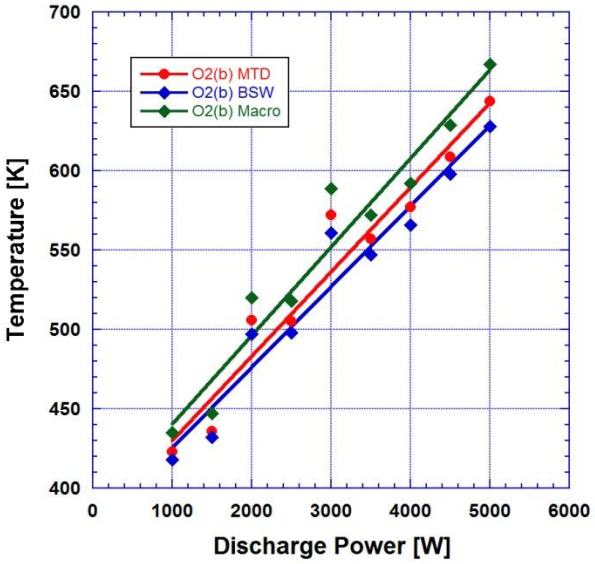

Figure 4.19. Gas temperature measurements versus discharge power approximately 5 cm downstream from the discharge. The discharge power was varied and the gas temperature was calculated using the three different O_2(b) diagnostics: O_2(b)_MTD, O_2(b)_BSW, O_2(b)_Macro.

Figures 4.20-4.22 show three experimental O_2(b) spectra measured immediately downstream from the discharge and the calculated temperature fits. The three spectra shown in Figures 4.20-4.22 were measured at low (1000 W), medium (3000 W), and high (5000 W) discharge powers. The theoretical temperature fits match the expected behavior along the P and R-branches as the discharge power and gas temperature are increasing.

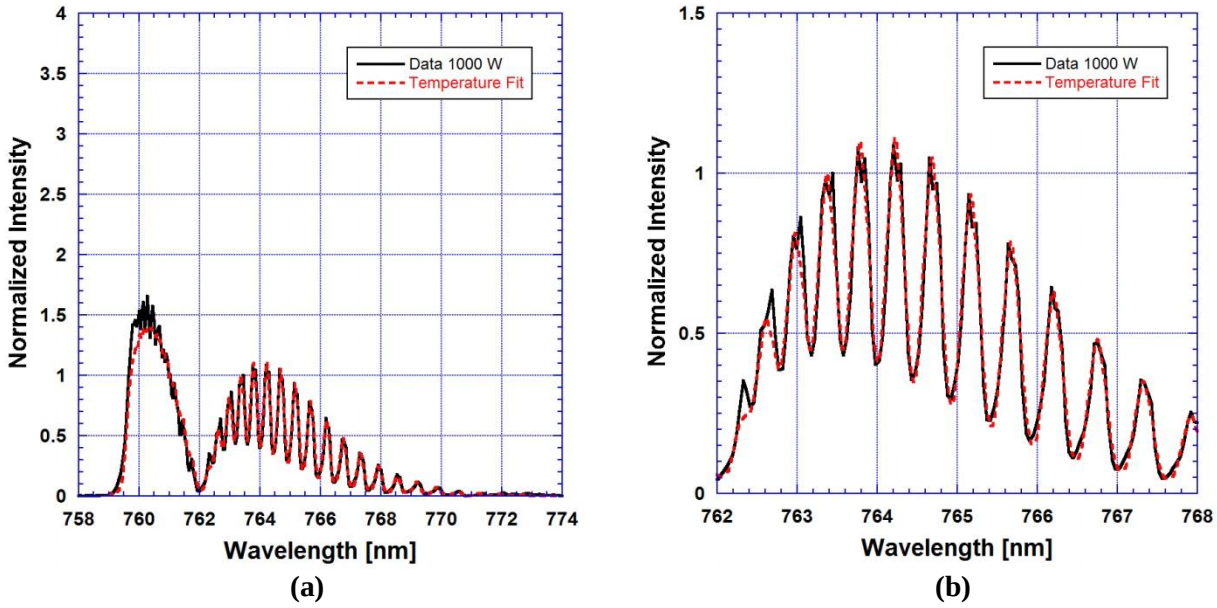

Figure 4.20. (a) O_2(b) spectrum at 1000 W and temperature fit indicating a gas temperature of 424 K [O_2(b)_MTD method]. (b) Enhanced version of (a) showing the temperature fits to the P-branch. The flow rates were O_2:He:NO 45:150:0.26 mmol-s^{-1} and the discharge pressure was 50 Torr.

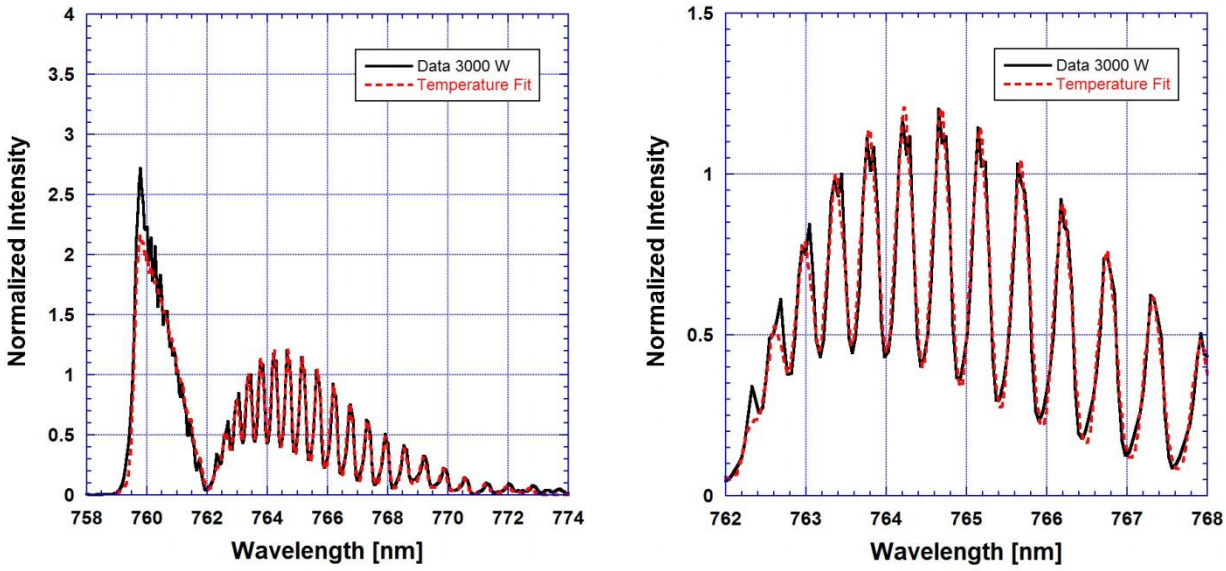

Figure 4.21. (a) O_2(b) spectrum at 3000W and temperature fit indicating a gas temperature of 572 K [O_2(b)_MTD method]. (b) Enhanced version of (a) showing the temperature fits to the P-branch. The flow rates were O_2:He:NO 45:150:0.26 mmol-s^{-1} and the discharge pressure was 50 Torr.

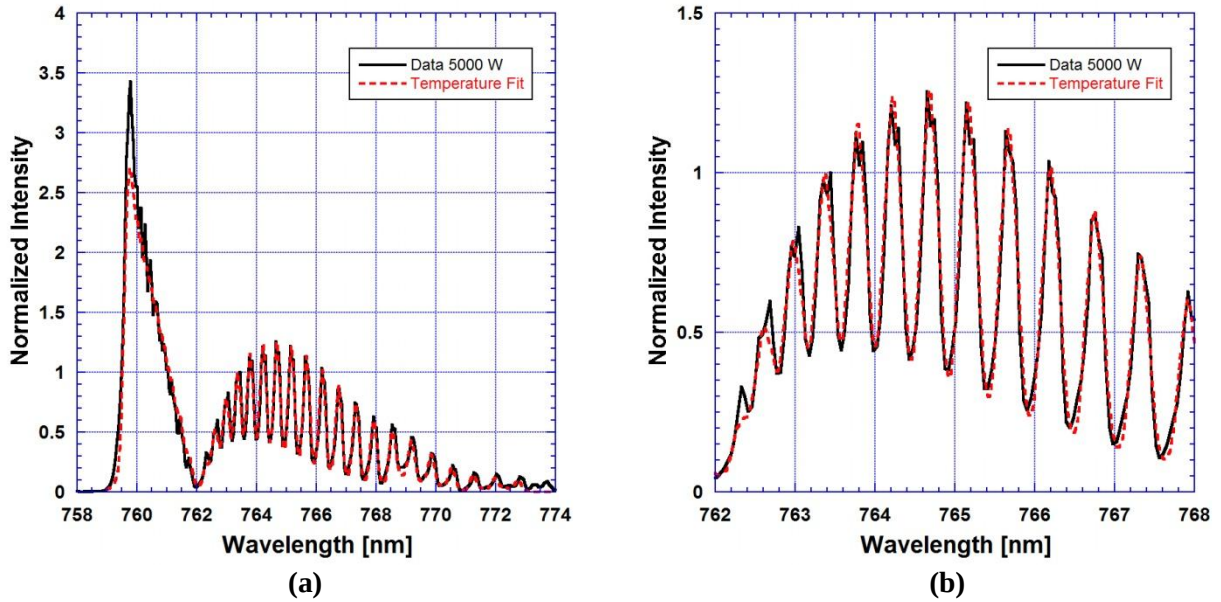

Figure 4.22. (a) O_2(b) spectrum at 5000W and temperature fit indicating a gas temperature of 644 K [O_2(b)_MTD method]. (b) Enhanced version of (a) showing the temperature fits to the P-branch. The flow rates were O_2:He:NO 45:150:0.26 mmol-s^{-1} and the discharge pressure was 50 Torr.

A few general conclusions can be made from the data presented above. First, the temperatures calculated from the O_2(b) spectra follow the expected trend that increasing the discharge power increases the gas temperature. Second, the temperature fits accurately track the behavior of the O_2(b) spectra along both the R and P branches even though only the P-branch peaks and valleys are used for matching purposes. The temperature fits exhibit the same R-branch behavior as the data shown in Figure 4.18(b).

Another interesting point is that the gas temperature at the discharge exit can vary from 425 K to 575 K (difference of 150 K) when discharge powers are changed from 1000 W to 4000 W. This temperature range can be compared to the data in Table 4.4 where laser cavity temperatures were measured versus discharge power. Table 4.4 shows that calculated O_2(b) temperatures in the laser cavity varied from 90 K to 105 K (difference of 15 K) at discharge powers of 1000 W and 4000 W. When looking at O_2(a) temperatures in Table 4.4, the cavity temperature difference is only 6 K when discharge power changes from 1000 W to 4000 W. These data indicate that gas temperature in the cavity stays fairly constant even as the gas temperatures leaving the discharge are increasing by huge margins. This seems to suggest that flow cooling methods downstream from the discharge such as injection of cold nitrogen gas and supersonic expansion are the main drivers which determine laser cavity temperature. This subject will be discussed more in Section 5 of this thesis.

4.6 Heat Exchanger Analysis Using O_2(a) and O_2(b)

An additional use of the O_2(a) and O_2(b) temperature diagnostics is to analyze the performance of different heat exchanger designs. Two different heat exchangers (denoted as HEX-1 and HEX-2) were used in the Cav6 laser configuration. For HEX-1, a solid block of aluminum had numerous holes drilled through in the flow direction. HEX-2 was designed so that the gas would pass through an array of tubes which carried the coolant. Detailed descriptions and photographs of HEX-1 and HEX-2 can be found in Section 2 of this thesis.

Three parameters were measured on the downstream side of the heat exchanger in order to analyze heat exchanger performance: flow temperature, O_2(a) yields, and O atom yields. As previously discussed in Section 3, flow temperature is important due to the equilibrium of the laser pumping reaction. Equally as important as the flow temperature is the O_2(a) yield at the heat exchanger exit. Therefore, the heat exchanger must maximize gas temperature reduction

while maintaining high $O_2(a)$ yields. The O atom yields also must be monitored at the heat exchanger exit. High O atom yields cause quenching of the I* state and decrease laser performance. However, O atom yields cannot be too low at the heat exchanger exit since O atoms also play a role in dissociating I_2.

For the heat exchanger experiments, the 6-tube discharge and either HEX-1 or HEX-2 were attached to the Cav6 laser hardware. The Cav6 hardware has built-in diagnostics ports immediately downstream from the heat exchanger. The diagnostics ports are located on both sides of the Cav6 hardware, allowing OMA and PMT measurements at the same location. If PMT measurements are not needed, the CCD fiber can be placed in the second diagnostics port so that $O_2(a)$ and $O_2(b)$ measurements can be made. Figure 4.23 shows a schematic and photograph of the experimental setup used to study the heat exchangers.

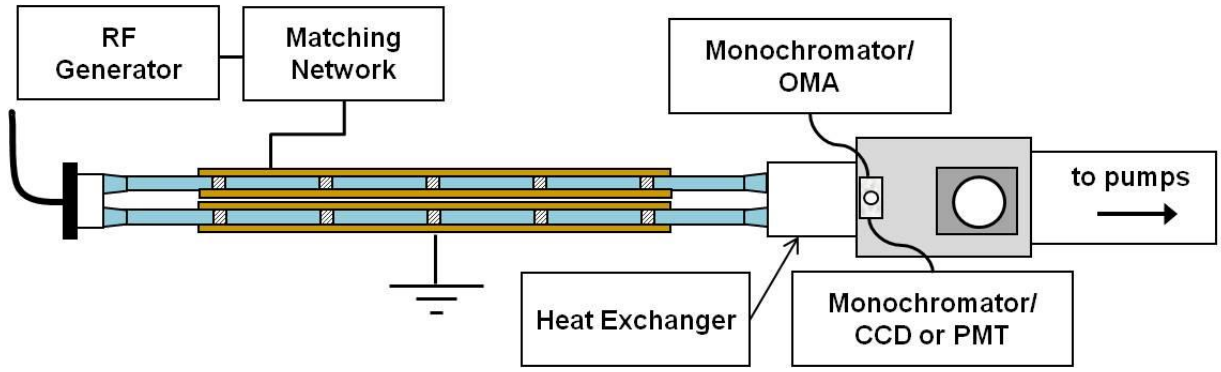

(a)

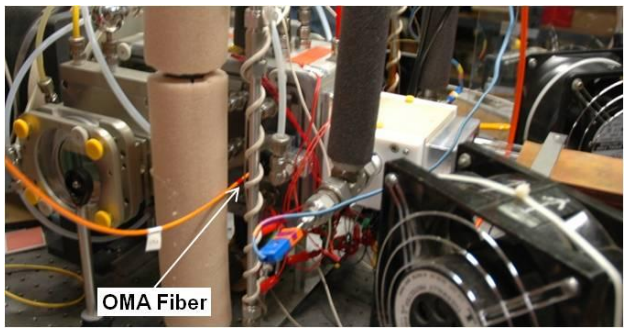

(b)

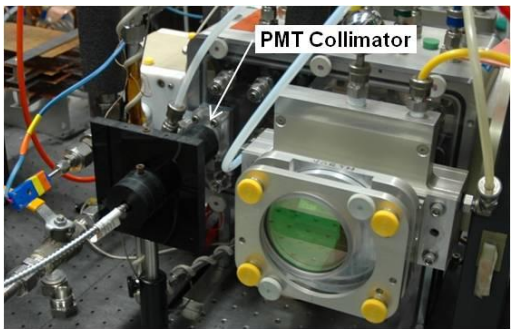

(c)

Figure 4.23. (a) Schematic of the experimental setup used to measure temperature, $O_2(a)$ yield, and O atom concentration on the downstream side of the heat exchanger. There are viewing ports on both sides of the Cav6 hardware that allow the OMA, CCD, and PMT optical diagnostics to take optical measurements after the heat exchanger and before the nozzle. Photographs showing (a) the OMA fiber and (b) the PMT collimator in the diagnostics duct downstream from the heat exchanger. The flow is from left to right in (a) and (c) and right to left in (b).

To compare HEX-1 and HEX-2, the flow temperature, $O_2(a)$ yield, and O atom yields downstream from the heat exchangers was measured versus discharge operating time. The discharge power, discharge pressure, and gas flow rates were held constant at 5000 W, 46 Torr, and O_2:He:NO 45:150:0.6 mmol-s^{-1}, respectively. These flow conditions were chosen based on flow conditions giving the best laser power measurements in past experiments [4.6]. Syltherm XLT heat transfer fluid was pumped through HEX-1 at 4 GPM US and -25°C and HEX-2 at 5 GPM US and -30°C. Ideally, the coolant flow rate and temperature would be the same to best compare HEX-1 and HEX-2. However, out of all the data taken with the heat exchangers, these coolant conditions were the most similar. As in the experiments described in Section 4.3, the discharge was pre-matched prior to taking any measurements. After being matched, the discharge was turned off and the flow tubes were allowed to cool. Then the pre-matched discharge was turned on and $O_2(a)$ and PMT measurements were made about every 60 seconds for HEX-1 and about every 100 seconds for HEX-2.

Figure 4.24 shows the gas temperatures calculated using the $O_2(a)$_MTD method, $O_2(a)$ yield, and O atom yields versus discharge operating time for HEX-1 and HEX-2. The first important point is that HEX-1 resulted in lower gas temperatures (by about 40 K) on the downstream side. However, the $O_2(a)$ yields were between one and one-half percent better with HEX-2. Figure 4.24 also shows that O atom yields are higher downstream from HEX-2. Unfortunately, these results do not provide a quick answer as to which heat exchanger would perform better in the EOIL system. In terms of gas temperature reduction, HEX-1 provides the best performance. However, the added gas temperature reduction comes at the cost of lower $O_2(a)$ yields. This results in the question: Downstream from the heat exchanger, are gas temperatures or $O_2(a)$ yields more important for laser performance?

To answer this question, gain was measured using HEX-1 and HEX-2. Gain measurements would determine if HEX-1, which gives lower gas temperatures and lower $O_2(a)$ yields, is better than HEX-2, which gives higher gas temperatures but higher $O_2(a)$ yields. There were no gain measurements using HEX-1 with Syltherm coolant at -25°C. The only available gain measurements with HEX-1 were made using water coolant at 0°C. In previous experiments with HEX-1, it had been shown that changing the coolant temperature from 0°C to -25°C did not affect the downstream gas temperature. For this reason, the gain measurements from HEX-1 with coolant at 0°C can be compared to gain measurements from HEX-2 with coolant at -30°C. For

both HEX-1 and HEX-2 experiments, the flow rates were O_2:He:NO 45:150:0.4 mmol-s^{-1}. Iodine and nitrogen gas were injected upstream of the nozzle at 39 mmol-s^{-1} and 70°C and 305 mmol-s^{-1} and -192°C, respectively. The 6-tube discharge was operated at 5000 W. The maximum gain was 0.264 %-cm^{-1} using HEX-1 and 0.285 %-cm^{-1} for HEX-2. The increased gain using HEX-2 reveals that the higher O_2(a) yields outweigh the colder gas temperatures downstream from the heat exchanger. This result will aid in future heat exchanger design.

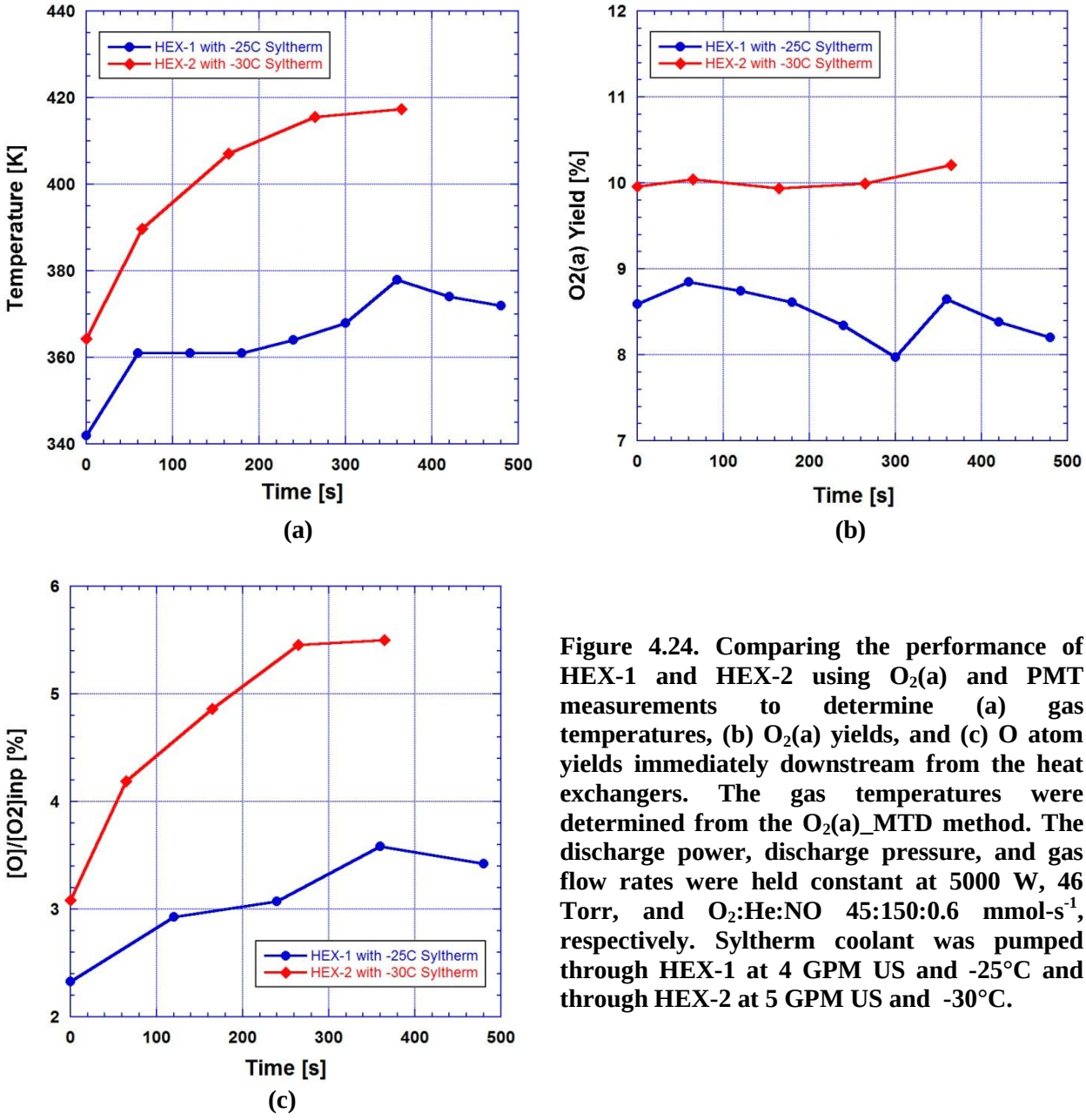

Figure 4.24. Comparing the performance of HEX-1 and HEX-2 using O_2(a) and PMT measurements to determine (a) gas temperatures, (b) O_2(a) yields, and (c) O atom yields immediately downstream from the heat exchangers. The gas temperatures were determined from the O_2(a)_MTD method. The discharge power, discharge pressure, and gas flow rates were held constant at 5000 W, 46 Torr, and O_2:He:NO 45:150:0.6 mmol-s^{-1}, respectively. Sytherm coolant was pumped through HEX-1 at 4 GPM US and -25°C and through HEX-2 at 5 GPM US and -30°C.

In addition to comparing the performance of HEX-1 and HEX-2, the effect of coolant temperature on heat exchanger performance was analyzed. For this experiment, HEX-2 was used in the same setup shown in Figure 4.23. The Syltherm flow rate was constant at 5 GPM US and the temperature varied from 15°C to -30°C. The discharge power, pressure, and flow rates were the same as those provided in Figure 4.24. Figure 4.25 shows the effect of coolant temperature on gas temperature, $O_2(a)$ yield, and O atom yield immediately downstream from the heat exchanger.

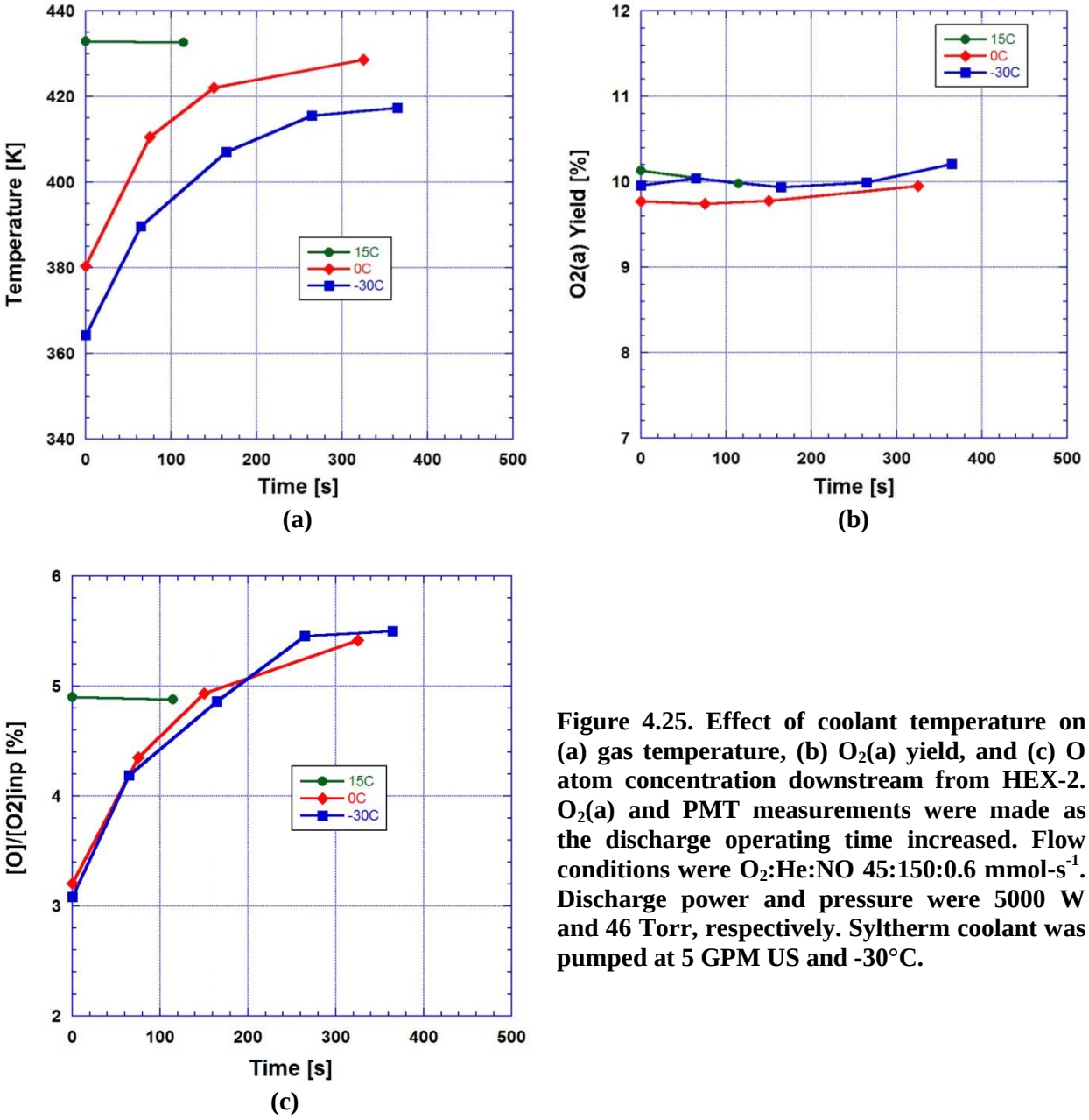

Figure 4.25. Effect of coolant temperature on (a) gas temperature, (b) $O_2(a)$ yield, and (c) O atom concentration downstream from HEX-2. $O_2(a)$ and PMT measurements were made as the discharge operating time increased. Flow conditions were O_2:He:NO 45:150:0.6 mmol-s^{-1}. Discharge power and pressure were 5000 W and 46 Torr, respectively. Syltherm coolant was pumped at 5 GPM US and -30°C.

Figure 4.25(a) shows that decreasing the coolant temperature in HEX-2 results in substantial temperature differences downstream from the heat exchanger. As previously mentioned, the coolant temperature was varied in HEX-1 from 25°C (tap water) to 0°C (ice water) to -25°C (Syltherm). Contrary to the results seen in Figure 4.25(a), changing the coolant temperature in HEX-1 from 0°C to -25°C did not result in noticeable changes in downstream temperature. This leads to the question: Why does lowering the coolant temperature in HEX-1 from 0°C to -25°C not affect the downstream temperature, but changing the coolant temperature in HEX-2 from 15°C to 0°C to -30°C results in increasingly lower downstream temperatures?

The answer lies in the designs of the two heat exchangers. The HEX-1 design has a large surface area which allows heat from the gas to transfer into the heat exchanger metal. However, there is also a lot more material (metal) between the coolant channels and hot gas ducts. The amount of material between the coolant channels and gas ducts limit the temperature drop that can be attained. There is a lower bound on HEX-1 where decreasing the coolant temperature does not decrease gas temperature. On the other hand, the HEX-2 design has thin-walled tubes carrying the coolant, allowing heat to easily pass between the metal and into the coolant. For this reason, decreasing the coolant temperature causes increased heat conduction between the gas and coolant tubes. However, the surface area seen by the gas is also less in HEX-2. As a result, there is less material to absorb the heat from the gas, leading the higher gas temperatures than HEX-1. Figure 4.25 also shows that decreasing the coolant temperature does not affect the $O_2(a)$ or O atom yield. This is a promising result because it shows that the gas temperature can be reduced by lowering the coolant temperature without negatively affecting $O_2(a)$ or O atom yields.

A final heat exchanger experiment was conducted so that temperature measurements downstream from the heat exchangers could be calculated using all four temperature determination methods. The experimental setup was almost the exact same as the setup shown in Figure 4.23. The one change in the setup was that the CCD fiber was placed at the location that had been used for PMT measurements. The flow rates were O_2:He:NO 45:150:0.6 mmol-s^{-1}. The discharge power and pressure were 5000 W and 46 Torr, respectively. Syltherm coolant was pumped through HEX-2 at 5 GPM US and -30°C. $O_2(a)$ and $O_2(b)$ measurements were made every 100 seconds for approximately 400 seconds. Figure 4.26 shows the calculated gas temperatures versus discharge operating time.

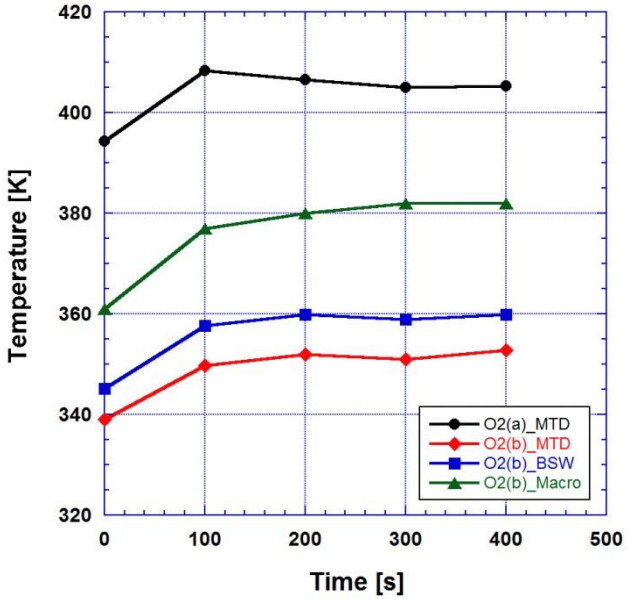

Figure 4.26. Gas temperature versus discharge operating time immediately downstream from the heat exchanger. Flow conditions were O_2:He:NO 45:150:0.6 mmol-s^{-1}. Discharge power and pressure were 5000 W and 46 Torr, respectively. Syltherm coolant was pumped through HEX-2 at 5 GPM US and -30°C. Four methods were used to determine the gas temperature: O_2(a)_MTD, O_2(b)_MTD, O_2(b)_BSW, and O_2(b)_Macro.

As seen in other experiments, the four temperature methods result in four different calculated gas temperatures. The O_2(b) temperature determination methods vary between 20 K and 30 K during the entire experiment. The only promising result is that the temperature methods exhibit the same behavior and seem to capture a steady-state temperature on the downstream side of the heat exchanger. The most likely reasons for the discrepancy between O_2(a) and O_2(b) temperatures is the NO "air afterglow" and the decreased signal-to-noise ratio on the downstream side of the heat exchanger.

In the next section of this thesis, the experimental spectra and theoretical matching procedure will be looked at in more detail. A number of hypotheses will be presented in hopes of explaining the discrepancy between temperatures calculated using the different methods. In particular, O_2(a) and O_2(b) measurements made versus discharge operating time (Section 4.3) and data from the heat exchanger experiments (Section 4.6) will be further analyzed.

4.7 References

[4.1] King, D.M., Carroll, D.L., Verdeyen, J.T., Laystrom, J.K., Benavides, G.F., Palla, A.D., Zimmerman, J.W., Woodard, B.S., and Solomon, W.C., Power Enhancement of the Hybrid ElectricOIL Laser, *AIAA 37th Plasma Dynamics and Lasers Conference*, 5-8 June 2006, AIAA Paper 2006-3756.

[4.2] Carroll, D.L., Verdeyen, J.T., King, D.M., Benavides, G.F., Woodard, B.S., Kittell, K., Solomon, W.C., Rawlins, W.T., Davis, S.J., and Kessler, W.J., Preliminary yield measurements in the ElectriCOIL system, *Proceedings of the Gas and Chemical Lasers and Applications IV Conference*, 26 January 2004, *SPIE* Vol. 5334, pp. 79-87 (2004).

[4.3] Groth, W., Kley, D., and Schurath, U., Rate Constant for the Infrared Emission of the NO($C^2\Pi \rightarrow A^2\Sigma^+$) Transition, *J. Quant. Spectrosc. Radiat. Transfer*, Vol. 11, pp. 1475-1480 (1971).

[4.4] Rawlins, W.T., Lee, S., Galbally-Kinney, K.L., Kessler, W.J., Hicks, A.J., Konen, I.M., Plumb, E.P., and Davis, S.J., Optically-Based Diagnostics for Gas-Phase Laser Development, *XVIII International Symposium on Gas Flow and Chemical Lasers and High Power Lasers*, August 2010.

[4.5] Woodard, B.S., Zimmerman, J.W., Verdeyen, J.T., Carroll, D.L., Field, T.H., Benavides, G.F., Palla, A.D., and Solomon, W.C., Improved production of $O_2(a^1\Delta)$ in transverse radio-frequency discharges, *HPLA 2008 Conference*, 21-24 April 2008, *SPIE* Vol. 7005, pp. 70051L-1-9 (2008).

[4.6] Zimmerman, J.W., Benavides, G.F., Woodard, B.S., Day, M.T., Carroll, D.L., Palla, A.D., Verdeyen, J.T., and Solomon, W.C., Electric Oxygen-Iodine Laser Performance Enhancement using Larger Discharge and Resonator Mode Volumes, *AIAA 41st Plasmadynamics and Lasers Conference*, 28 June - 1 July 2010, AIAA Paper 2010-5038.

5. Concerns with O_2(a) and O_2(b) Temperature Calculations

The previous section presented the results of using the O_2(a) and O_2(b) temperature diagnostics to analyze data. For the most part, each of the four temperature diagnostics matches expected trends in the data (i.e. as the discharge power increases or the discharge operating time increases, the calculated gas temperature increases). However, the four temperature determination methods did not always calculate similar gas temperatures. Also, there were cases where the four methods calculated dramatically different temperatures. This section attempts to explain the discrepancy among the four temperature methods. In the previous section, temperature differences were attributed to the NO "air afterglow." This section will show how the "air afterglow" affects temperature calculations. In addition to the "air afterglow," issues with forming the theoretical spectra used in the matching procedure may be affecting temperature calculations. In particular, the lineshape function may be leading to errors between the temperature determination methods. A detailed analysis of the lineshape function will be presented and discussed.

5.1 Temperatures Downstream from Heat Exchangers

In Section 4.6, the performance of different heat exchangers was analyzed. This was done by comparing gas temperatures, O_2(a) yields, and O atom yields immediately downstream from the heat exchangers. Since O_2(a) and O atom yields were desired, the OMA and PMT were placed in the two diagnostic ducts downstream from the heat exchangers. CCD measurements could not be made since the only two diagnostics ducts were occupied by the OMA and PMT. Since O_2(b) measurements were not made, the O_2(a)_MTD method was used to determine gas temperatures downstream from both heat exchangers. Later in Section 4.6, data were presented where the PMT was removed and the CCD was placed in the diagnostics duct. This allowed gas temperature calculations using all four temperature methods. While each method exhibited the expected behavior of gas temperature increasing with discharge operating time (Figure 4.26), none of the methods calculated similar gas temperatures. This subsection will analyze the experimental spectra and temperature fit procedure to determine why the methods are inconsistent.

To find out what is causing the temperature differences among the four methods, the spectra used in the calculations were analyzed. Figure 5.1 shows raw and corrected O_2(a) and

O_2(b) measurements downstream from the heat exchanger. These spectra were used to obtain the last data points (at 400 seconds) in Figure 4.26 in Section 4.6. The calculated temperatures were 405 K from O_2(a)_MTD and 353 K from O_2(b)_MTD.

As described in Section 4, the "air afterglow" causes a ramped baseline that elevates and rotates the spectra. At first glance, the procedure used to correct the linear baseline seems to be performing well since the tails of the corrected OMA measurement (near 1190 nm and 1300 nm) have count values near zero. Problems become more evident when the corrected spectrum is observed more closely. The procedure used to correct the baseline does not zero the corrected O_2(a) spectra at the lower wavelength side (around 1250 nm). There is a clear gap between the bottom of the measured signal and the zero count value. The fact that the linear baseline corrects the OMA measurement at 1190 nm and 1300 nm but not at the tails of the O_2(a) spectrum confirms that a nonlinear "air afterglow" can show up in some spectra. This is not saying that a linear baseline gives poor results for all spectra. In some instances, as in most plots shown in Section 4, a linear baseline performs well at zeroing the spectra. However, there is a clear problem with the linear baseline in the spectra shown in Figure 5.1.

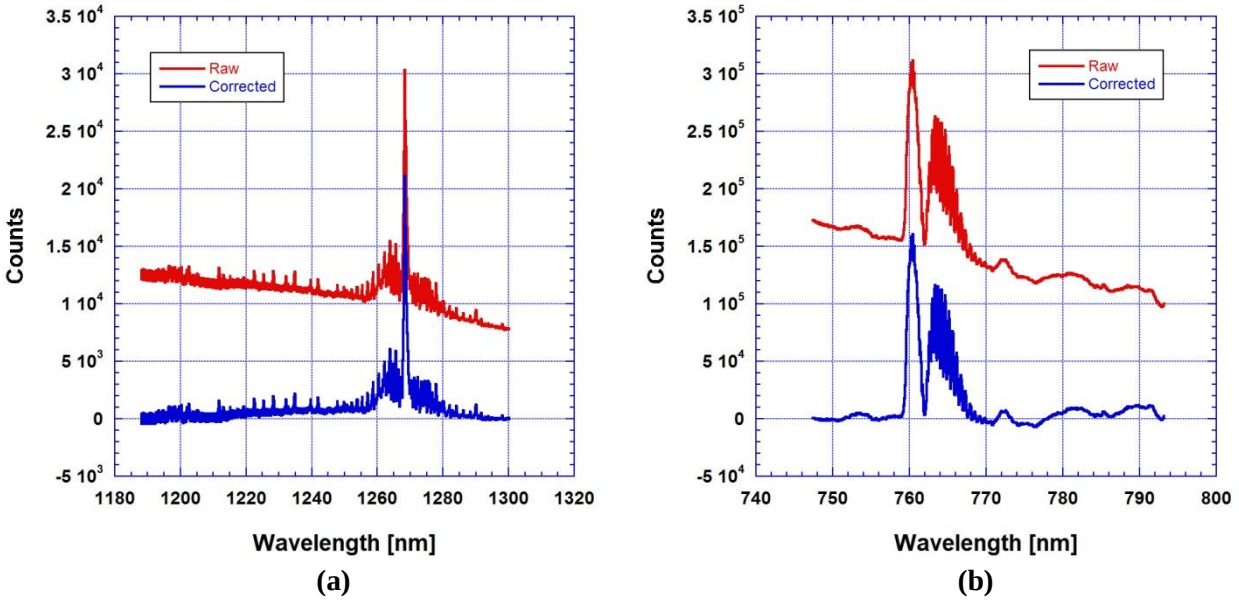

Figure 5.1. Raw and corrected (a) O_2(a) and (b) O_2(b) measurements made downstream from the heat exchanger. These plots show that applying a linear baseline does not always zero the emission tails. Flow conditions were O_2:He:NO 45:150:0.6 mmol-s^{-1}. Discharge power and pressure were 5000 W and 46 Torr, respectively. Syltherm coolant was pumped through HEX-2 at 5 GPM US and -30°C.

A similar baseline problem appears in the O_2(b) spectra. From looking at Figure 5.1(b), the linear baseline gives zero counts near the beginning (746 nm) and end (794 nm) of the CCD measurement. The linear baseline also results in a zero baseline at the lower wavelength tail of the O_2(b) emission (758 nm). However, the linear baseline does not provide a zero baseline at the higher wavelength tail (770 nm) of the O_2(b) emission.

Figure 5.2 illustrates the effects of a poor baseline on the O_2(a) temperature fit. Figure 5.2 shows the corrected O_2(a) spectra from Figure 5.1 plotted with the temperature fit. The most noticeable difference between the data and temperature fit is that the peak intensities around 1268 nm do not match well. Figure 5.2(b) takes a closer look at the peaks and valleys used in the temperature fit process. The temperature fit attempts to match the peaks and valleys from 1255 nm to 1268 nm. As expected, the temperature fit does not match the data on the tail end of the spectrum from 1255 nm to 1260 nm. Due to the poor baseline, all peaks (especially the ones from 1255 nm to 1260 nm) are elevated. In order to match the elevated intensities, the matching procedure must increase the theoretical spectrum temperature. This results in calculated temperatures that are higher than the actual gas temperature.

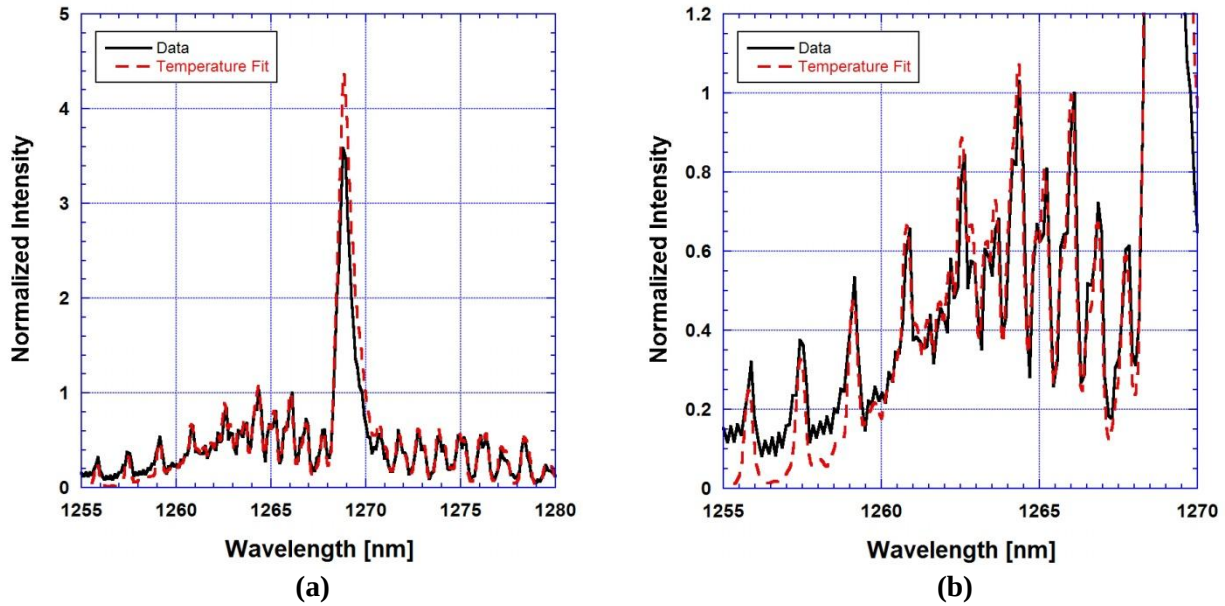

Figure 5.2. (a) Corrected O_2(a) spectrum from Figure 5.1 and temperature fit indicating a gas temperature of 405 K. (b) Enhanced version of (a) showing the temperature fit to the peaks and valleys used in the matching process. The poor baseline is evident from the large gap in intensity between the data and temperature fit from 1255 nm to 1260 nm. The poor baseline leads to elevated intensities and higher calculated gas temperatures.

Figure 5.3 shows the effect of a poor baseline on the O_2(b) temperature fit. Figure 5.3 shows the corrected O_2(b) spectrum from Figure 5.1. The data has a zero baseline near 758 nm, but the spectrum seems to shift downward at the higher wavelength side. At 770 nm, the spectrum has been shifted so far down that the normalized intensities become negative. For the most part, the temperature fit matches the peaks and valleys of the P-branch quite well. However, the downward shift lowers these peaks and valleys. In order to match the downward shifted peaks and valleys, the matching procedure is forced to decrease the theoretical spectrum temperature. This results in calculated temperatures that are lower than the actual flow temperature.

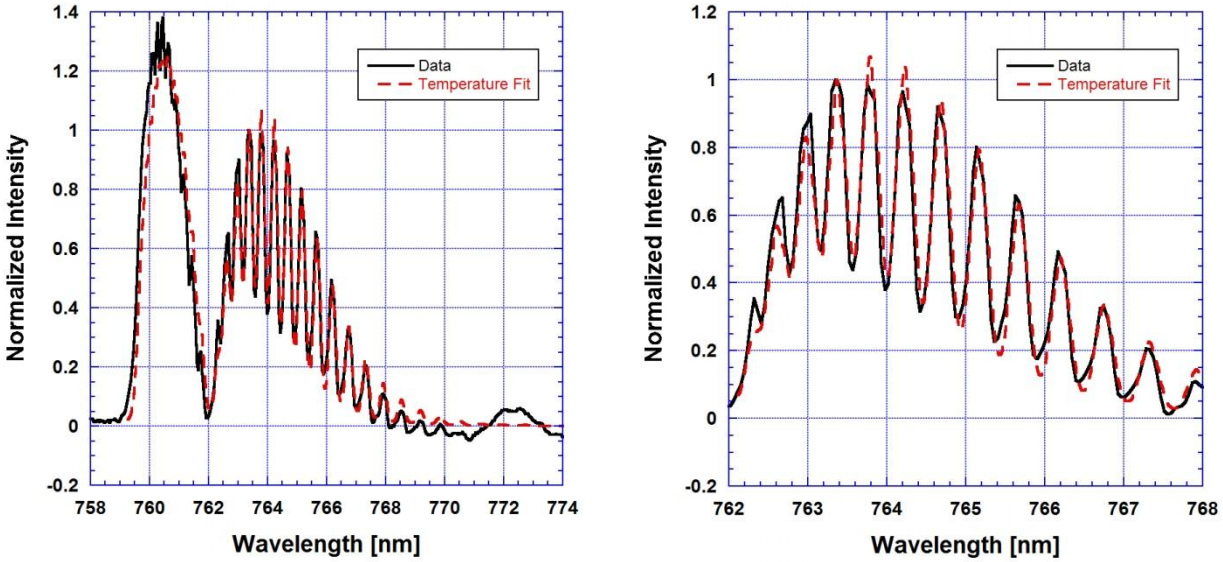

Figure 5.3. (a) Corrected O_2(b) spectrum from Figure 5.1 and temperature fit indicating a gas temperature of 353 K [O_2(b)_MTD method]. The baseline is at zero on the lower wavelength tail, but the baseline causes the higher wavelength tail to shift too far down and become negative. (b) Enhanced version of (a) showing the temperature fit to the peaks and valleys of the P-branch.

In addition to the spectra shown above, another data set is provided to further illustrate the effects of a poor baseline on the temperature calculation. Figure 5.4 shows raw and corrected O_2(a) and O_2(b) measurements downstream from the HEX-2 heat exchanger. These spectra were from a different heat exchanger experiment than the spectra shown above. The flow conditions were O_2:He:NO 45:150:0.9 mmol-s^{-1}. The discharge power and pressure were 6500 W and 50 Torr, respectively. This data set was chosen due to the large amount of "air afterglow" in the

spectra. The "air afterglow" is larger in Figure 5.4 than the data shown in Figures 5.1-5.3 due to the higher discharge power. Also, the calculated O_2(a) and O_2(b) temperatures were very different from one another [472 K for O_2(a)_MTD and 374 K for O_2(b)_MTD]. The lack of agreement between O_2(a) and O_2(b) temperatures shows that an increasing "air afterglow" effect causes larger differences in the temperature calculations.

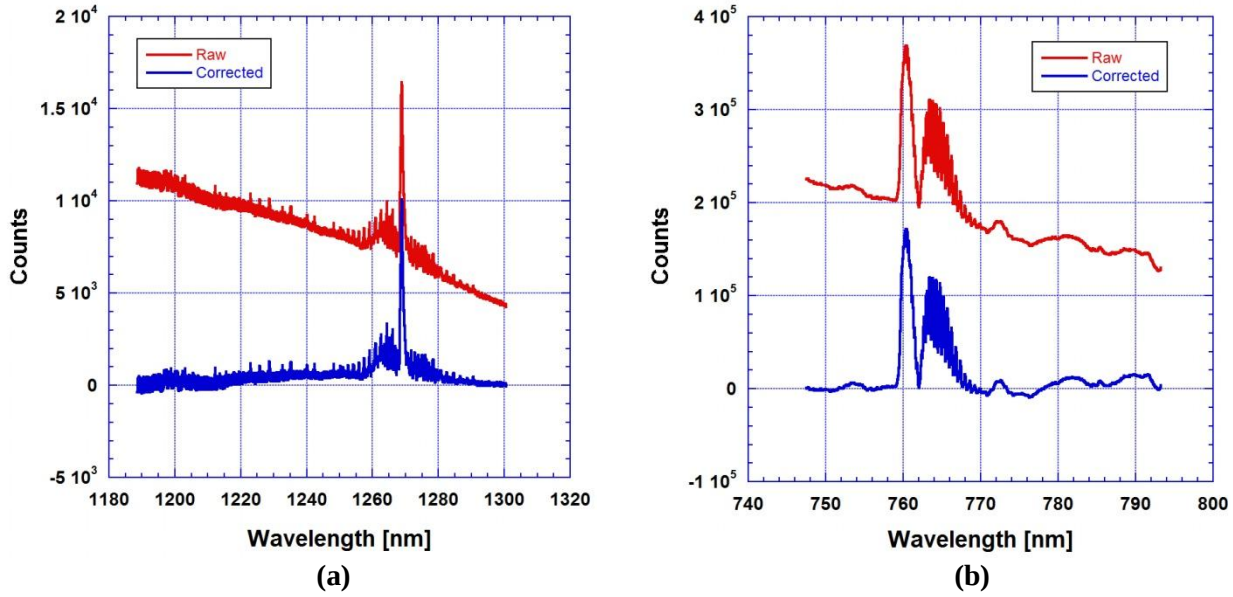

Figure 5.4. Raw and corrected (a) O_2(a) and (b) O_2(b) measurements made downstream from the heat exchanger. Flow conditions were O_2:He:NO 45:150:0.9 mmol-s^{-1}. Discharge power and pressure were 6500 W and 50 Torr, respectively. Syltherm coolant was pumped through HEX-2 at 5 GPM US and -30°C.

Figure 5.5 and 5.6 show the corrected O_2(a) and O_2(b) spectra from Figure 5.4 plotted with temperature fits. The same baseline problems are seen with these spectra as with the previous data set. The only difference is that the increased "air afterglow" affects the baseline intensity even more. For instance, the baseline shown in Figure 5.5(b) has a normalized intensity around 0.2 at 1255 nm. This can be compared to the baseline shown in Figure 5.2(b) which has a normalized intensity around 0.15 at 1255 nm. At first, this may not seem like a large difference. But small changes to the peak and valley intensities used to match the theoretical spectra to data can cause very large temperature differences. The poor baseline in Figure 5.5(b) is the main reason for a calculated O_2(a) temperature that is too high. A second indication of an unreasonably high temperature is the poor agreement between the data and temperature fit at the

peak intensity of 1268 nm. Another alarming observation involves the width of the noise in the O_2(a) spectrum. In Figure 5.4(a), the noise in the corrected spectrum from 1190 nm to 1250 nm has large amplitude. The noise amplitude is on the same order as the peaks and valleys used in temperature calculation. The large noise signal (amplitude of about 0.1 normalized intensity) can also be seen in Figure 5.5(b) between peaks at 1256 nm and 1257 nm. It is very hard to accurately match the spectra when the signal-to-noise ratio is so low. Also, the O_2(b) spectrum shown in Figure 5.6(a) has the same downward slope as the previous data shown in Figure 5.3(a). As described above, the downward slope leads to lower calculated O_2(b) temperatures.

The reasoning presented above provides some justification on why the O_2(a) and O_2(b) temperature methods are providing different temperature values downstream from the heat exchanger. The raw data have nonlinear "air afterglow" that cannot be properly corrected using the current linear method. For the O_2(a) spectra, the linear method does not zero the baseline on the lower wavelength side. This elevates the peaks and valleys used to calculate temperature. For the O_2(b) spectra, the linear method does not zero the baseline on the higher wavelength side. This lowers the peaks and valleys used to calculate temperature. Due to the poor baselines, the temperature fit procedure calculates higher O_2(a) temperatures and lower O_2(b) temperatures.

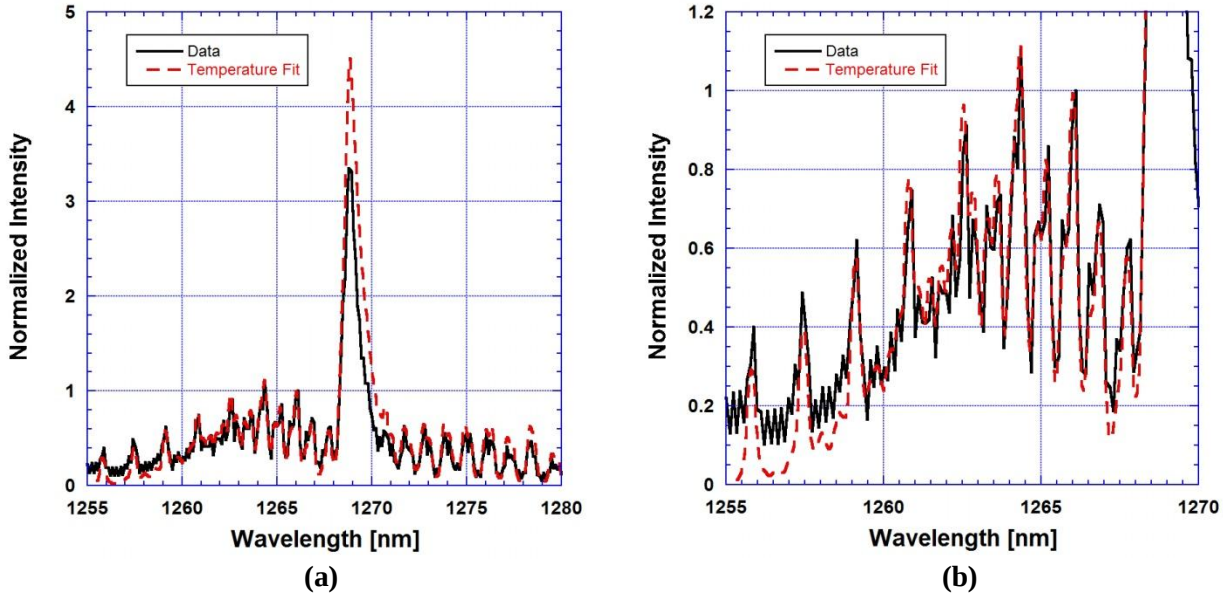

Figure 5.5. (a) Corrected O_2(a) spectrum from Figure 5.4 and temperature fit indicating a gas temperature of 472 K. (b) Enhanced version of (a) showing the temperature fit to the peaks and valleys used in the matching process.

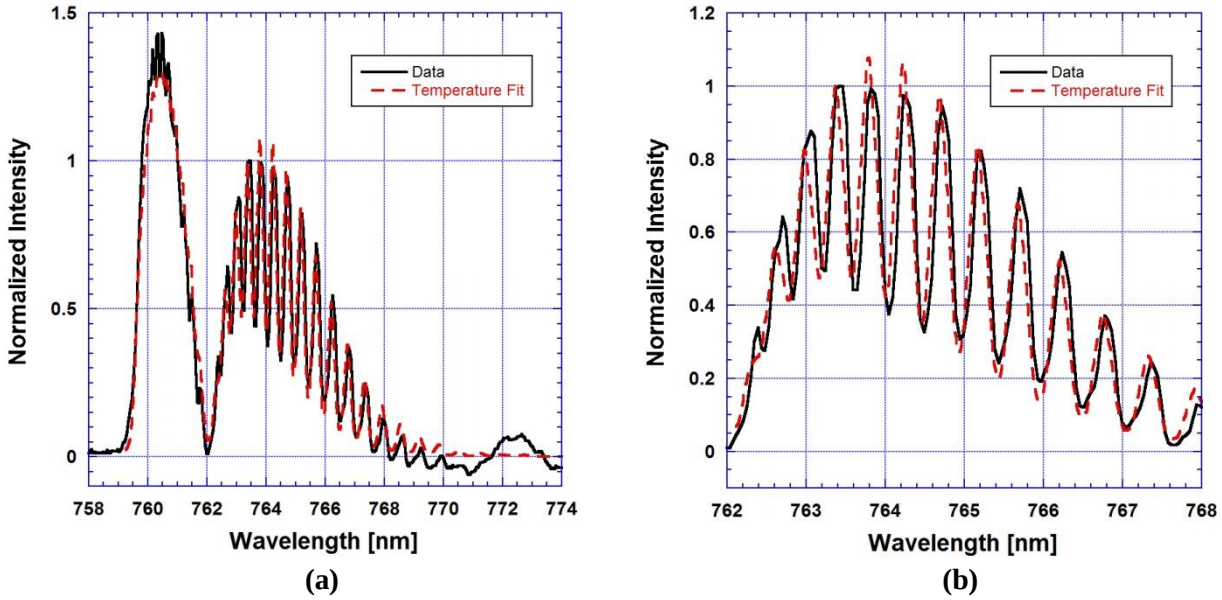

Figure 5.6. (a) Corrected O_2(b) spectrum from Figure 5.4 and temperature fit indicating a gas temperature of 374 K [O_2(b)_MTD method]. (b) Enhanced version of (a) showing the temperature fit to the peaks and valleys of the P-branch.

Since a linear correction for "air afterglow" is not providing the best results in the heat exchanger data, a different method of correcting the experimental spectra needs to be used. Currently, a new method for correcting the data is being studied. This method uses a higher-order polynomial to make corrections to the "air afterglow." The higher-order polynomial method may be necessary to correct the nonlinear data seen downstream from the heat exchanger. Since the higher-order polynomial method is still being developed, this thesis will not present any data that uses this method to correct the "air afterglow."

The analysis above presents reasons for the temperature difference between the O_2(a) and O_2(b) spectra. However, one question still needs to be answered: Why do the O_2(b) temperature methods calculate different temperatures? This question arises from the data shown in Figure 4.26 in Section 4.6 where the three O_2(b) methods calculate considerably different temperatures. There are a few reasons why the three O_2(b) methods calculate different temperatures. First, the O_2(b) methods differ by the way in which the "air afterglow" effect is corrected. In O_2(b)_MTD, the "air afterglow" is subtracted the same way as O_2(a)_MTD (presented in Section 4.1). The O_2(b)_BSW and O_2(b)_Macro methods use a slightly different procedure than O_2(b)_MTD for correcting the "air afterglow." This would account for subtle temperature differences between O_2(b)_MTD and O_2(b)_BSW.

The nonlinear slope from the "air afterglow" also explains why O_2(b)_BSW and O_2(b)_MTD give different calculated temperatures than O_2(b)_Macro. In O_2(b)_Macro, the ratio of only two peaks is used to calculate temperature. Since the peaks used in this method are close to one another, the baseline procedure does not affect the relative intensity ratio between these two peaks. On the other hand, O_2(b)_BSW and O_2(b)_MTD use more peaks and valleys to calculate temperature. These methods are using peaks and valleys on the lower wavelength side (where the baseline is good) and the higher wavelength side (where the poor baseline causes peaks and valleys to slope downward). The peaks and valleys on the higher wavelength side of the data are more influenced by the poor baseline procedure and cause the matching procedure to favor lower temperatures. This may explain why the O_2(b)_MTD and O_2(b)_BSW methods usually calculate lower gas temperatures than the O_2(b)_Macro method.

5.2 Temperatures versus Discharge Operating Time

The heat exchanger studies were not the only experiments where the O_2(a) and O_2(b) temperatures were not in agreement. In Section 4.3, an experiment was conducted where the discharge power was held constant and the gas temperature was measured versus discharge operating time. These results (Figures 4.10, 4.12, and 4.14) showed that calculated O_2(a) and O_2(b) temperatures varied. The results also showed unusual fluctuations where gas temperatures spiked upward or downward by as much as 50 K between data points spaced a few seconds apart. This behavior was unusual since the gas temperature was expected to increase slightly or remain relatively consistent between data points. The following subsection analyzes the O_2(a) and O_2(b) spectra from these experiments to understand why the discrepancies and random temperature fluctuations occurred.

Figure 5.7 shows raw and corrected O_2(a) and O_2(b) measurements. The flow conditions were O_2:He:NO 10:33:0 mmol-s^{-1}. Discharge power and pressure were 1000 W and 20 Torr, respectively. The spectra shown in Figure 5.7 were used to calculate temperatures [505 K for O_2(a)_MTD and 462 K for O_2(b)_MTD] in Figure 4.12(b) at a discharge operating time of 170 seconds. Since NO was not added, there is no "air afterglow" and the raw and corrected spectra are nearly on top of one another. The one downside of the spectra shown in Figure 5.7 is that the signal-to-noise ratio is low due to the low flow rates and discharge power. The low signal-to-noise ratio allows small discrepancies along the spectral tails to more easily influence the

baseline. In Figure 5.7(a), numerous small peaks can be seen from 1180 nm to 1250 nm. The magnitudes of these peaks are on the order of the peak intensities used to match the theoretical and experimental spectra. It is not known whether these small peaks are emissions from other excited states or just part of the background noise. It is possible that more of these small peaks are present under the O_2(a) spectrum. Any additional emissions under the O_2(a) spectrum would elevate the peaks and valleys used in the temperature fit process and lead to higher calculated temperatures.

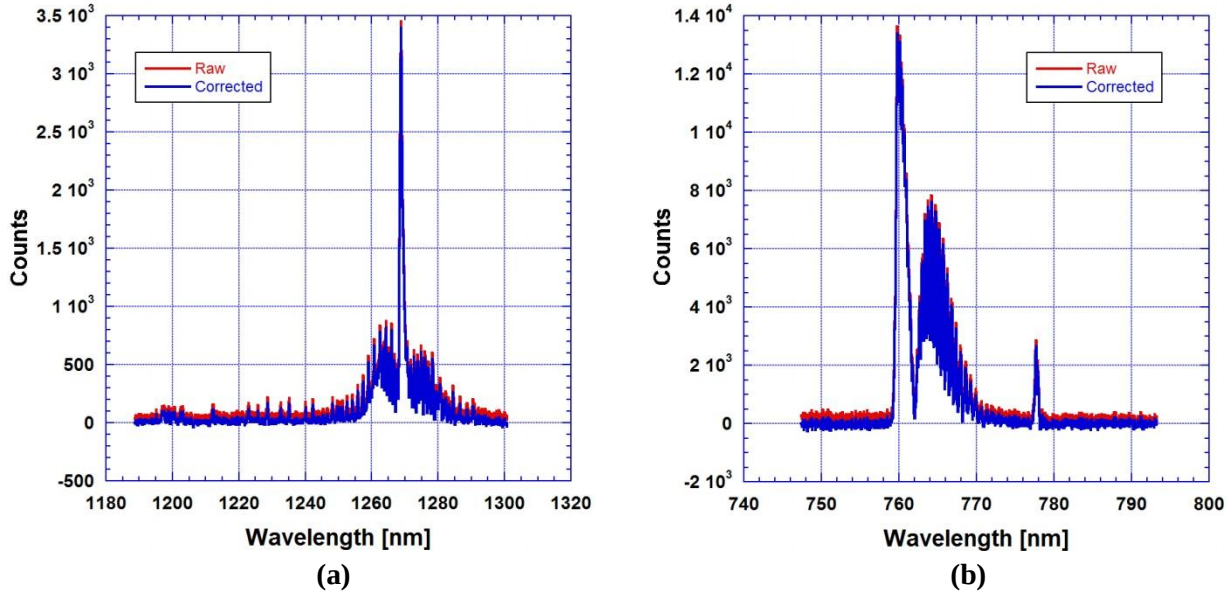

Figure 5.7. Raw and corrected (a) O_2(a) and (b) O_2(b) measurements. Flow conditions were O_2:He:NO 10:33:0 mmol-s^{-1}. Discharge power and pressure were 1000 W and 20 Torr, respectively.

Figures 5.8 and 5.9 take a closer look at the temperature fits to the corrected O_2(a) and O_2(b) spectra from Figure 5.7. In Figure 5.8(b), the temperature fit seems to be matching the peaks and valleys well. The only noticeable problem is that the data still do not have a zero baseline at 1255 nm. On the other hand, the peak normalized intensities at 1268 nm for the data and temperature fit are in agreement. In Figure 5.9, the O_2(b) temperature fit also seems to be matching the data well. In Figure 5.9(a), the O_2(b) spectrum does not have the same downward slope observed in plots with extensive "air afterglow." The only downfall with the O_2(b) temperature fit is that it does not do a good job matching the peak intensities and behavior of the R-branch (from 759 nm to 761 nm).

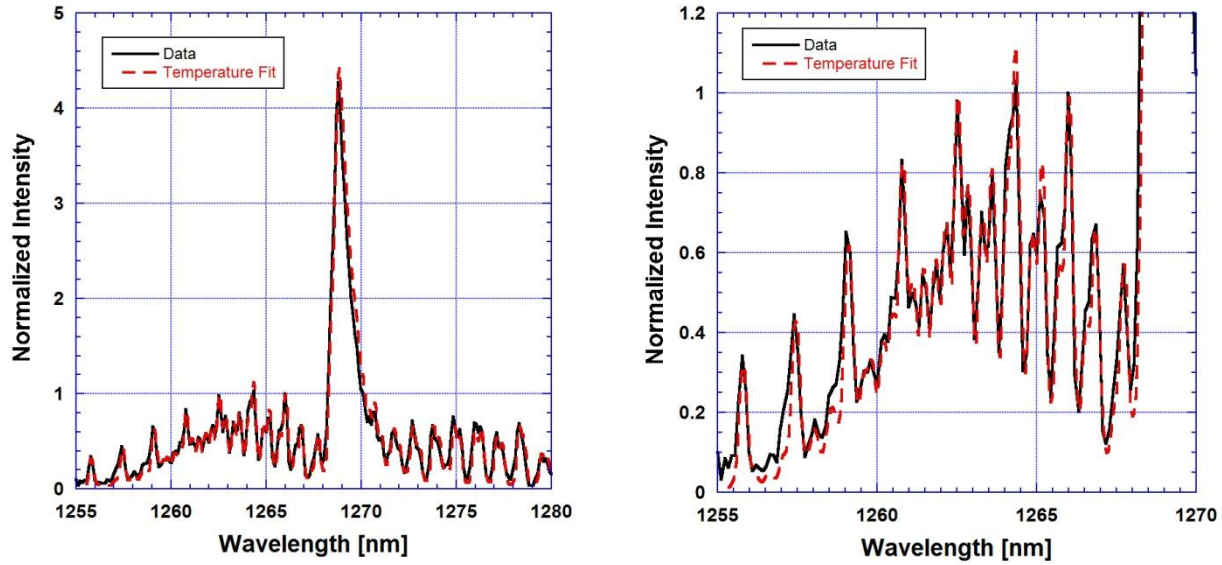

Figure 5.8. (a) Corrected O_2(a) spectrum from Figure 5.7 and temperature fit indicating a gas temperature of 505 K. (b) Enhanced version of (a) showing the temperature fit to the peaks and valleys used in the matching process.

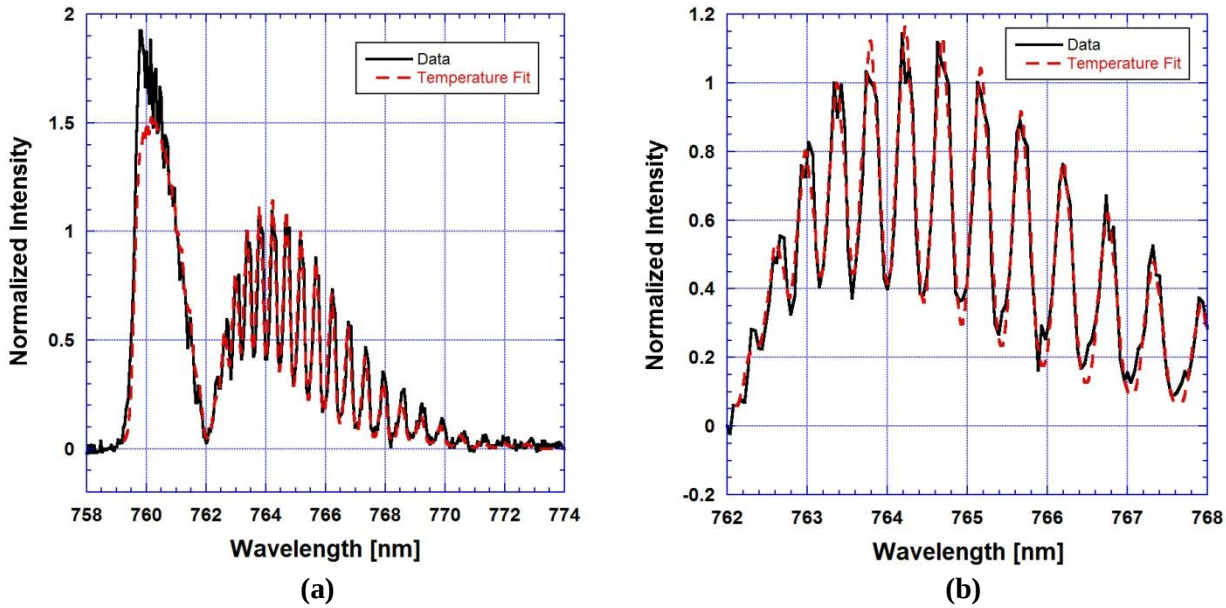

Figure 5.9. (a) Corrected O_2(b) spectrum from Figure 5.7 and temperature fit indicating a gas temperature of 462 K [O_2(b)_MTD method]. (b) Enhanced version of (a) showing the temperature fit to the peaks and valleys of the P-branch.

Additionally, the same experiment described above was conducted with NO in the primary flow. Figure 5.10 shows raw and corrected O_2(a) and O_2(b) measurements. The flow conditions were O_2:He:NO 10:33:0.16 mmol-s^{-1}. Discharge power and pressure were 1000 W and 20 Torr, respectively. The spectra shown in Figure 5.10 were used to calculate temperatures [525 K O_2(a)_MTD and 493 K O_2(b)_MTD] in Figure 4.12(a) at a discharge operating time of 170 seconds. Unlike the spectra shown in Figure 5.7, the NO "air afterglow" affects the spectra. As with the spectra shown in Figure 5.7, the signal-to-noise ratio is low. For the O_2(a) spectrum, a few small emissions can be seen in the noise from 1220 nm to 1250 nm.

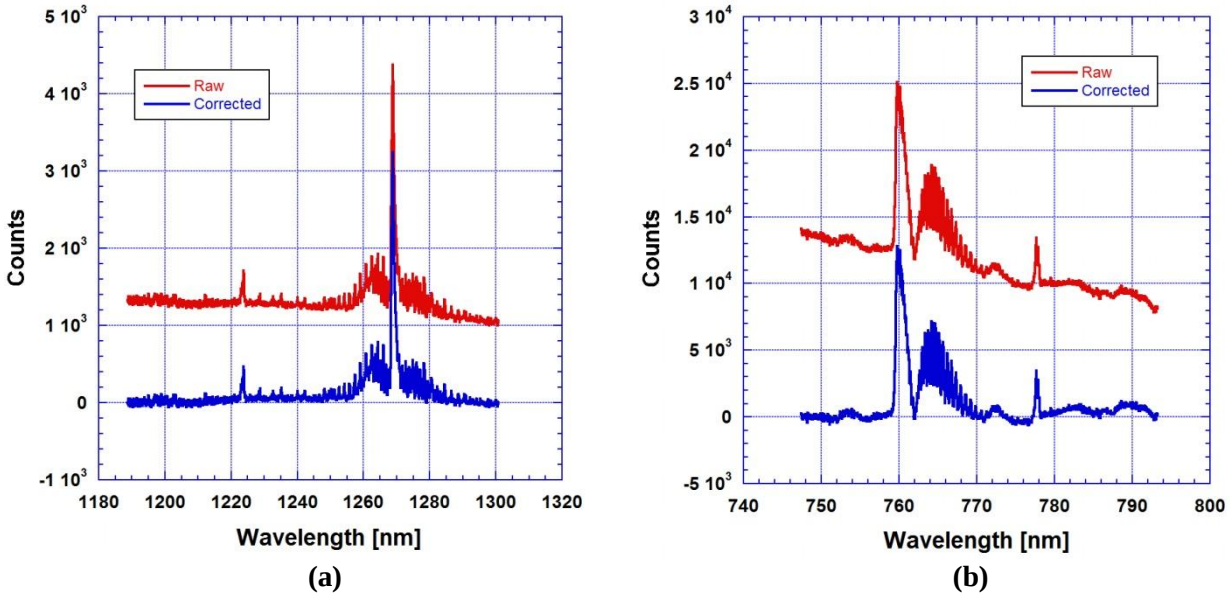

Figure 5.10. Raw and corrected (a) O_2(a) and (b) O_2(b) measurements. Flow conditions were O_2:He:NO 10:33:016 mmol-s^{-1}. Discharge power and pressure were 1000 W and 20 Torr.

Figures 5.11 and 5.12 look at the temperature fits to the data with NO. The corrected O_2(a) spectrum shown in Figure 5.11 looks very similar to the data in Figure 5.9 where NO was not present. As expected, the baseline to the data at 1255 nm is elevated. However, the baseline elevation is very similar to the case without NO. This is a puzzling result since the case without NO was expected to give a baseline closer to zero than the case with NO. The O_2(b) spectrum shown in Figure 5.12 also has the slight downward tilt seen in previous plots.

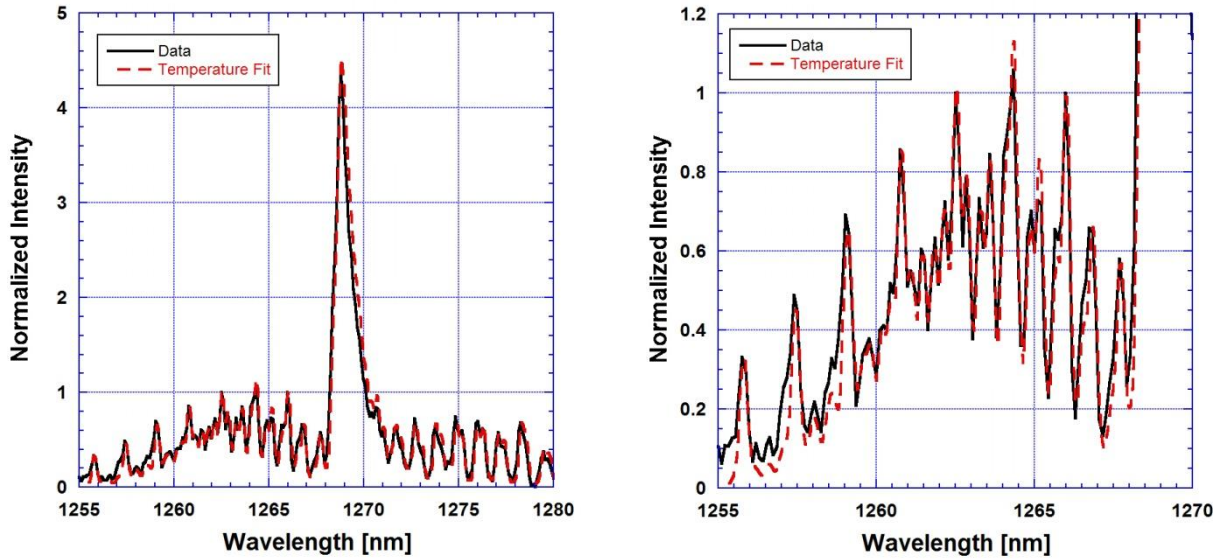

Figure 5.11. (a) Corrected O_2(a) spectrum from Figure 5.10 and temperature fit indicating a gas temperature of 525 K. (b) Enhanced version of (a) showing the temperature fit to the peaks and valleys used in the matching process.

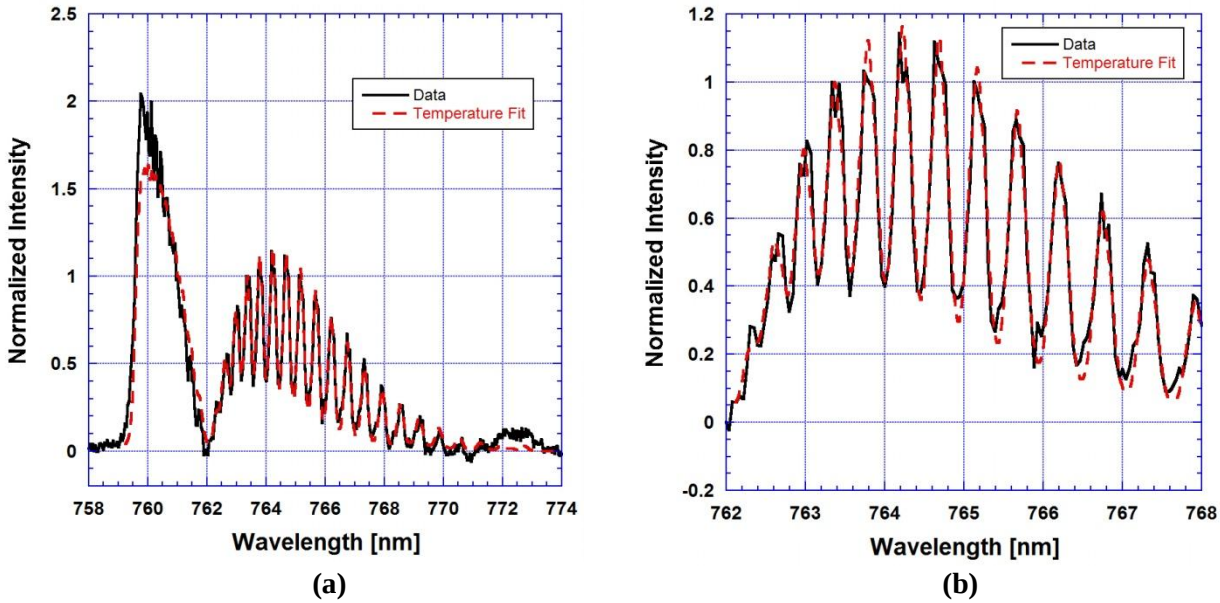

Figure 5.12. (a) Corrected O_2(b) spectrum from Figure 5.10 and temperature fit indicating a gas temperature of 493 K [O_2(b)_MTD method]. (b) Enhanced version of (a) showing the temperature fit to the peaks and valleys of the P-branch.

The results shown above still indicate that the baseline procedure is causing the inconsistencies between the O_2(a) and O_2(b) temperature methods. But it is also interesting to note that the O_2(a) and O_2(b) temperatures still disagreed in the data without NO. When the spectra without NO were observed more closely, the baseline procedure was not zeroing the spectral tails any better than the data with NO. Another cause for the disagreement between O_2(a) and O_2(b) temperature diagnostics is the low signal-to-noise ratio in the experimental spectra. The low signal is caused by the low flow rates and low discharge power. Having a low O_2(a) or O_2(b) signal allows the background noise to have a greater impact on the peaks and valleys. The low signal-to-noise ratio may also be causing the large calculated temperature fluctuations seen in the data.

5.3 Effect of Lineshape Function on Temperature Fit

The previous two subsections looked at experimental O_2(a) and O_2(b) spectra to determine why the four different temperature methods resulted in different gas temperatures. This subsection will present another possible reason why the temperature diagnostics are not in agreement. There is reason to believe that the lineshape function used to develop theoretical O_2(a) and O_2(b) spectra does not give the best results. This subsection will analyze experimental and theoretical O_2(b) spectra to demonstrate this point.

First off, the reader needs to understand the role of the lineshape function (introduced in Section 3.6) in developing theoretical spectra. The purpose of the lineshape function is to transform the infinitesimally thin emission lines (provided by HITRAN) into a distribution of emitted photons. This means that the emission lines are transformed into bell-shaped distribution curves. Since the distribution curves overlap with one another, the overall spectrum is obtained by superimposing all the bell-shaped curves. The current lineshape function used by O_2(a)_MTD, O_2(b)_MTD, and O_2(b)_BSW is a third-order, or super-Lorentzian, lineshape. The third-order Lorentzian lineshape is given as Equation 5.1

$$g(\lambda, \Delta\lambda, \lambda_0) = \frac{(\Delta\lambda/2)^2}{\left[\left|\lambda - \lambda_0\right|^3 + (\Delta\lambda/2)^3\right]} \tag{5.1}$$

where λ is the wavelength, $\Delta\lambda$ is the resolution parameter, and λ_0 is line center location. Both the wavelength and line center location are known variables.

The resolution is one of the two parameters (temperature is the other) that are varied when trying to fit theoretical spectra to experimental spectra. The resolution parameter controls the widths of the individual emission lines. It can be thought of as the full width at half maximum (FWHM) of each emission intensity. As the resolution parameter decreases, the width of each emission distribution decreases. A smaller FWHM causes the emission distributions to become sharper and have lower densities in the tails. This results in less superposition of emission lines and leads to more defined peaks and valleys.

To analyze the lineshape function, the O_2(b) P-branch emissions need to be observed in greater detail. One feature of the O_2(b) spectrum is the presence of "doublet" peaks along the P-branch. The "doublet" peaks occur because the ^{P}P and ^{P}Q transitions are very close to one another. Figure 5.13(a) shows the HITRAN emission intensities of the ^{P}P and ^{P}Q transitions at 296 K. Figure 5.13(b) shows the "doublet" peaks seen in experimental O_2(b) spectra that result from the close proximity of the ^{P}P and ^{P}Q transitions. The spectrum shown in Figure 5.13(b) is from the experiments described in Section 4.5 where O_2(b) measurements were made 5 cm downstream from the discharge. The spectra from this experiment all were very "clean" with a high signal-to-noise ratio. Since the O_2(b) signal was so strong, the NO "air afterglow" effects did not affect the spectra. The remainder of this subsection will use the O_2(b) spectrum shown in Figure 5.13(b) to analyze the lineshape function.

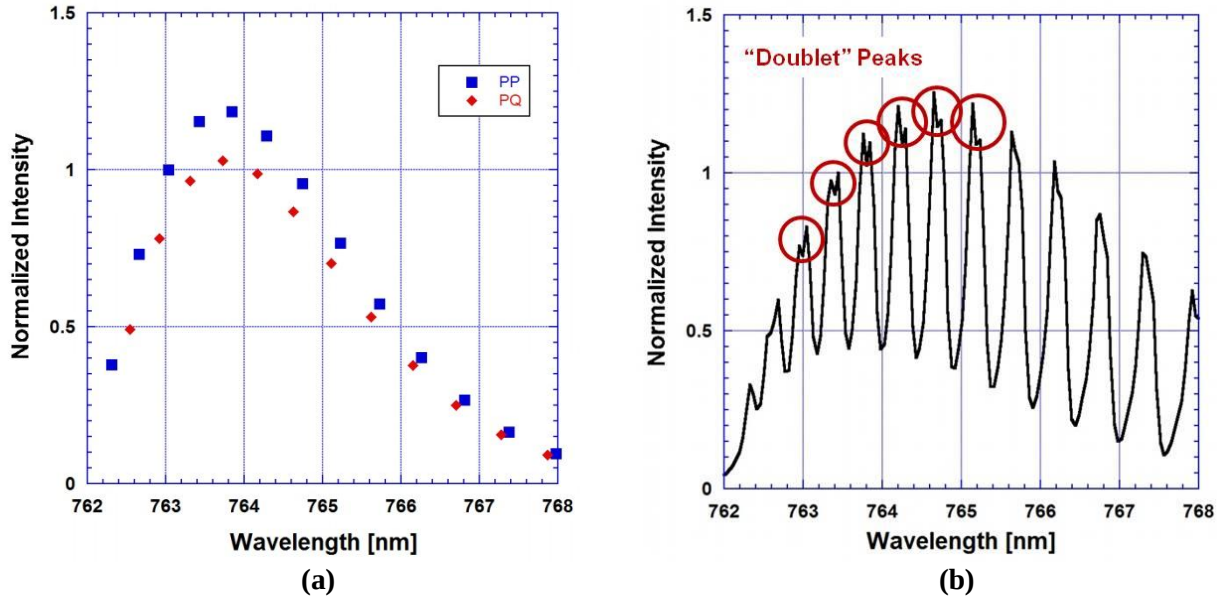

Figure 5.13. (a) HITRAN data at 296 K showing the normalized emission intensities of the ^{P}P and ^{P}Q transitions in the P-branch of the O_2(b) spectrum. (b) Experimental O_2(b) spectrum showing the "doublet" peaks in the P-branch.

When the O_2(b)_BSW method was developed, the resolution of the spectrometer was not high enough to observe the "doublet" peaks in the data. Instead, the "doublet" peaks were blended together to give single peak emissions in the centers of the "doublet" peaks. Since the "doublet" peaks were not observed during experimentation, a lineshape function was chosen (the third-order Lorentzian) which also produced single peaks. Later, a new spectrometer was used to measure the O_2(b) emission that had greater resolution and allowed the "doublet" peaks to be seen. All O_2(b) spectra presented in this thesis were measured with the newer spectrometer where the "doublet" peaks are visible. However, the lineshape used by the O_2(b) temperature diagnostic was never updated to account for the increased instrument resolution. Therefore, temperature calculations are still performed using the third-order Lorentzian lineshape that produces theoretical spectra with only single peaks in the P-branch. Figure 5.14 shows an experimental spectrum and the temperature fit to the data to illustrate the lack of agreement between the "doublet" peaks from experiments and the single peaks from the temperature fits.

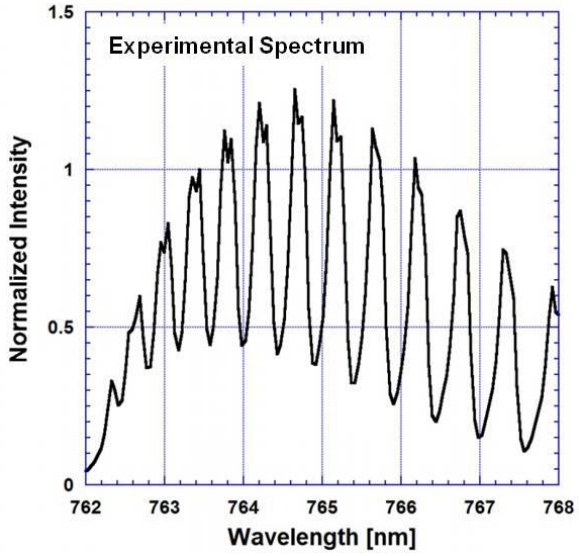

(a)

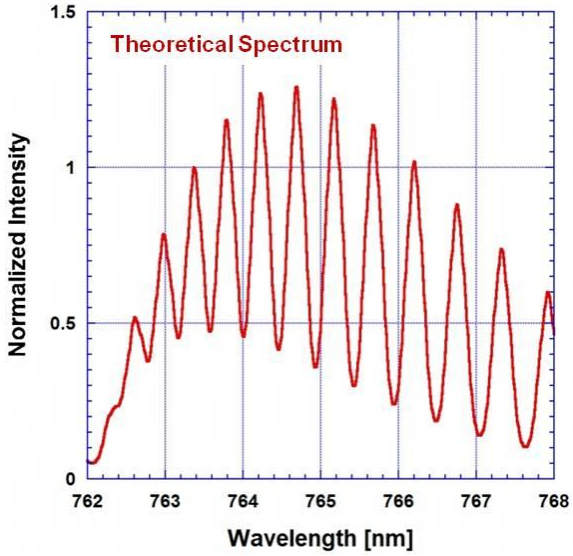

(b)

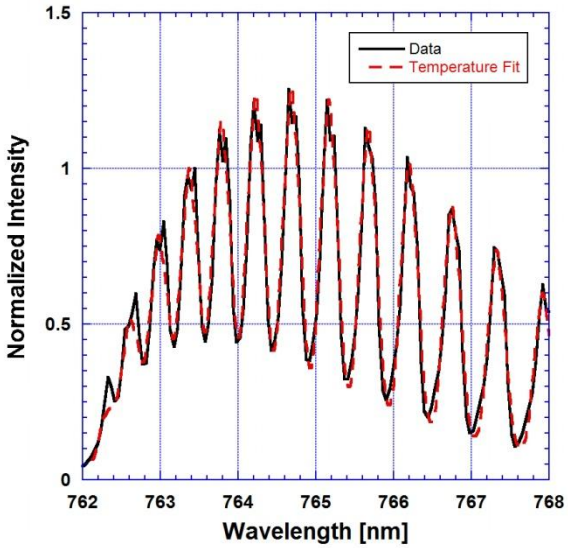

(c)

Figure 5.14. (a) P-branch of an experimental O_2(b) spectrum. (b) Temperature fit of the spectrum shown in (a) indicating a gas temperature of 644 K [O_2(b)_MTD method]. The "doublet" peaks can be seen in the experimental spectrum but not the theoretical spectrum. The inconsistent resolution between the experimental and theoretical spectra indicates that the third-order Lorentzian lineshape is not appropriate for developing theoretical spectra. (c) Both the experimental and temperature fit plotted together. When both data and temperature fit are plotted together, it is hard to see the nonexistent "doublet" peaks in the temperature fit spectrum.

Since the theoretical spectra were not exhibiting the "doublet" peaks, a study was conducted to see if "doublet" peaks could be observed in theoretical spectra with the third-order Lorentzian lineshape. Figure 5.15 shows the experimental spectrum used in the resolution study. Figure 5.16 shows the temperature fit [using O_2(b)_MTD method] to the experimental spectrum from Figure 5.15. The temperature fit indicated a gas temperature of 644 K with 0.235 nm resolution. The spectrum shown in Figure 5.16 is the baseline case used in the resolution study. In order to see the "doublet" peaks in the theoretical spectra, the temperature was held constant at 644 K and the resolution parameter was decreased. Figures 5.16 through 5.20 show the effect

of decreasing the resolution parameter on the theoretical spectrum. As the resolution parameter decreases, the "doublet" peaks become more and more defined. When the resolution reaches 0.120 nm, the "doublet" peaks finally are observed. However, as the "doublet" peaks become more defined, the valleys of the P-branch decrease below the intensity values seen in the experimental spectrum. It is apparent that using the current lineshape function will never produce theoretical spectra with both "doublet" peaks and P-branch valleys that are not unreasonably low.

Another interesting observation can be made when looking at the R-branch in Figures 5.16 through 5.17. As the resolution parameter is decreased, the individual emissions from the R-branch (759 nm to 762 nm) become more defined. The R-branch emissions from the experimental spectrum are qualitatively most similar to the theoretical spectrum with a resolution of 0.150 nm. Again, this points to a lineshape problem since the P-branch valley intensities of the theoretical spectrum with 0.150 nm resolution are much lower than the valley intensities in the experimental spectrum. The main point to be taken from this analysis is that the O_2(b)_BSW and O_2(b)_MTD methods are trying to match peaks and valleys using a lineshape function that can never output theoretical spectra capable of matching the resolution of experimental spectra.

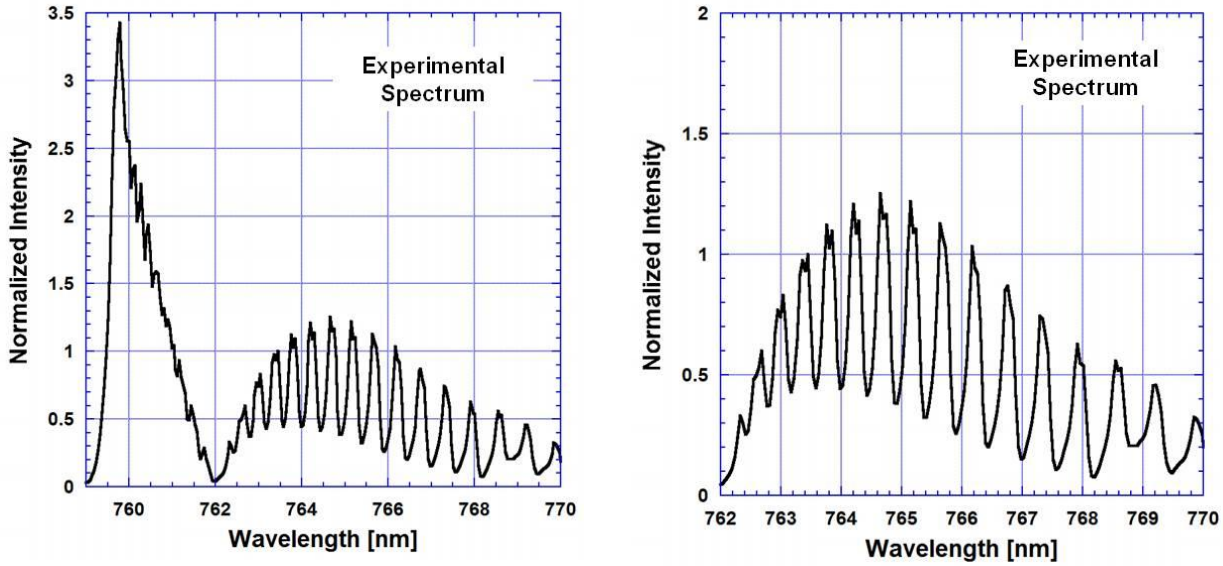

Figure 5.15. (a) Experimental O_2(b) spectrum taken approximately 5 cm downstream from the discharge exit. (b) Enhanced version of (a) showing more details of the P-branch emissions.

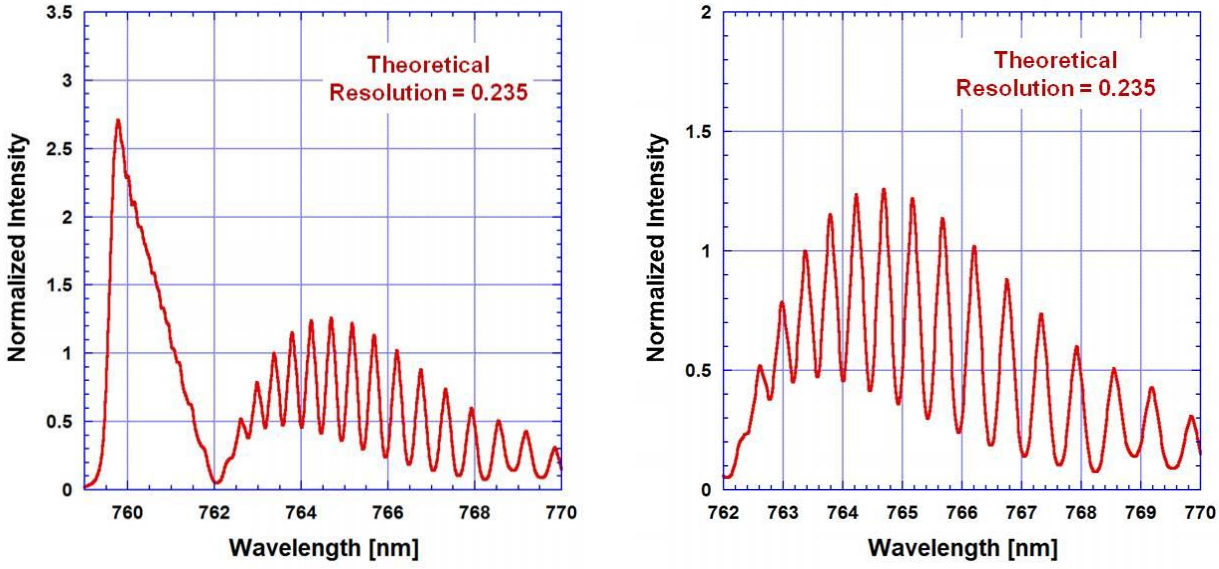

Figure 5.16. (a) Theoretical O_2(b) spectrum that was matched to the experimental spectrum shown in Figure 5.15. The temperature of the spectrum is 644 K and the resolution parameter is 0.235 nm. (b) Enhanced version of (a) showing more details of the P-branch emissions.

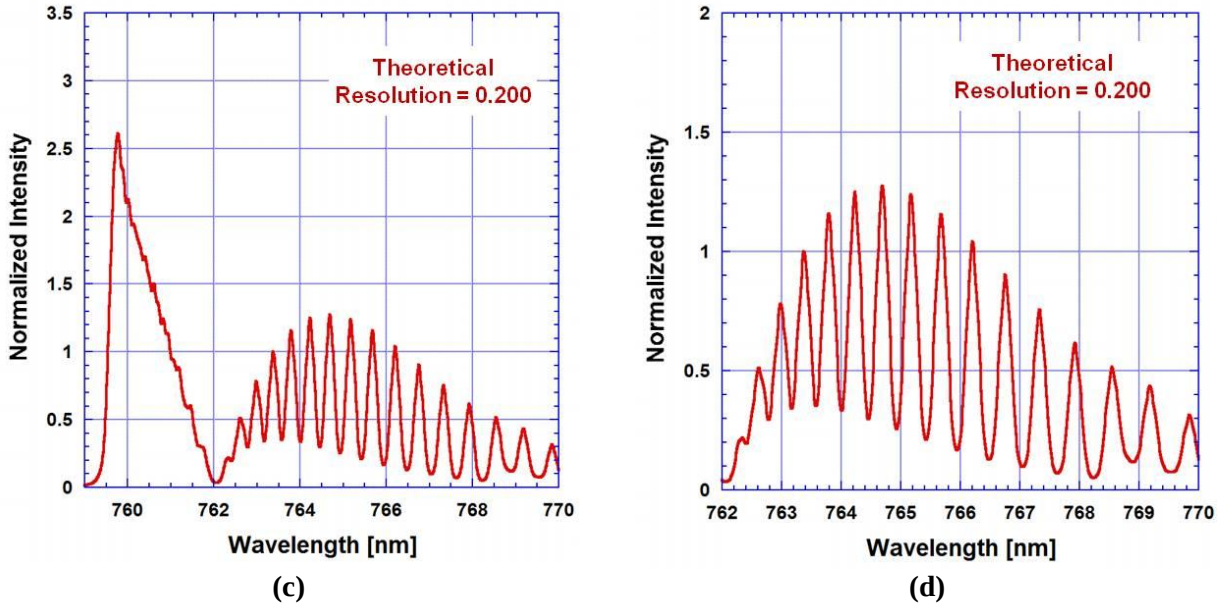

Figure 5.17. (a) Theoretical O_2(b) spectrum at a temperature of 644 K with a resolution parameter of 0.200 nm. (b) Enhanced version of (a) showing more details of the P-branch emissions.

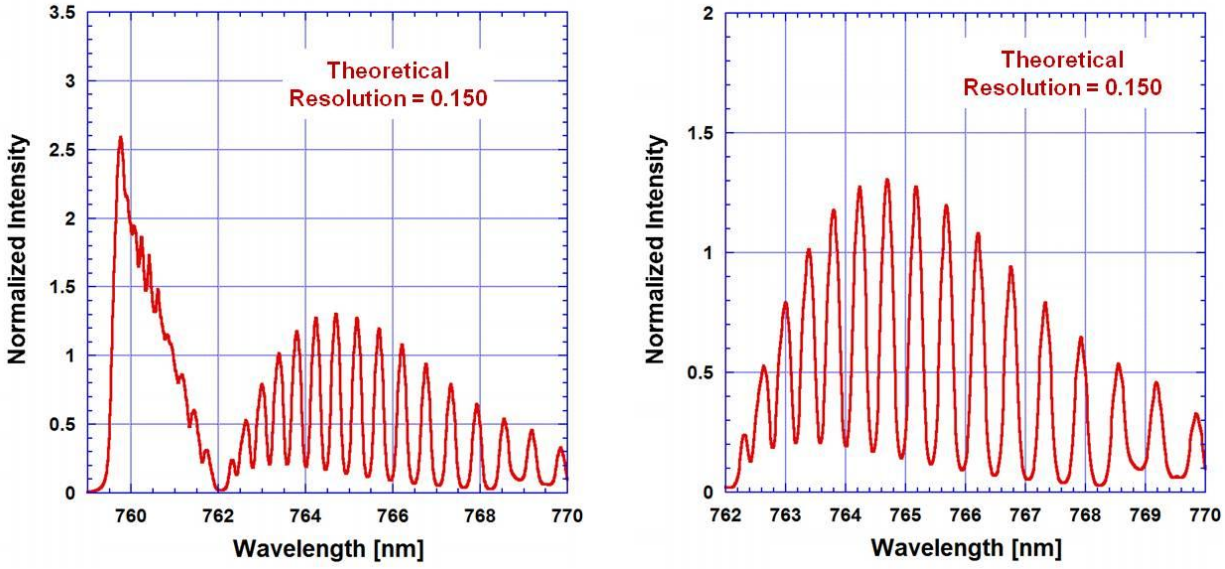

(c) **(d)**

Figure 5.18. (a) Theoretical O_2(b) spectrum at a temperature of 644 K with a resolution parameter of 0.150 nm. (b) Enhanced version of (a) showing more details of the P-branch emissions.

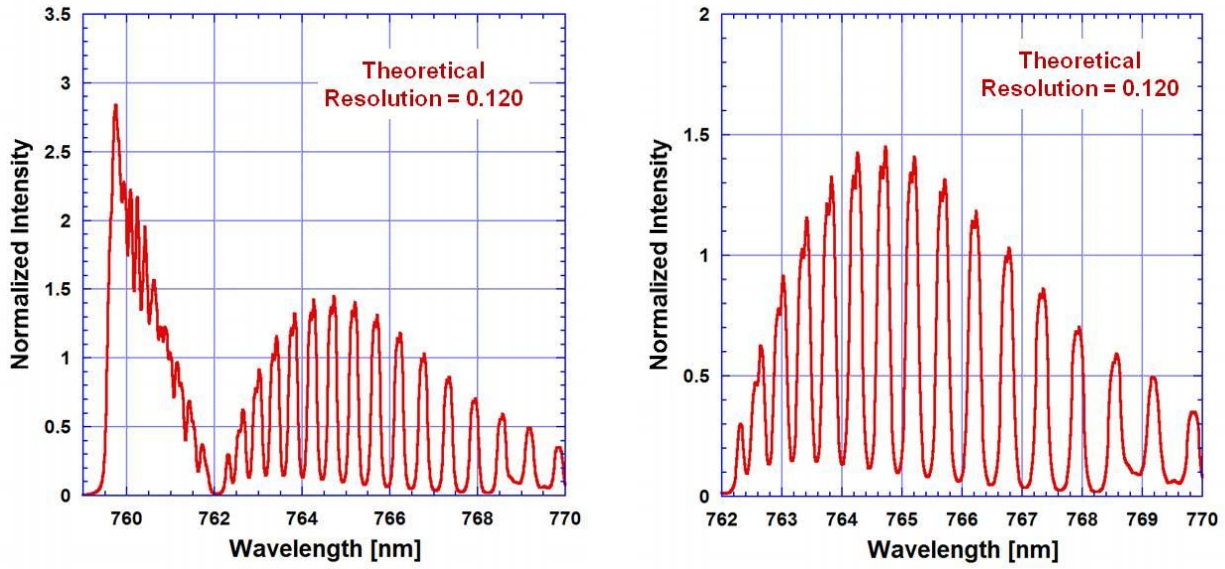

(e) **(f)**

Figure 5.19. (a) Theoretical O_2(b) spectrum at a temperature of 644 K with a resolution parameter of 0.120 nm. (b) Enhanced version of (a) showing more details of the P-branch emissions.

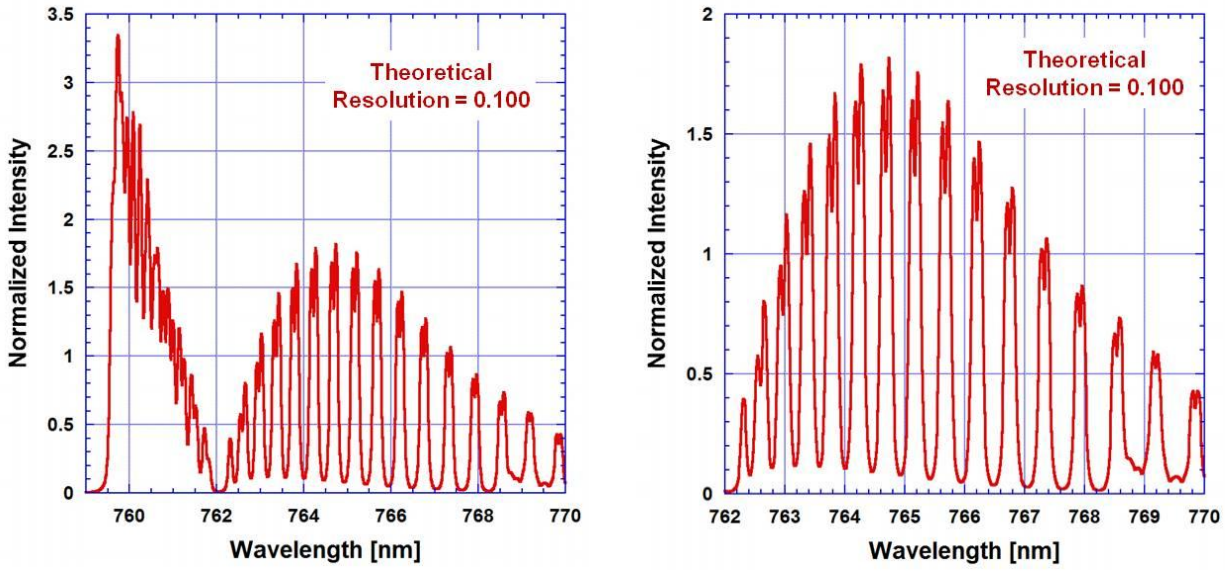

Figure 5.20. (a) Theoretical O_2(b) spectrum at a temperature of 644 K with a resolution parameter of 0.100 nm. (b) Enhanced version of (a) showing more details of the P-branch emissions.

Since the third-order Lorentzian lineshape is not matching the "doublet" peaks while keeping the valley heights elevated, a different lineshape function was investigated. Instead of using the third-order Lorentzian, a normal Lorentzian lineshape was used. The Lorentzian lineshape function is given as Equation 5.2.

$$g(\lambda, \Delta\lambda, \lambda_0) = \frac{(\Delta\lambda/2)}{\left[\left|\lambda - \lambda_0\right|^2 + (\Delta\lambda/2)^2\right]} \tag{5.2}$$

This new lineshape function was used to match the experimental spectrum shown in Figure 5.15. Figure 5.21 shows the results of the temperature fit using the normal Lorentzian lineshape. The temperature fit indicated an O_2(b) temperature of 630 K with 0.139 resolution. The theoretical spectrum formed using the normal Lorentzian lineshape seems to solve the problems observed with the third-order Lorentzian lineshape. The "doublet" peaks are observed and the valley intensities remain at the same magnitude as the valleys in the experimental spectrum. These results indicate that the normal Lorentzian lineshape produces theoretical spectra that better match the resolution of the experimental spectra. Therefore, the normal Lorentzian seems to be the more accurate choice when trying to match experimental and theoretical spectra.

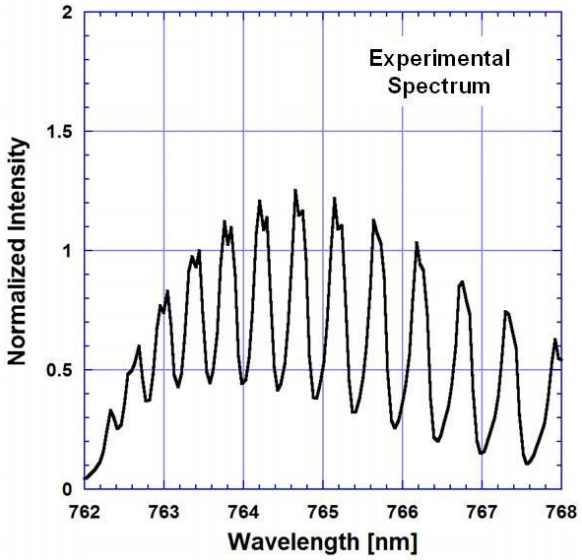

(a)

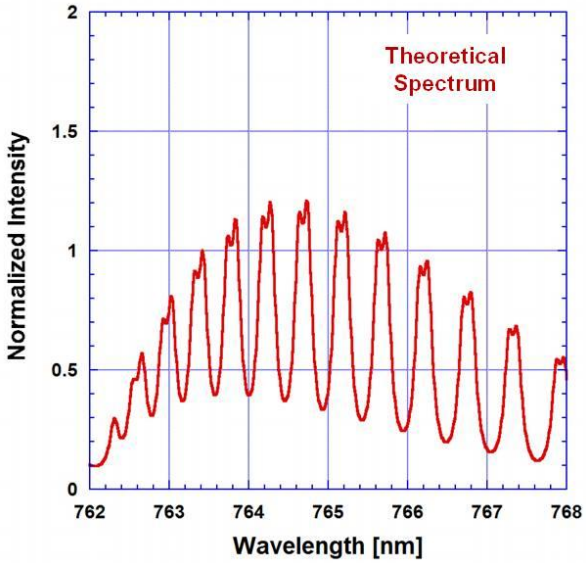

(b)

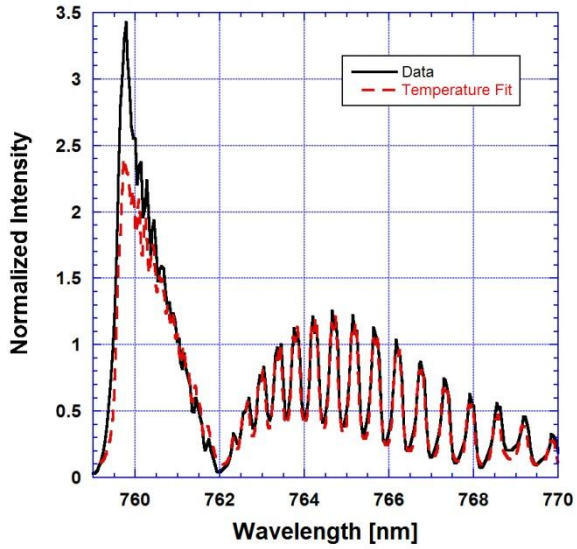

(c)

Figure 5.21. P-branches of (a) experimental and (b) theoretical O_2(b) spectrum. The theoretical spectrum was matched to the experimental spectrum. The theoretical spectrum was formed using the normal Lorentzian lineshape. (c) The entire O_2(b) emission showing the data and temperature fit. The temperature fit indicated a temperature of 630 K with a resolution parameter equal to 0.139 nm.

Using the third-order Lorentzian lineshape function could be one reason why the O_2(a) and O_2(b) temperature diagnostics are not calculating the same gas temperatures. The third-order Lorentzian lineshape superimposes the "doublet" peaks and allows the resulting single peak to reach higher intensities at a lower temperature. Therefore, the theoretical spectrum can stay at lower temperatures (which it must do anyway to match the valleys when using the third-order Lorentzian) and still match the peaks. This results in lower temperature measurements than the actual flow temperature. Using the normal Lorentzian lineshape should result in higher calculated O_2(b) temperatures since the "doublet" peaks will not be superimposed.

Plans were made to alter the temperature fit process so that the "doublet" peaks seen in the data could be matched to theoretical spectra. However, changing the lineshape to a normal Lorentzian uncovers a problem between the experimental and theoretical spectra. The relationship between the "doublet" peaks (in terms of relative intensity) for the experimental and theoretical spectra is not the same. This point is illustrated by Figure 5.22 where a few P-branch emissions are shown for both the experimental and theoretical spectra. The experimental and theoretical spectra shown in Figure 5.22 are the same spectra shown in Figure 5.21. The vertical axis for the temperature fit spectrum has been shifted upward so that the "doublet" peaks for the data and temperature fit can easily be compared. From looking at Figure 5.22, the "doublet" peaks from 762 nm to 763.4 nm exhibit the same trends between the data and temperature fit. However, after 763.4 nm, the "doublet" peaks are not consistent between the data and temperature fit. In the temperature fit, the "doublet" peaks on the higher wavelength side always have greater intensities. The opposite behavior is observed in the data.

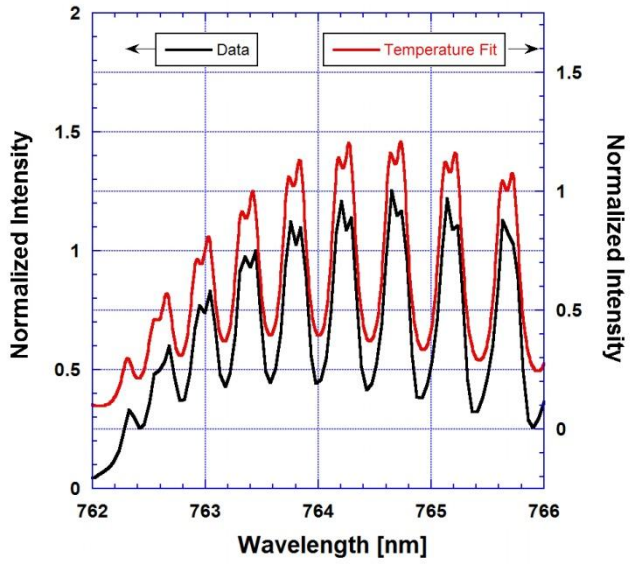

Figure 5.22. P-branches of experimental (data) and theoretical (temperature fit) O_2(b) spectra showing the discrepancy between the "doublet" peaks. The vertical axis for the temperature fit spectrum has been shifted upward so that the "doublet" peaks for the data and temperature fit can easily be compared. At wavelengths higher than 763.4 nm, the "doublet" peaks are not consistent between the data and temperature fit. in the temperature fit, the "doublet" peak on the higher wavelength side always has a greater intensity. The opposite is true for the data.

There is no certain reason why the "doublet" peaks in the data are behaving differently from the theory. One hypothesis is that the instrument resolution is not high enough to observe the detail of the "doublet" peaks. The counterargument to this is: If instrument resolution is not high enough to observe the detail of the "doublet" peaks, then why do the first few "doublet" peaks in the data (from 762 nm to 763 nm) match the "doublet" peaks in the theoretical spectrum? Another possible reason for the disagreeing data and theory may involve the gas

velocity. The gas velocity may be shifting the emission lines in the experimental spectra. The data used from HITRAN to produce the theoretical spectra were obtained from a still gas. Measuring a high-speed gas may be leading to the inconsistencies. Whatever the reason, the fact remains that something is causing a disagreement between theory and data. Since the discrepancy between the “doublet” peaks in the experimental and theoretical spectra exists, any attempt to match the “doublet” peaks is unattainable.

6. Concluding Remarks and Future Recommendations

This thesis described the development of new spectroscopic temperature diagnostics for use in the EOIL system. The HITRAN database was used to develop temperature-dependent theoretical O_2(a) and O_2(b) emission spectra. Gas temperatures were calculated by matching the theoretical emission spectra to experimental measurements. In the past, gas temperatures were calculated using only the O_2(b) emission spectra. This proved to be problematic since the O_2(b) emission signal is not strong enough for accurate temperature calculations in all regions of the laser system. Since the O_2(a) emission signal is strong throughout the EOIL system, the O_2(a) temperature diagnostic can calculate temperatures in regions where the O_2(b) signal is weak.

Section 3 described the procedure used to convert HITRAN data into theoretical emission spectra. It also described the matching procedure used to compare theoretical and experimental spectra. The O_2(a) and O_2(b) methods developed in this thesis were given the shorthand names: O_2(a)_MTD and O_2(b)_MTD. The temperatures calculated from the O_2(a)_MTD and O_2(b)_MTD methods were compared to the two current O_2(b) temperature diagnostics: O_2(b)_BSW and O_2(b)_Macro.

Section 4 showed experiments where the newly developed O_2(a)_MTD and O_2(b)_MTD methods were used to analyze data. The O_2(a)_MTD method showed promising results by calculating O_2(a) temperatures in the subsonic section of VertiCOIL. The strong O_2(a) signals and low background noise in VertiCOIL resulted in temperatures within ±4 K. The O_2(a) temperature diagnostic was also used to analyze the performance of two heat exchanger designs. Additionally, both O_2(a) and O_2(b) temperature diagnostics were able to determine gas temperatures in the supersonic laser cavity. Section 4 also looked at the level of agreement between the four temperature methods. In general, the O_2(a) and O_2(b) methods calculated different gas temperatures. The differences between the O_2(a) and O_2(b) calculated temperatures depended on the experiment conditions. When the NO_2* "air afterglow" signal was low and the O_2(a) and O_2(b) signals were strong, the calculated temperatures usually were within ±10 K. When the "air afterglow" signal increased, the temperature difference between the O_2(a) and O_2(b) diagnostics increased as well. For instance, the spectra shown in Figure 5.4 (with a large "air afterglow" signal) resulted in a 100 K temperature difference between the O_2(a) and O_2(b) methods. As shown in Section 4.1, the effects of the "air afterglow" on the spectra were dependent on discharge power and system pressure. Additionally, the spectra measurement

location within the EOIL system impacted the "air afterglow" effects. For instance, spectra measurements downstream from the heat exchangers were greatly affected by the "air afterglow."

Section 5 examined aspects of the temperature determination methods to determine why difference existed between the O_2(a) and O_2(b) temperatures. The analysis showed that problems existed when trying to determine gas temperatures in EOIL using spectroscopic measurements. The largest cause for concern is the baseline procedure used to correct the O_2(a) and O_2(b) spectra. In some experimental spectra, the current linear baseline procedure has trouble zeroing the emission tails. This was especially true when spectra were measured at low discharge powers or low pressures where the emission signal-to-noise ratio was low. Also, O_2(a) and O_2(b) measurements made downstream from the heat exchanger exhibit a nonlinear baseline from the NO "air afterglow." Using the linear correction procedure on a baseline that is nonlinear causes higher calculated temperature from O_2(a) spectra and lower calculated temperature from O_2(b) spectra. In the spectra downstream of the heat exchanger, the calculated O_2(a) and O_2(b) temperatures varied by about 50 K.

In addition to the baseline procedure, the lineshape currently used to produce theoretical spectra may be causing disagreement between the O_2(a) and O_2(b) temperature diagnostics. As discussed in Section 5.3, the third-order Lorentzian lineshape does not produce theoretical spectra capable of matching the shape of the experimental spectra. The third-order Lorentzian lineshape superimposes the "doublet" peaks and allows the resulting single peak to reach higher intensities at a lower temperature. This allows the theoretical spectrum to stay at lower temperatures and still match the peaks. This diagnostic then outputs lower temperature measurements than the actual flow temperature. Section 5.3 showed that changing the lineshape function to a normal Lorentzian produced theoretical spectra that better matched the resolution of the experimental spectra. However, changing the lineshape to a normal Lorentzian uncovered inconsistencies between the "doublet" peaks of experimental and theoretical spectra. This discrepancy does not allow temperatures to be calculated by matching the "doublet" peaks between experimental and theoretical spectra. The reason for the inconsistencies between "doublet" peaks in experimental and theoretical spectra still is not understood.

Even though the newly developed O_2(a)_MTD and O_2(b)_MTD temperature diagnostics have a few problems, the methods have provided promising results. In order to improve the

temperature diagnostics, a number of things can be done. As mentioned in Section 5.1, a higher-order polynomial method may be a solution to obtaining better baselines. A nonlinear baseline may serve as a better approximation to the "air afterglow" emissions. This would increase the robustness of the baseline procedure. The higher-order polynomial method could be used whether spectra are measured downstream of the discharge (where the baseline is usually more linear) or downstream of the heat exchanger (where the baseline is the most nonlinear).

If the higher-order polynomial process can be automated and integrated into the data reduction process, then it may be the key to more consistent temperatures between O_2(a) and O_2(b). It may also provide consistent results between the three O_2(b) temperature diagnostics. An important aspect of temperature diagnostics is the speed at which temperature calculations take place. During experiments, it is useful to have temperature information very quickly (within minutes after measurements are made) so that O_2(a) yields can be calculated immediately. The quick results allow experimenters to make adjustments "on the fly" to improve system performance. The current linear correction method is computationally inexpensive and requires only a few seconds to complete. Since it uses an automated process, the O_2(b)_Macro method (which uses the linear baseline procedure) is the fastest method at determining gas temperature. Because the O_2(b)_Macro determines gas temperature the fastest, it is usually used for temperature calculations. However, it may be advantageous to slow down the data reduction procedure so that more accurate temperatures can be obtained. Spectra should be analyzed after the baseline procedure to ensure that the proper baseline has been applied. If the higher-order polynomial process still does not work, then the experimenters may need to adjust the spectra by hand so that zero baselines are obtained. This would cause more work for the experimenters, but may lead to more accurate results.

In addition to improving the baseline procedure, there are some other ways to improve the temperature calculations. One possible change involves the matching process. Instead of only matching peaks and valleys in the data, it may be better to match every point in the experimental spectrum to the theoretical spectrum using a least squares fit. This would be much more expensive computationally, but it should provide more accurate results. Also, different lineshapes for the theoretical spectra (besides the normal and third-order Lorentzian) can be studied. A Gaussian lineshape may produce theoretical spectra that best match the resolution of the experimental spectra. An even better lineshape might be a Voigt function (first introduced in

Section 3.4 when describing the gain temperature diagnostic), which is a convolution of Gaussian and Lorentzian lineshapes. The Voigt function may be the most accurate lineshape since it uses contributions from both the Lorentzian and Doppler linewidths. The Lorentzian broadening occurs from collisional broadening effects (i.e. pressure). The collisional broadening effect can be calculated from the gas pressure collisional broadening coefficients. If one knows the gas flow rates and pressures, the Lorentzian broadening effects can be calculated. The gas temperature causes variations to Doppler broadening. Therefore, temperature would be varied in the Doppler broadening term when trying to match experimental and theoretical spectra.